Theses and Dissertations

12-2010

Redox-Magnetohydrodynamic (MHD) Microfluidics: Fundamentals, Optimization, and Applications to Analytical Chemistry

Melissa Christine Weston
University of Arkansas, Fayetteville

REDOX-MAGNETOHYDRODYNAMIC (MHD) MICROFLUIDICS: FUNDAMENTALS, OPTIMIZATION, AND APPLICATIONS TO ANALYTICAL CHEMISTRY

REDOX-MAGNETOHYDRODYNAMIC (MHD) MICROFLUIDICS: FUNDAMENTALS, OPTIMIZATION, AND APPLICATIONS TO ANALYTICAL CHEMISTRY

A dissertation submitted in partial fulfillment
of the requirements for the degree of
Doctor of Philosophy in Chemistry

By

Melissa Christine Weston
Colorado State University
Bachelor of Science in Chemistry, 2006

December 2010
University of Arkansas

Abstract

Microfluidic systems are of great interest in analytical chemistry for the development of lab-on-a-chip devices. This dissertation describes fundamental investigations of magnetohydrodynamics with added redox species (redox-MHD) as a new microfluidic approach for use in analytical applications. Redox-MHD is attractive because it offers a unique combination of desirable features that are otherwise only available separately with individual micropumps. Redox-MHD is compatible with aqueous and nonaqueous solutions, does not require moving parts, easily reverses flow direction, and requires only low voltages. An ion flux is generated from the oxidation or reduction of an electroactive species at specific locations by activated electrodes patterned on the chip. In the presence of a magnetic field perpendicular to the ion flux, a magnetic force is generated to induce solution convection. This convection is visualized using microbeads to track fluid flow over microband electrode arrays to investigate redox-MHD in a confined solution. The effects of concentration of redox species, widths of electrodes, gaps between electrodes, and applied potentials and currents on flow velocities are discussed. A significant result is the fairly flat flow profile attained in the gap between electrodes that are oppositely biased. A novel method for maximizing flow velocities in order to lower the necessary concentration of redox species to perform pumping is presented. Velocities were increased by as much as 70% from control experiments using the technique. Redox MHD-induced convection was also shown to be compatible with and used to transport components of an immunoassay (without channel walls) while simultaneously detecting an enzymatically-generated electroactive species. Key findings include much lower concentrations of redox-pumping species than were

originally anticipated, enzymatic activity was sustainable in the presence of those pumping species, detection signal easily separated from pumping signal, and direction of fluid motion controlled by active electrode placement instead of reconfiguring channel walls or controlling valves. These results suggest that a general design of a microfluidic device could be utilized for a broad range of flow patterns and applications.

This dissertation is approved for recommendation
to the Graduate Council.

Dissertation Director:

_____

Dr. David Paul

Dissertation Committee:

_____

Dr. Ingrid Fritsch

_____

Dr. Charles Wilkins

_____

Dr. Xiaogang Peng

Dissertation Duplication Release

       I hereby authorize the University of Arkansas Libraries to duplicate this dissertation when needed for research and/or scholarship.

Agreed   _____
              Melissa Christine Weston

Refused   _____
              Melissa Christine Weston

Acknowledgements

I would like to sincerely thank my research advisor, Dr. Ingrid Fritsch, for the invaluable guidance and support she has provided throughout my graduate studies. For her patience and attention to detail, and for the time and energy she has invested into helping me grow as a scientist, I am forever indebted. Many thanks go to the other members of the analytical faculty and to my committee, Dr. David Paul, Dr. Charles Wilkins, Dr. Julie Stenken, and Dr. Xiaogang Peng, for their instruction in research and for the education presented in classes and seminars. Thanks especially to Jerry Homesley who has devoted his time to always helping out our lab when necessary and for his exceptional help with my project, in particular.

I am very grateful for the friendship of all those I have worked closely with in the lab- Andrea, Anu, Caitlin, Christena, Matt, and Penny- thank you for your helpful day-to-day advice and for making the lab such a pleasant place to work. Special thanks go to Dr. Emily Anderson, my very good friend and mentor who, through her everyday positive attitude and patience in teaching me the ways of the lab, has helped me get to where I am today.

Finally, and most importantly, I would like to thank my parents for their constant love and support, and my sister and best friend, Elizabeth, for always being there for me. To Dan, I especially thank you for your daily encouragement and positivity in helping me through this endeavor.

Table of Contents

Chapter 1

Introduction to Redox-Magnetohydrodynamics for Fluid Flow

Overview

Miniaturization drives much of the research and development in analytical chemistry. Downsizing chemical analyses has advantages such as smaller volume requirements, less waste and materials, reduced power consumption, and on-site analysis capability. Smaller scales can offer improvements in sensitivity and new approaches in solving analytical chemistry problems. Microfluidics is critical for the development of micro total analysis systems (μTAS) which aim to combine multiple laboratory procedures in single hand-held devices. This could revolutionize chemical analyses which require multiple steps involving mixing and directing fluids as in DNA sequencing and immunoassays. These "lab-on-a-chip" systems could also be used for environmental monitoring, medical diagnostics, and drug discovery applications. There are challenges which arise, however, in handling fluids at small dimensions in an automated fashion: small volumes can evaporate quickly unless enclosed, laminar flow conditions inhibit mixing and stirring, and a pump must match the system's parameters and flow requirements (stopping, starting, speed, and direction). Thus, there is a need for the further study and development of microfluidic approaches.

There are a number of microfluidic methods presently of interest in the field; each with their unique advantages and limitations. Mechanical pumps offer a large variety of operating procedures, however, they are difficult to miniaturize as they usually utilize moving parts, valves, and thus, require extensive fabrication procedures.[1] Centrifugal pumping is attractive due to its low cost as well as adaptability to a wide range of channel sizes.[2] However, centrifugal fluidics requires a motor and rotating system and only allows for unidirectional flow which limits its applicability. Electrokinetic control is based upon

the interaction of an external electric field with the working fluid to cause flow and is probably, the most popular of all the micropumping methods. Electrokinetic control allows for pumping in small channels without high external pressures and moves fluid with a flat velocity profile, which makes electrokinetics advantageous for separations.[3] The main disadvantages of electrokinetic pumping are that it requires high voltages which can result in bubble formation due to the electrolysis of water and is highly dependent on the physicochemical properties of the fluid and channel walls and thus flow rates can change with solution composition and over time. Thus, there is a need for a novel microfluidic pumping system which can incorporate advantages of existing techniques such as low power, controlled flow direction, and ease of fabrication, while overcoming disadvantages such as limitations with respect to device materials and solutions. Magnetohydrodynamic (MHD) microfluidics may offer these benefits and is the topic of this dissertation. The topic of using magnetic fields to induce convection in solution has recently been reviewed by Pamme,[4] Qian and Bau,[5] and us.[6] Our review, "Magnetic Fields for Fluid Motion," appeared as a feature article in Analytical Chemistry and serves as the basis for this chapter.

MHD involves three physical fields: electric, magnetic, and flow.[7] The driving source for MHD pumping is the magnetic force, $\mathbf{F_B}$ (N/m^3), which is generated from the interaction of an ion current (or ion motion) with a magnetic field at right angles to each other, as defined by the cross product:

$$\mathbf{F_B} = \mathbf{j} \times \mathbf{B}$$

where $\mathbf{j}$ is the flux density of ions (A/m^2), and $\mathbf{B}$ is the magnetic flux density (T). MHD microfluidics is attractive for several reasons. First, MHD does not require moving parts thereby simplifying device fabrication over mechanical pumping methods, such as syringe pumps and centrifugal approaches. MHD offers the advantage of bi-directional pumping without the use of valves, which is readily accomplished by changing the polarity of either the magnetic field or the ion flux. MHD can also operate in both aqueous and non-aqueous solutions, performs well in a large range of channel widths, and does not require channel walls, thereby allowing for greater flexibility in device fabrication. Pumping is also easily performed in a loop, which is beneficial for chromatographic applications and stirring solutions, on the microscale, using MHD is possible.

It has only been recently (in the past 10 years) that MHD has been applied to microfluidics.[4-6] MHD has been successfully reported for both pumping[8-15] and mixing[16-18] applications and has been used in conjunction with a variety of analytical applications, including separations[19], nuclear magnetic resonance (NMR)[20], and polymerase chain reaction (PCR)[18]. However, in all of these approaches, bubble formation due to electrolysis of water caused interferences in pumping and in some cases, electrode dissolution occurred.

Adding redox species alleviates the problems of electrode degradation and water electrolysis because the resulting faradaic processes generate high currents while maintaining low applied voltages.[21] This approach, termed redox-MHD, is the focus of this dissertation. Redox-MHD has often been characterized by measuring changes in currents and/or by using colored redox species to study convection.[22-32] However, most of

these reports are fundamental studies of the phenomenon, and thus, do not have any direct, practical application. There are only a small number of reports which suggest the use of redox-MHD for microfluidics.[33-37] Redox-MHD was demonstrated as a pumping method for both aqueous and non-aqueous solutions ($Fe(CN)_6^{3-}$ and $Fe(CN)_6^{4-}$ in water and NB in acetonitrile) using gold electrodes along the sidewalls of an LTCC channel.[9, 18] These reports established that velocity could be readily varied by either changing the applied potential or redox species concentration and direction of flow could be changed with ease as well, by changing the polarity of the electrodes or the direction of the magnetic field. Another report used the reversible aluminum deposition and stripping reaction in a chloroaluminate ionic liquid, at aluminum electrodes, to pump fluids.[17] This report also demonstrated the ease with which fluid direction could be changed by simply changing the polarity of the current.

However, because of the minimal studies surrounding this topic, a major portion of this dissertation is dedicated to investigating the fundamentals of redox-MHD microfluidics through flow visualization to track microbeads in solution. This technique is unique to redox-MHD studies in that convection could be observed even without measurable changes in current in the presence of the magnetic field and also allowed us to determine flow velocities and trajectories throughout the solution in order to optimize redox-MHD fluid flow for use in analytical applications.

Applications of redox-MHD to analytical chemistry are even fewer. Redox-MHD has been limited to investigations to increase sensitivity and achieve lower detection limits, through convection, in anodic stripping voltammetry (ASV) for trace metal analysis.[38-40] These studies were performed on a large scale in which the same electrode

5

was used for convection and detection purposes and thus, adding sample solution and rinsing were performed manually. Thus, a focus of the work in this dissertation is to design a flow-through system in which the pumping and detecting features are separate electrodes and an analyte can be introduced into the electrochemical cell and pumped across a surface (detector) in an automated fashion. An illustration of redox-MHD in such a device is shown in Figure 1.1.

A limitation of redox-MHD for use in analytical applications is the need for high concentrations of redox species to provide a large enough ion flux that a sufficient magnitude of $\mathbf{F_B}$ can be generated in the low magnetic fields of permanent magnets. High concentrations could cause interferences in analysis and detection methods. Thus, the final portion of this dissertation is dedicated to investigating ways in which to maximize $\mathbf{F_B}$, and the resulting flow velocities, while minimizing the necessary redox species concentration in order to expand the use of redox-MHD microfluidics for analytical chemistry based applications.

The chapters that follow contain introductory paragraphs to further describe the background and purpose of the research reported in this dissertation. The following chapters were originally written to be self-contained manuscripts for publication. Thus, some redundancy is present.
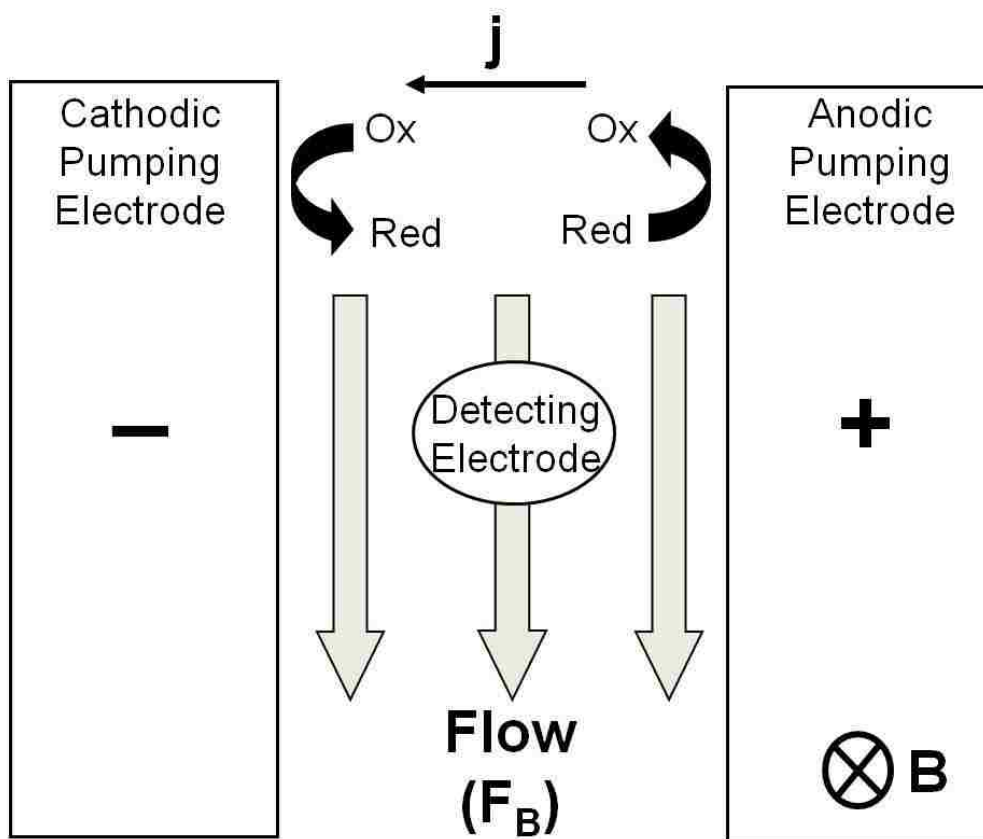
<u>Figure 1.1.</u> Schematic of redox MHD. Electroactive species carry current between the oppositely polarized electrodes. In the presence of a magnetic field, fluid flow is created. Fluid is directed over the detecting electrode through between the pumping electrodes.

Summary

Chapter 2 of this dissertation investigates redox-MHD flow at microelectrode arrays using polystyrene microbeads in an applied potential approach. Parameters such as electrode size, electrode spacing, and redox-species concentration are studied for their effect on flow velocities and trajectories. Flow profiles throughout solution are also investigated. This chapter is based on a publication in Analytical Chemistry.[41]

Chapter 3 reports on a highly controlled approach to manipulating redox-MHD fluid flow by controlling the current at microband electrodes. Quantitative relationships of current and magnetic field on $\mathbf{F_B}$ were determined providing insight for control of redox-MHD in microfluidic systems. This chapter is based on a manuscript, submitted for publication to Sensors and Actuators.

The ability to use redox-MHD for simultaneous pumping and detection of an immunoassay-important molecule is described in Chapter 4. The effect of the redox-pumping species on detection of the molecule and the effect of an active detecting electrode on redox-MHD pumping were investigated. This chapter is based on a publication that appeared as a Letter in Analytical Chemistry.

Chapter 5 involves investigating ways to minimize the necessary redox species concentration while maximizing $\mathbf{F_B}$, and the resulting flow velocities. Different potential waveforms and electrode designs were reported on for optimizing redox-MHD flow. The techniques reported therein could be used to expand the use of redox-MHD microfluidics for analytical chemistry based applications.

References

(1)   Nguyen, N.; Huang, X.; Chuan, T. K. *Journal of Fluids Engineering* **2002**, *124*, 384-392.

(2)   Duffy, D. C.; Gillis, H. L.; Lin, J.; Sheppard Jr., N. F.; Kellogg, G. J. *Anal. Chem.* **1999**, *71*, 4669-4678.

(3)   Harrison, D. J.; Manz, A.; Fan, Z. H.; Ludi, H.; Widmer, H. M. *Analytical Chemistry* **1992**, *64*, 1926-1932.

(4)   Pamme, N. *Lab on a Chip* **2006**, *6*, 24-38.

(5)   Qian, S. Z.; Bau, H. H. *Mechanics Research Communications* **2009**, *36*, 10-21.

(6)   Weston, M. C.; Gerner, M. D.; Fritsch, I. *Analytical Chemistry* **2010**, *82*, 3411-3418.

(7)   Davidson, P. A. *An Introduction to Magnetohydrodynamics* Cambridge University Press: New York, 2001.

(8)   Bau, H. H.; Zhu, J. Z.; Qian, S. Z.; Xiang, Y. *Sensors and Actuators B-Chemical* **2003**, *88*, 205-216.

(9)   Homsy, A.; Koster, S.; Eijkel, J. C. T.; van den Berg, A.; Lucklum, F.; Verpoorte, E.; de Rooij, N. F. *Lab Chip* **2005**, *5*, 466-471.

(10)   Jang, J.; Lee, S. S. *Sensors and Actuators A* **2000**, *80*, 84-89.

(11)   Lemoff, A. V.; Lee, A. P. *Sensors and Actuators B* **2000**, *63*, 178-185.

(12)   Lemoff, A. V.; Lee, A. P. *Biomedical Microdevices* **2003**, *5*, 55-60.

(13)   Nguyen, B.; Kassegne, S. K. *Microfluidics and Nanofluidics* **2008**, *5*, 383-393.

(14)   Wang, L. S.; Flanagan, L.; Lee, A. P. *Journal of Microelectromechanical Systems* **2007**, *16*, 454-461.

(15)   Zhong, J. H.; Yi, M. Q.; Bau, H. H. *Sensors and Actuators a-Physical* **2002**, *96*, 59-66.

(16)   Qian, S.; Bau, H. H. *Sensors and Actuators B-Chemical* **2005**, *106*, 859-870.

(17)   Qian, S.; Zhu, J.; Bau, H. H. *Physics of Fluids* **2002**, *14*, 3584-3592.

(18)   West, J.; Karamata, B.; Lillis, B.; Gleeson, J. P.; Alderman, J.; Collins, J. K.; Lane, W.; Mathewson, A.; Berney, H. *Lab Chip* **2002**, *2*, 224-230.

(19)   Eijkel, J. C. T.; Dalton, C.; Hayden, C. J.; Burt, J. P. H.; Manz, A. *Sensors and Actuators B* **2003**, *92*, 215-221.

(20)   Homsy, A.; Linder, V.; Lucklum, F.; de Rooij, N. F. *Sensors and Actuators B-Chemical* **2007**, *123*, 636-646.

(21)   Anderson, E. C. PhD dissertation, University of Arkansas, Fayetteville, AR, 2006.

(22)   Grant, K. M.; Hemmert, J. W.; White, H. S. *Journal of Electroanalytical Chemistry* **2001**, *500*, 95-99.

(23)   Lee, J.; Ragsdale, S. R.; Gao, X.; White, H. S. *Journal of Electroanalytical Chemistry* **1997**, *422*, 169-177.

(24)   Ragsdale, S. R.; Grant, K. M.; White, H. S. *J. Am. Chem. Soc.* **1998**, *120*, 13461-13468.

(25)   Ragsdale, S. R.; Lee, J.; Gao, X.; White, H. S. *Journal of Physical Chemistry* **1996**, *100*, 5913-5922.

(26)   Ragsdale, S. R.; Lee, J.; White, H. S. *Analytical Chemistry* **1997**, *69*, 2070-2076.

(27)   Ragsdale, S. R.; White, H. S. *Analytical Chemistry* **1999**, *71*, 1923-1927.

(28)   Dass, A.; Counsil, J. A.; Gao, X. R.; Leventis, N. *Journal of Physical Chemistry B* **2005**, *109*, 11065-11073.

(29)   Leventis, N.; Chen, M.; Gao, X.; Canalas, M.; Zhang, P. *Journal of Physical Chemistry B* **1998**, *102*, 3512-3522.

(30)   Leventis, N.; Dass, A. *Journal of the American Chemical Society* **2005**, *127*, 4988-4989.

(31)   Leventis, N.; Gao, X. *Journal of Physical Chemistry B* **1999**, *103*, 5832-5840.

(32)   Leventis, N.; Gao, X. *Journal of the American Chemical Society* **2002**, *124*, 1079-1086.

(33)   Aguilar, Z. P.; Arumugam, P. U.; Fritsch, I. *Journal of Electroanalytical Chemistry* **2006**, *591*, 201-209.

(34)   Arumugam, P. U.; Clark, E. A.; Fritsch, I. *Anal. Chem.* **2005**, *77*, 1167-1171.

(35)   Grant, K. M.; Hemmert, J. W.; White, H. S. *J. Am. Chem. Soc.* **2002**, *124*, 462-467.

(36)   Leventis, N.; Gao, X. *Analytical Chemistry* **2001**, *73*, 3981-3992.

(37)   Wilkes, J. S.; Williams, M. L.; Musselman, R. L. *Electrochemistry* **2005**, *73*, 742-744.

(38)   Anderson, E. C.; Fritsch, I. *Anal. Chem.* **2006**, *78*, 3745-3751.

(39)   Clark, E. A.; Fritsch, I. *Anal. Chem.* **2004**, *76*, 2415-2418.

(40)   Weston, M. C.; Anderson, E. C.; Arumugam, P. U.; Yoga Narasimhan, P.; Fritsch, I. *Analyst* **2006**, *131*, 1322-1331.

(41)   Anderson, E. C.; Weston, M. C.; Fritsch, I. *Analytical Chemistry* **2010**, *82*, 2643-2651.

Chapter 2

Investigations of Redox-Magnetohydrodynamic Fluid Flow At Microelectrode

Arrays Using Microbeads

The following chapter was published in a very similar form as:

Abstract

Microbeads are used to track fluid flow over microband electrode arrays to investigate fundamentals of redox magnetohydrodynamics (redox-MHD) in a confined solution. The results may lead toward design of micro total analysis systems with microfluidics based on the redox-MHD concept. Ion flux was generated by reduction and oxidation of electroactive potassium ferri- and ferrocyanide at selected individually-addressable microelectrodes in the array. An external magnetic field was produced by a small, permanent magnet (0.38 T) placed directly below the array with its field perpendicular to the plane of the array. The cross product of ion flux and magnetic field produces a magnetic force (a portion of the Lorentz force equation) that causes the fluid to rotate around the active electrodes. Velocities up to 1.8 mm/s are demonstrated here. The effects on velocities were obtained for different concentrations of redox species, widths of electrodes, gaps between electrodes, and combinations of anodically- and cathodically-polarized electrodes. The microbeads allowed mapping of flow patterns and velocities, both parallel and perpendicular to the array chip. The influence of counteracting shear forces, drag along the walls, and reinforcing flow are discussed. A significant result is the fairly flat flow profile across 650 μm, attained between electrodes that are oppositely biased.

Introduction

There is great interest in microfluidics for directional pumping and mixing so that devices for small volume, high-throughput, and portable chemical analysis may be realized (e.g. micro total analysis systems, µTAS). Magnetohydrodynamics (MHD) is an interesting possible alternative to the more established microfluidic pumping methods (e.g. electrokinetic, mechanical, and centrifugal). Publications on using MHD in microfluidics have been reviewed.[1] A more recent review expands the MHD microfluidics discussion on solutions that contain readily reduced and oxidized (redox) chemical species.[2] Such "redox-MHD" can achieve a great deal of fluid control without introduction of moving parts by inducing convection in the presence of a magnetic field from small permanent magnets. In this case, the faradaic current at an electrode (generated by as little as a few millivolts) causes an ion flux. Thus, bubble generation and electrode dissolution can be avoided. A large range of redox species with different reduction potentials, electron transfer kinetics, reversibility, and solvent solubility (aqueous and non-aqueous) can be chosen. Also, the electrodes can be easily patterned on chips to produce ion flux at desired locations and can operate within confined volumes, channels, and reservoirs. Redox-MHD can simply reverse flow direction, either by altering the potential or sign of the current at the electrode (i.e. changing an anodic reaction to a cathodic one (or visa versa)) or by changing the direction of the magnetic field. There are only a limited number of reports suggesting the use of redox-MHD for microfluidics.[3-9]

MHD in general is governed by the right-hand rule,[10-12]

$$\mathbf{F_B} = \mathbf{j} \times \mathbf{B} \qquad\qquad (1)$$

where $\mathbf{F_B}$ is a body force (in units of N/m^3) called the magnetohydrodynamic force, or simply the magnetic force,[13] $\mathbf{j}$ is the charge or ion flux (Coul/(s m^2))[14], and $\mathbf{B}$ is the magnetic field (T).[15] $\mathbf{F_B}$ is often imprecisely called the Lorentz force ($\mathbf{F_L}$) in the literature. The Lorentz equation, which describes the electromagnetic force exerted on a charged particle, has both magnetic *and* electric field components.[16] $\mathbf{F_B}$ is actually only the magnetic component of the Lorentz force. (Vectors are denoted here in bold-face.)

Despite the mathematical simplicity of eq. 1, it is not trivial to predict MHD-generated fluid velocity from experimental parameters. For example, the current, i, passing through an electrode, does not provide a spatial representation of $\mathbf{j}$ in solution needed to calculate $\mathbf{F_B}$ in three dimensions. Also, the relationship between the fluid velocity and $\mathbf{F_B}$ depends on additional factors important to the fluid dynamics. These include the location of walls relative to where $\mathbf{F_B}$ is generated, the viscosity of the solution, counteracting flows or shear stress, and reinforcing flows. Thus, the first step toward understanding how MHD can be used to control microfluidics is to visualize the fluid flow in a confined, small volume system that has the capability to vary where $\mathbf{F_B}$ is generated, its direction, and its magnitude.

To begin to address this need, individually-addressable, microband electrode arrays were used here in a small cell containing a solution of both the oxidized and reduced forms of a redox species. The movement of polystyrene latex microbeads in this cell tracked the fluid flow. The only report to-date, involving an electrode array to investigate redox-MHD, was that of Nishiyama and Aogaki,[17] but convection could only be inferred from changes in current rather than by direct observation. In addition, only

one set of dimensions was evaluated (130 bands, 2 mm x 10 μm electrodes with 5 μm gaps between them), and because the electrodes of the array were interdigitated (not individually-addressable), varied spatial control of $\mathbf{F_B}$ was not possible.

Our approach of varying the number and location of active anodes and cathodes and monitoring fluid flow with microbeads also clearly deviates from other studies that made use of particles to investigate MHD fluid flow. Those include studies that use microbeads but were not performed in the presence of redox species: AC MHD micropumps,[18-20] a switch,[21] a high current density DC MHD micropump,[22] and a circular cylinder.[23] Particle image velocimetry (PIV) also has been performed.[24-26] The only PIV investigation[25] that involves redox species (copper ions) provided a spatial resolution of only 0.5 mm in a large electrochemical cell. (A resolution of at least 10-μm is needed for small electrochemical cells like the ones we describe here.) In-situ-generated bubbles have been used to track fluid flow in a redox system,[27] instead of particles, but only velocities near the bubble-generating electrode can be monitored and the large density mismatch between the bubbles and solution can cause localized convection.

Tracking particles possesses benefits over the use of colored solutions, which is another way to image fluid flow. Although many more redox-magnetoconvection studies have imaged fluid flow with colored redox species[8, 9, 28-32] generated *in situ*, and with dyes,[33-37] they suffer from the inability to monitor microscopic convective paths contained within the colored regions. Scanning electrochemical microscopy[8, 31] with simultaneous monitoring of colored redox species has been used, with the same limitation.

The use of an individually-addressable microelectrode array and tracking of microbeads to follow fluid flow has revealed exciting characteristics about redox-MHD that were not previously observed and are elaborated herein. To obtain these outcomes, the effective gap between and "width" of active electrodes was varied by changing which electrodes and how many were under potential control. The potential applied and redox species concentration were also investigated. A solution containing 0.1 M KCl with a 1:1 mole ratio of ferri- and ferrocyanide was used in these studies.

Experimental

Chemicals and materials. All chemicals were reagent grade and used as received. Aqueous solutions were prepared with deionized water from a PURELAB ULTRA Scientific ELGA Labwater filtration system. Potassium ferricyanide ($K_3Fe(CN)_6$) was obtained from EM Science (Gibbstown, NJ). Potassium ferrocyanide trihydrate ($K_4Fe(CN)_6 \cdot 3H_2O$) was purchased from J. T. Baker (Phillipsburg, NJ), and potassium chloride (KCl) was acquired from Aldrich Chemical Co. (St. Louis, MO). Polystyrene latex microspheres (10 μm diameter, 2.5 wt% dispersion in water) were obtained from Alfa Aesar (Ward Hill, MA). Sylgard® 184 silicone elastomer base, Sylgard® 184 silicone elastomer curing agent, and OS-30 solvent, (Dow Corning Corp.) were used to form poly(dimethyl siloxane) (PDMS) films. Microscope slides (precleaned, 3 in. x 1 in. x 1.2 mm), were obtained from VWR. Small pieces cut from a gold coin (Canadian Maple Leaf, 99.99%) placed in a molybdenum boat (Kurt J. Lesker Co., Pittsburgh, PA) and a chromium-plated tungsten rod (Kurt J. Lesker Company, Clairton, PA) served as sources for metal deposition. Silicon wafers (125-mm diameter, 600-650-μm thickness, and (100) orientation) with 2-μm, thermally-grown SiO_2,

purchased from Silicon Quest International, were used as substrates for the microband electrode arrays. Benzocyclobutene, BCB, (Cyclotene 4024-40) was obtained from Dow Chemical Company. Electrical connection of the potentiostat to on-chip contact pads was made using an edge connector (solder contact, 20/40 position, 0.05 in. pitch) from Sullins Electronics Corp. (San Marcos, CA).

Microelectrode array design. Each 1 in. x 1 in. chip contains an array of 16, individually-addressable microband electrodes (Figure 2.1a). The band electrodes are 2 mm long with nominal widths of 25, 50, or 100 μm, and separated by 25-, 50-, or 100-μm gaps, respectively. Actual widths and lengths, measured using an optical microscope, are reported elsewhere in this chapter. In general, the widths were smaller than nominal values by ~10 μm (with a corresponding increase in the gaps).

Each chip contains two large conductors (8 mm x 4.5 mm each) used as counter electrodes and two large band electrodes (6 mm x 0.5 mm each), located 1.0 mm from the counter electrodes, used as pseudo-reference electrodes. These large electrodes are too far from the array to affect electrochemistry there during an experiment. Photodefinable BCB was used to insulate the electrode leads (which connect the electrodes to the contact pads on the top of the array chip), exposing only the electrode array, counter, and reference electrode regions to solution when the bottom half of the array chip is immersed. The array chips were fabricated with photolithography using photoplot masks (Advance Reproductions Corporation, North Andover, MA). Two masks were required, one for the metal electrode layer and one for the BCB layer. The design of the photoplot masks allows 12 array chips to be fabricated on a single 125 mm diameter silicon wafer. The oxidized silicon wafers were used as substrates for fabrication. The SiO_2 layer

serves as insulation between the semiconducting silicon and the conductive gold. The electrode layer consists of 50 Å Cr (for adhesion) and 500 Å Au, both deposited with an Edwards 306 Auto thermal evaporator without breaking vacuum between deposition of the two metals. The gold-covered wafers were spin-coated with 4 μm of positive photoresist (AZ4330RS). Then, the photoresist was patterned using a photoplot mask, and exposed areas were dissolved away by AZ400K photoresist developer (Hoechst-Celanese). The unexposed areas of photoresist, which remained on the wafer after the development step, protected the underlying metal from the wet metal etch step. The Au was etched for ~1 min with a solution of KI (50 g) and I_2 (12 g) in water (500 mL), and the Cr was etched for ~30 s with CEP-200 Chrome Etchant (Microchrome Technology, San Jose, CA). Then, the photoresist was removed with acetone.

Wafers were then spin-coated with 5 μm of BCB (a negative photoresist), using VM652 adhesion promoter (HD Microsystems). A soft-bake of the BCB was performed for 20 min at 70 ^{0}C. Then, BCB was patterned using the second photoplot mask and unexposed areas were dissolved away by DS2100 developer (Dow Chemical Company). The wafers were then rinsed with T1100 rinse solvent (Dow Chemical Company). The BCB was cured at 150 ^{0}C for 15 min, and at 250 ^{0}C for 60 min. A descumming procedure was then performed with reactive ion etching (RIE) to remove the polymer residue that remains behind in the developed regions. The 90 s RIE program used a mixture of O_2 (32 sccm) and SF_6 (8 sccm) at 250 mtorr and 200 W RF power (Unaxis PlasmaTherm SLR 720). After the RIE, the wafers were diced into 1 in. x 1 in. chips, shown in Figure 2.1.

PDMS (Poly(dimethyl siloxane)). PDMS films were made with a 10: 1 weight

ratio of base to curing agent. The elastomer and curing agent mixture were degassed in a

vacuum dessicator for 30 min. Microscope slides were rinsed with OS-30 solvent, dried

with nitrogen gas, and further dried by heating at 65 ^{o}C for 10 min. The degassed PDMS

was spread to a fairly uniform film thickness on the microscope slides by spin-coating for

60 s at different spin-rates. The PDMS was then cured at 100 ^{o}C for 1 h. The cured

PDMS film was peeled away from the microscope slides by hand, and the thickness was

measured using digital calipers (Silver Swallow). A spin rate of 200 rpm resulted in a

PDMS thickness of ~350 μm, and 100 rpm resulted in ~650 μm. Arectangular opening

(approximately 1.5 x 0.7 cm), which defines the dimensions of the electrochemical cell,

was cut in the PDMS using a razor blade.

Magnetic field. A 1 in. x 1 in. x 0.5 in. permanent, NdFeB sintered magnet (1.23

T residual induction, 0.55 T on the surface, Magnet Sales Co.) was used for the redox-

MHD studies. The array chip was placed directly on the magnet. The north pole pointed

downward, perpedicular to the plane of the chip. The magnetic field at the array was

measured to be 0.38 T by a DC magnetometer (AlfaLab Inc.). The vertical component of

B measured 650 μm above the array was 0.366 T, corresponding to a variation of ~4% or

gradient of ~22 T/m. The lateral variation of **B** across the array (~3 mm x ~3 mm) is

estimated to be ~0.2% or a gradient of ~0.2 T/m.

Experimental set-up. Figure 2.1c illustrates the experimental setup. A free-

standing PDMS film was placed directly on the array chip with the rectangular opening

exposing the array region and portions of the counter and pseudo-reference electrodes.

The opening was filled with a solution containing redox species, electrolyte, and
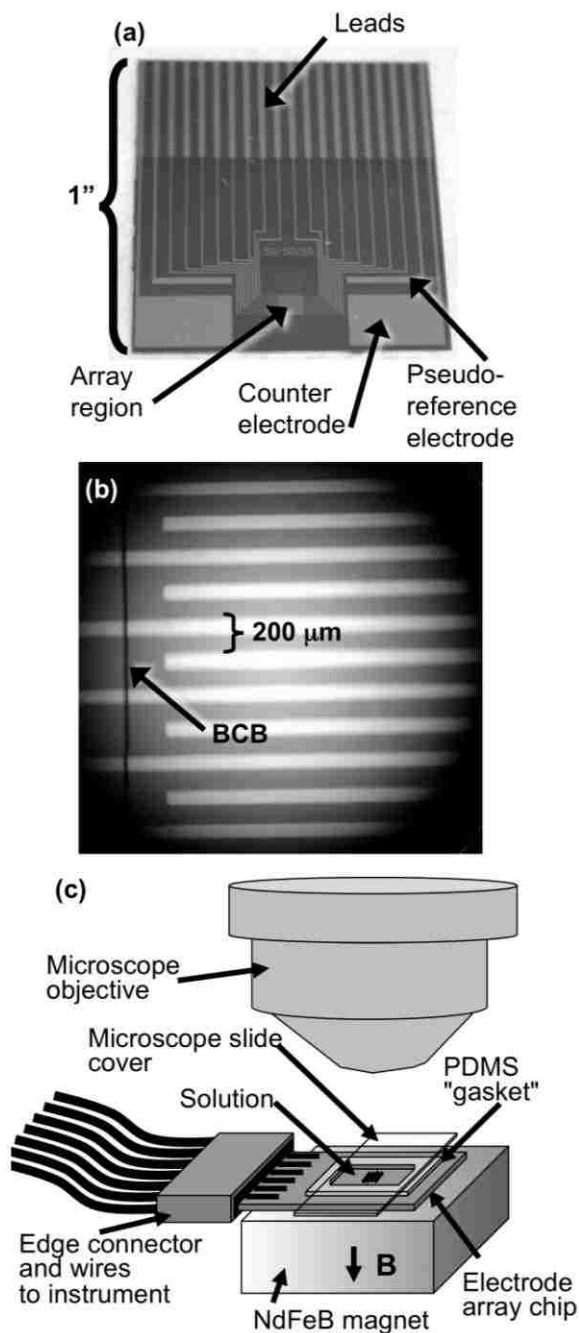
Figure 2.1. (a) Completed array chip after dicing. (b) Optical microscope image of Au array electrodes (11 of 16 bands are shown) with BCB insulator visible to the side of the array region. These microband electrodes were designed with nominal dimensions of 2 mm length, with 50 μm width, having 50 μm gaps between them. Arrays were also fabricated with nominal microband widths of 25 μm and 100 μm, having gaps of 25 μm and 100 μm, respectively. (c) Assembly of electrochemical cell for viewing the motion of microbeads resulting from magnetoconvective effects at an array of microband electrodes.

microbeads. A 1-in. x 0.75-in. piece of microscope slide was placed on top of the PDMS as a lid, creating a closed electrochemical cell, with a height determined by the PDMS thickness (either 350 μm, 480 μm, or 650 μm, as indicated in the figure captions) and a length and width determined by the rectangular opening cut into the PDMS. The solution could be used for about 90 s before the beads rose to the top due to the density mismatch with the solution. Therefore, every bead-tracking experiment was performed with fresh solution. Bead movement was observed with a Nikon Eclipse ME600P microscope, and movies were recorded using a Nikon COOLPIX 990 digital camera (15 frames per second with 350 x 240 pixels per frame).

Average speeds (called linear bead velocities) and standard deviations were calculated from several microbeads. The speed was determined from the distance a bead traveled, using the electrode array as a length scale, over a given time based on the time stamp on the video recording. Unless otherwise stated, linear bead velocities were obtained only from beads that met the following conditions: beads were located approximately half-way between the array chip and microscope slide, moving along the lengthwise axis of the electrodes, and either 300-400 μm away laterally (horizontally) from the center of a single set of active electrodes or in the case of a reinforcing flow configuration, approximately half-way between the oppositely-biased electrodes. Because the flow profile was fairly flat between oppositely-biased electrodes that produced reinforcing flow, velocity measurements were more reproducible in that configuration than bead velocities measured along the length of a single active electrode. Particle imaging velocimetry (PIV) images were generated using DynamicStudio v.3.00 software (Dantec Dynamics, Copenhagen, Denmark).

Viscosity measurements. The viscosity measurements were performed at 24 ºC using a Cannon-Fenske Routine type viscometer size 50, no. 1556 (Industrial Research Glassware, Kenilworth, NJ). The procedure for measuring viscosities followed the manufacturer's guidelines. The viscometer was calibrated with deionized water to determine the viscometer constant which was then used to determine viscosities of all other solutions.

Electrochemical control. A CHI 760B bipotentiostat (CH Instruments, Austin, TX) was used for cyclic voltammetry (CV) and chronoamperometry (CA) in a three- and four-electrode configuration. Unless otherwise specified, the solution contained 0.3 M $K_3Fe(CN)_6$, 0.3 M $K_4Fe(CN)_6$, and 0.1 M KCl, and the on-chip Au counter and pseudo-reference electrodes were used. The suspension of microbeads was pipetted into the redox solution to achieve a 30X dilution (from 2.5% to 0.083% wt dispersion), and thereby diluted each form of the redox couple to 0.29 M.

The 1:1 mole ratio of oxidized and reduced redox species supplied the counter electrodes with sufficient electroactive molecules to allow current to flow there without requiring its potential to shift to extreme values that would corrode the electrode by oxidation or electrolyze water and produce interfering bubbles. Also, the 1:1 mixture stabilizes the potential of the bare Au pseudo-reference electrode at $E^{\circ'}$. Anodic currents are reported here and are expressed as the *absolute* value of the averaged steady-state current. Current densities were determined by dividing the measured current by the combined area of active electrodes that were shorted together to form the "working" electrode. (The gaps between shorted electrodes were not included in this combined area.)

Results and Discussion

      Electrochemical characterization of the microband electrodes. Typical cyclic

voltammograms and chronoamperograms collected at a single working electrode having

three different widths are shown in Figure 2.2. The composition of the solution was 0.3

mM $K_3Fe(CN)_6$, 0.3 mM $K_4Fe(CN)_6$, and 0.1 M KCl. The low redox concentration was

chosen so that diffusion (and not convection due to density gradients which occur at the

high concentrations) is the only significant form of mass transfer that contributes to the

current response. The solid curves in Figure 2.2 were obtained using the horizontal setup

without any glass lid, PDMS gasket, or magnet so that comparisons of the

electrochemical responses could be made to theoretical predictions.

      The CV responses exhibit the expected sigmoidal-shape at the smallest electrode

and increasing peak shapes for the larger electrodes at the same scan rate. This is

because radial diffusion dominates mass transfer at this time scale and for the smallest

band widths. The peak-shaped responses obtained for the larger band widths illustrate an

increasing contribution to mass transfer from linear diffusion. Because both forms of the

redox couple are present, the current is non-zero at both oxidizing and reducing

potentials.

      The half-wave potential ($E_{1/2}$) is 0 V vs. the Au pseudo-reference electrode. This

is expected, based on the Nernst Equation,[38]

$$E = E_{1/2} + (RT/nF) \ln([O]/[R])$$

where R is the ideal gas constant, T is the absolute temperature, n is the number of

electrons transferred per molecule of redox species (n = 1 for the

ferricyanide/ferrocyanide redox couple), F is the Faraday constant 96485.3 Coul/mol electrons, and [O] and [R] are the molar concentrations of the oxidized and reduced forms of the redox couple, respectively. The $E_{1/2}$ is equal to the sum of the standard potential, $E°$, and two terms that account for activity coefficients (γ), $(RT/nF) \ln(\gamma_O/\gamma_R)$, and diffusion coefficients (D), $(RT/nF) \ln(D_R^{1/2}/D_O^{1/2})$.

Although CV is more diagnostic than CA, most of the magnetoconvective studies involve monitoring microbead movement after the electrode potential is stepped to an oxidizing or reducing potential. Thus, examples of CA responses when the potential is stepped to oxidizing values (+0.3 V) are also provided in Figure 2.2. A pseudo-steadystate, diffusion-limited current is achieved for all three band widths at long times.

The pseudo-steady state CA current at three different band widths, 15 μm, 42 μm, and 91 μm (29, 39, and 51 μA, respectively) are within 0.2%, 0.3%, and 0.4% of theoretical values, respectively. The theoretical values were determined using an equation in which the current at long time scales, when the diffusion layer is larger than the electrode size, can be modeled by that at a hemicylindrical electrode.[39]

$$i(t) = 2 \, n \, F \, D \, l \, C^* \, \pi \, / \ln[4 \, D \, t \, / \, r_o^2] \qquad (4)$$

where D is the diffusion coefficient (6.5×10^{-6} cm^2 s^{-1} for $K_4Fe(CN)_6$ at 25° C),[40] l is the electrode length, C^* is the concentration of redox species, t is the time, and r_o is the electrode radius which may be substituted by the electrode band width / 4.

CV and CA were also carried out in solutions with low redox concentrations at two enclosed configurations formed by adding the lid with a PDMS spacer. One of those configurations included the magnet (as in Figure 2.1) and the other did not. The dashed
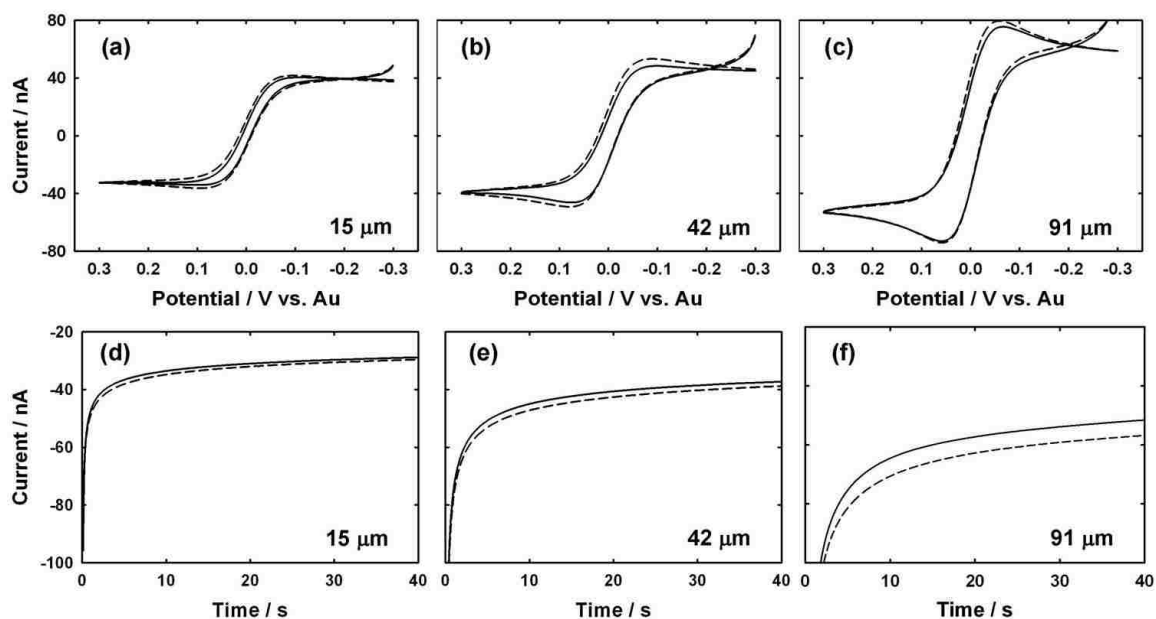
Figure 2.2. Typical electrochemical responses at a single working electrode at three different widths in solution of low redox concentrations (0.0003 M $K_3Fe(CN)_6$, 0.0003 M $K_4Fe(CN)_6$, 0.1 M KCl), without the magnet, using the on-chip counter and pseudo-reference electrodes. Solid curves indicate experiments with the open-cell configuration and dashed curves represent those with the closed-cell configuration (at 480 μm PDMS thickness). Cyclic voltammograms (5 mV/s) and chronoamperograms (stepped to +0.3 V) are shown for a band electrode at the following widths: (a) and (d) 15-μm, (b) and (e) 42-μm, and (c) and (f) 91-μm.

curves in Figure 2.2 are responses for the closed electrochemical cell in the absence of the magnet. The presence of the magnet caused no additional changes in responses in the enclosed electrochemical cell (not shown), as would be expected for low redox concentrations (which generate low faradaic current, low $\mathbf{j}$ values, and therefore low $\mathbf{F_B}$).

The effect of the lid seems to be two-fold. First, it changes a semi-infinite system into a more finite one. Second, because redox species are trapped, the passive equilibration from neighboring electrodes that are within the diffusion length (~390 μm) has a greater effect. However, because the active microband electrode is narrower than the cell height, new redox species can still arrive from a radial direction, and thus, true thin-layer behavior will not be displayed. This explanation is supported by a CA current that is initially larger in magnitude (by ~20% at 20 s) than that without the lid because of an initial increased concentration gradient from passive neighboring electrodes, but has a faster fall-off in time, due to depletion of the diffusion layer laterally outward. The CV responses became more peak-shaped when the electrochemical cell became enclosed, consistent with slight thin-layer-like behavior. This was especially noticeable at the narrowest electrodes, which are more dominated by radial diffusion than the wider ones when the lid is off.

Figure 2.3 provides examples of CV and CA responses at the intermediate electrode width in the enclosed cell with and without the presence of the magnet in solutions containing the high redox concentrations that are used in the MHD studies. These concentrations are a factor of 1000 of that used to produce Figure 2.2. The density gradient generated under oxidizing conditions produces an oscillating pseudo-steadystate current that is present in both CV and CA experiments. The volume element adjacent to

28
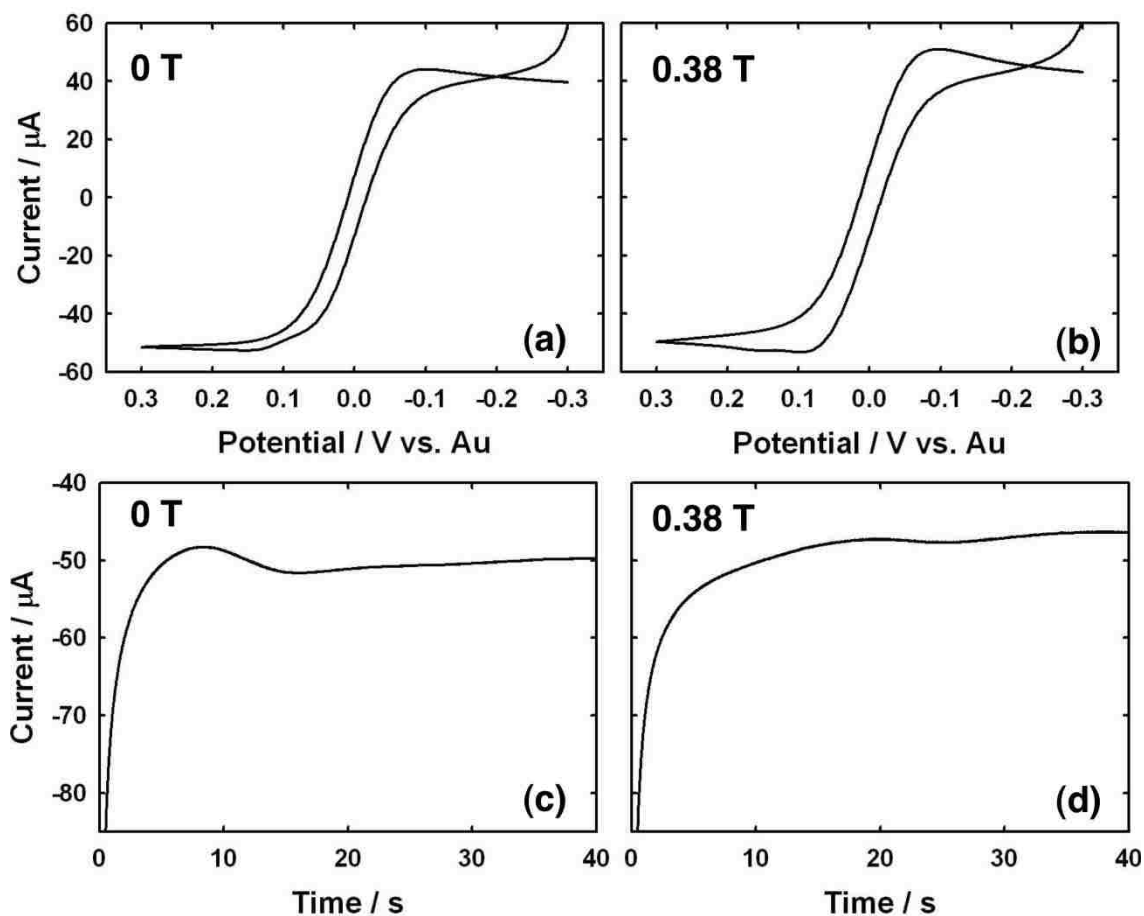
Figure 2.3. Electrochemical responses at a single 42 μm band electrode in a solution of 0.300 M $K_3Fe(CN)_6$, 0.300 M $K_4Fe(CN)_6$, 0.1 M KCl using the on-chip counter and pseudo-reference electrodes. Experiments were performed in the closed cell configuration using a PDMS thickness of 480 μm. Cyclic voltammograms collected at 5 mV/s in the (a) absence of the magnet, 0 T, and (b) in the presence of the magnet, 0.38 T. Chronoamperometry experiments performed at +0.3 V vs Au pseudo-reference in the (c) absence of the magnet, 0 T, and (d) in the presence of the magnet, 0.38 T.

29

the electrodes on the floor of the electrochemical cell becomes less dense than the surrounding solution when $Fe(CN)_6^{4-}$ is converted to $Fe(CN)_6^{3-}$.[41] Those volume elements rise and are replaced with the surrounding solution, causing convection and variations in flux of redox molecules and therefore variations in current. The presence of the magnet has a "dampening effect" on the current response, suggesting that another force, presumably $\mathbf{F_B}$, levels out the natural convection. Density-gradient-caused convection does not occur during cathodic events, as is supported by the smooth reduction curve of the CV response (Figure 2.3) and in flattened cathodic CA responses (not shown). This is because volume elements containing the reduced form of the redox species are more dense than the surrounding solution and remain against the chip.

Other than the "dampening effect" during oxidation, there is no other obvious enhancement or decrease in the current response. Previous reports of MHD induced convection have involved changes in current as an indicator of magnetoconvection.[8-11, 17, 30, 31, 42-45] It would be difficult to use the more subtle changes shown here to infer details about flow. Thus, there is a need in these small systems with low B fields to monitor the magnetoconvective flow independently of changes in current.

Effects on fluid velocity by changing redox concentrations and applied potential at single biased electrodes in the presence of a magnetic field. The schematic in Figure 2.4a shows a rotational path expected for $\mathbf{F_B}$ around a single biased electrode when the magnetic field is perpendicular to the lateral (horizontal) ion flux (according to eq. 1). As expected, microbeads in the solution exhibited rotational motion.

It does not appear that the beads experience F_B directly. Although the beads possess negative charges from sulfate groups, there is no net ion flux perpendicular to the magnetic field, because the beads are evenly distributed laterally. Also, spherically-distributed ion gradients at each bead's surface (its double layer) cancel out. Thus, bead movement may be interpreted as resulting from momentum transfer and can be used to track fluid flow.

The ion gradient, and therefore F_B and fluid velocity, can be controlled by changing the current generated at the electrode. One way to do this is to change the concentration of the redox species. Figure 2.4b shows bead velocities resulting from a 44-μm-wide band electrode held at an oxidizing potential at the mass-transfer limit in a solution containing 0.0100, 0.025, 0.050, 0.100 and 0.300 M each of ferricyanide and ferrocyanide. The higher concentrations result in higher currents and therefore larger ion gradients, F_B values, and linear fluid velocities. The linear velocity of 150 μm/s that was attained with 0.300 M at a single electrode is comparable to the lower values achieved by electrokinetic pumping in channels.[46]

The dependence of current and velocity on concentration is linear, yielding best-fit equations of $y = 0.16 \ \mu A \ mM^{-1} + 0.199 \ \mu A$ ($R^2=1$) and $y = 0.50 \ \mu m \ s^{-1} \ mM^{-1} + 6.05$ $\mu m \ s^{-1}$ ($R^2=0.992$, see Figure 2.4b), respectively. Viscosities varied by about 12% from 0.000902 kg/m to 0.00102 kg/m for the 0.100 M and 0.300 M solutions, respectively, and did not have a measurable affect on current or bead velocity.

It has been observed that a threshold value of F_B is needed to generate a change in current.[27, 45, 47] Some investigators have interpreted that result to mean that there is no

convection below this threshold.[10, 48] Our studies show that convection is present, even under conditions (small electrode radius, low redox concentrations, low B-field) that do not exhibit a measurable change in current. This must be because the slow MHD convection does not sufficiently perturb the redox concentration gradient at the microelectrode's surface enough to cause an appreciable change in current. In fact, the lowest redox concentration that was studied here (0.010 M in Figure 2.4b) is lower than any in the redox-MHD literature for a microelectrode at low B-fields where convection has been confirmed. This conclusion re-emphasizes the importance of visualizing the flow.

Another way to change the fluid velocity, without changing solution composition, is to vary the potential applied to the electrode.[3, 5] A plot of velocity as a function of potential at a single biased 44-μm band electrode is shown in Figure 2.4c. For potentials greater than 0.10 V vs. Au pseudo-reference (equivalent to +0.1 V vs. E°'), the anodic current was mass-transfer limited and reached a steady-state of ~45 μA (0.051 A/cm^2). For these potentials, the fluid velocity was ~107 μm/s. When the potential decreased below 0.10 V, the current decreased, following a Nernstian dependence. The decrease in current results in a diminished F_B, which in turn produces a slower fluid velocity. For example, with the potential held at 0.04 V, the anodic current was 25 μA (0.028 A/cm^2), and the fluid velocity was 75 ± 13 μm/s. When the potential was decreased further to 0.02 V, the anodic current decreased to half (13 μA, 0.015 A/cm^2), and the fluid velocity also slowed to half (38 ± 8 μm/s).

Effect of electrode width on fluid velocity. Because there is long-range coupling through solution from the motion of a fluid element, redox-MHD fluid
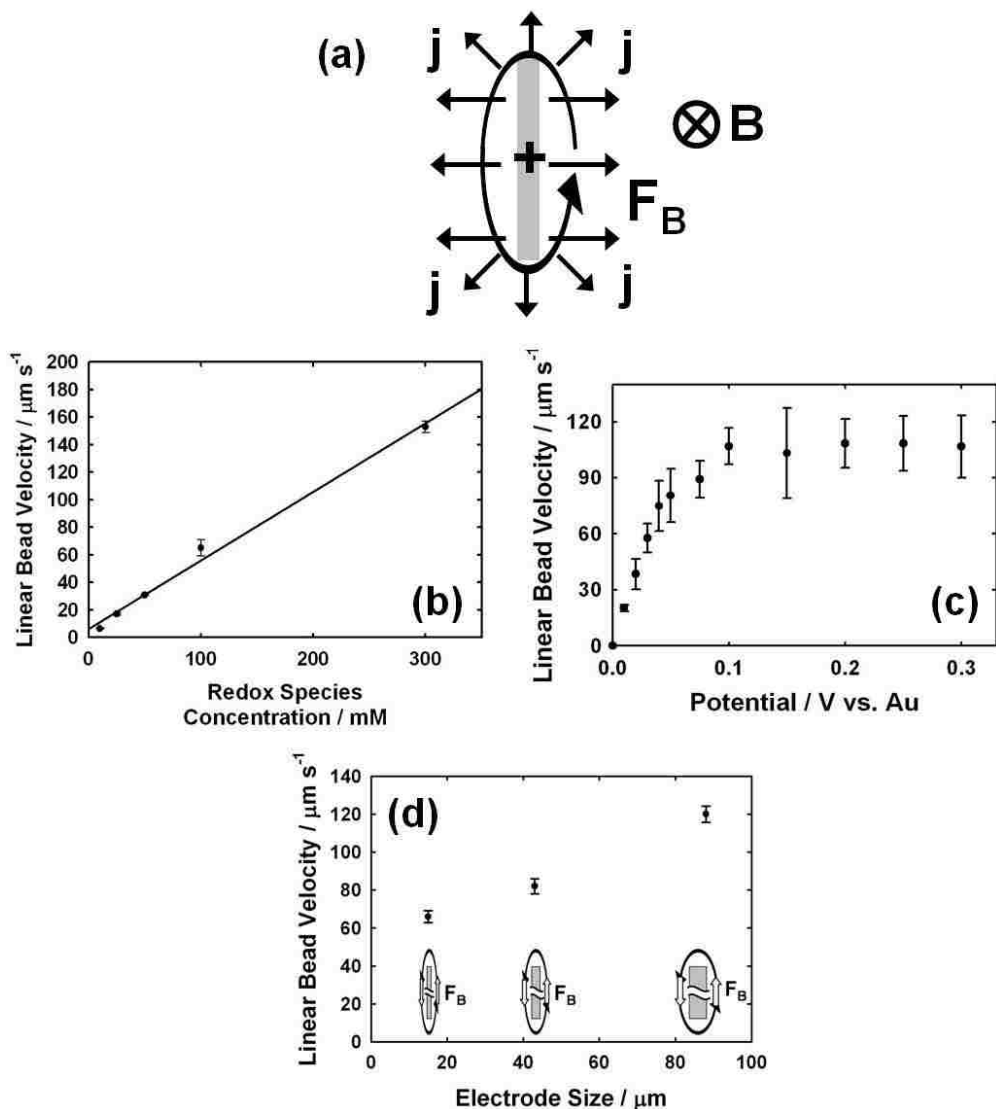
Figure 2.4. (a) Schematic drawing of F_B around a single band electrode that is held at an oxidizing potential. (b) Effect of redox species concentration on flow of solution around a single 44 μm-wide electrode at +0.3 V. [Note: $K_4Fe(CN)_6$ and $K_3Fe(CN)_6$ were each used at the given concentrations.] The observed anodic plateau current is given for each data point. A magnetic field of 0.38 T and a PDMS thickness of 350 μm were used. (c) Effect of potential on fluid velocity, using a solution containing 0.3 M $K_3Fe(CN)_6$, 0.3 M $K_4Fe(CN)_6$ and 0.1 M KCl, where all other conditions are the same as in (b). (d) Dependence of linear bead velocity on the width of a single microband electrode. The anodic potential was controlled to achieve a current of ~27 μA at each electrode using a PDMS thickness of 650 μm. Actual current values (averaged over the 3 s time period in which the microbead velocities were measured) at each of the electrodes are: 27.1 μA (0.0906 A/cm^2) at the 15-μm width, 27.2 μA (0.0316 A/cm^2) at the 43-μm width, and 26.8 μA (0.0152 A/cm^2) at the 88-μm width. Measurements were made at 300 μm above the array and approximately 300 to 400 μm away from the center of each electrode.

33

dynamics depend not only on **j** and **B**, but also on the geometry and dimensions of the electrodes. We observed this affect when comparing band electrodes of different widths. When electrodes of varying sizes are biased to the same potential, the current, and thus the resulting F_B, is greater for larger widths. So, if a faster linear velocity were measured,it could be attributed to the higher current. Therefore, to better determine the effect of electrode size on fluid velocity, the potential was adjusted to achieve the *same* steady-state current at three electrodes, each having a different width. Under these circumstances, it might be expected that a greater F_B at the narrower electrodes due to the larger current density there would produce a faster linear velocity. However, the opposite was observed.

A plot of linear bead velocity as a function of electrode width is shown in Figure 2d. When the same current of ~27 μA was achieved (in the presence of the magnetic field) at 15, 43, and 88-μm wide band electrodes, the resulting fluid velocities were 66 ± 3, 82 ± 4, and 120 ± 4 μm/s, respectively. The corresponding current densities are: ~0.090, ~0.031, and ~0.015 $\mu A/cm^2$, respectively. The slower linear velocities at the narrower electrodes result from shear stress. For rotational flow around a band electrode, the solution experiences shear forces as it moves in one direction along one side of the electrode and in the opposite direction along the other side of the electrode. The closer that two oppositely moving volume elements are, the greater the shear stress is. Thus, a greater current density there might not be enough to offset the increased interaction of these fluid elements. Consequently, slower speeds at narrower electrodes are observed.

Gap between oppositely-biased electrodes (reinforcing flow). When one microband electrode is poised at an oxidizing potential and another at a reducing

potential, the $\mathbf{F_B}$ forces between the electrodes act in the same direction, as shown in Figure 2.5a. If the oppositely-biased electrodes are sufficiently far apart, then no coupling interaction of flow occurs. However, when they are closer together, the fluid motion between electrodes acts in a reinforcing way, resulting in increased linear fluid velocity there. A plot of linear bead velocity between 44-μm wide, oppositely biased electrodes (one at +0.3 V and the other at −0.3 V) as a function of the gap between them is shown in Figure 2.6b and supports this prediction. *The velocity more than doubles, from 104 ± 19 μm/s at a gap of 1.45 mm to 263 ± 14 μm/s at a gap of 650 μm.* This high reinforcing speed exceeds that of 190 μm/s reported previously[3] for much larger electrode dimensions and higher current in a closed channel having an aqueous solution with similar composition and magnetic field. (The maximum speed obtained for our device is described in the "flow profile" section below.) As the gap between the active array electrodes decreases further, the fluid velocity decreases, reaching 60 ± 12 μm/s with a 56-μm gap. The fall-off occurs because the opposing $\mathbf{F_B}$ forces along the outer edges of the two biased electrodes are also closer together, resulting in a decrease in linear velocity between them. The anodic currents observed during the experiments are shown in Figure 2.5b. There is no significant change in current (51-52 μA, 0.058-0.059 A/cm^2) until the gap between biased electrodes is decreased to 56 μm and the observed current increases to 66 μA (0.075 A/cm^2), due to redox cycling between the oppositely biased electrodes. Thus, the change in velocity with gap is solely due to the location of the relative $\mathbf{F_B}$ vectors and the spatial coupling of fluid flow. Even when redox cycling
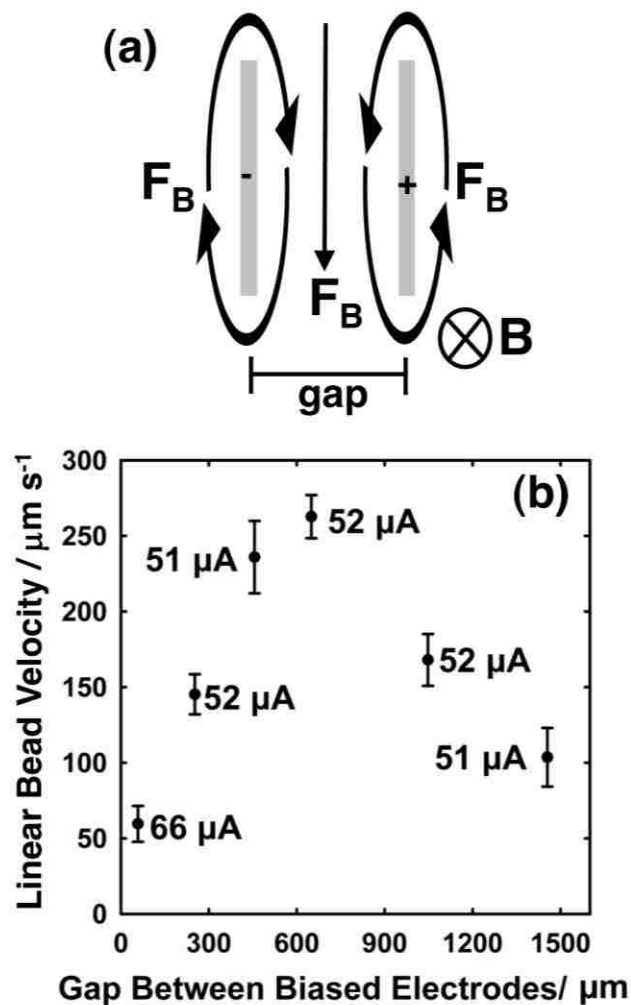
<u>Figure 2.5.</u> Effect of distance between two oppositely biased electrodes on fluid velocity. (a) Schematic drawing of flow between two oppositely biased electrodes. (b) Fluid velocity is plotted as a function of the gap between two 44 µm electrodes (one held at 0.3 V, the other held at -0.3 V). A magnetic field of 0.38 T and PDMS thickness of 350 µm were used. The anodic plateau current is given for each data point.

increases the current, the corresponding increase in $\mathbf{F_B}$ is insufficient to overcome the shear stress from opposing flow directed by the outer edges of the electrodes.

Vertical and horizontal flow profiles. The reinforcing flow configuration with co-planar microband electrodes is somewhat analogous to electrodes that might be on opposite walls of a channel, directing fluid flow down the length of the channel.[3, 4, 49, 50] Although, in the case here, there are no nearby sidewalls along the lengths of the electrodes that would slow fluid movement, a different offsetting force, called the shear force, slows movement, instead. It is of interest, then, to investigate the flow profile over the horizontal and vertial crosssections. These were determined by tracking microbeads and are shown in Figure 2.6. An experimental setup similar to that in Figure 2.5 was used, but with a gap of 650 µm between the two single, oppositely-biased active electrodes to maximize velocity (Figure 2.6a).

Surprisingly, the horizontal flow profile between the biased electrodes (at a fixed height, midway between array and lid) was approximately flat (Figure 2.6b). However, theory for both non-redox and redox-containing solutions predict a parabolic flow profile for the Hartmann ($\ll 1$) and Reynolds (<1) numbers for rectangular, electrode-lined microchannels. The parabolic profile results from a pressure-driven flow, and thus, the corresponding equations have been used to calculate velocity as a function of the pressure differential along the length of the channel.[51] Numerical simulations and analytical solutions for the case of one and two-electrode pairs on the sides of a channel for redox-MHD also propose a parabolic profile.[49, 50] Also, reports of non-redox MHD in confined solutions where velocities were measured show faster fluid flow in the center of the cell than near the walls where the electrodes reside.[18-22]

We can speculate why our lateral velocity profile is approximately flat and not parabolic. The greatest $\mathbf{F_B}$ force is generated by net ion movement in the diffusion layer near the electrodes. The movement of solution in this layer causes neighboring solution to move due to viscous forces, resulting in a flat flow profile, similar to that of electrokinetic pumping, but over a larger distance (in this case, 650 μm). However, the lack of sidewalls immediately adjacent to and along the lengths of the microband electrodes, possibly in combination with the non-uniform ion flux extending from the electrodes laterally, is likely to play a major role.

The dependence of fluid velocity on height above the electrode array chip was determined by raising the focus of the microscope objective and determining the speed of the microbeads that were in focus. Fluid velocity measurements were made at 100 μm intervals (corresponding to a fraction of a revolution of the fine focus knob of the microscope and based on a calibration) above the surface of the chip. The 100 μm interval was selected because this was the smallest height change that allowed the viewing of a completely different set of microbeads from those measured at other heights. For this experiment, 650 μm thick PDMS was used to allow the collection of more data points than would have been possible with the 350 μm thick PDMS used in our other experiments. The same electrode dimensions and reinforcing flow arrangement used for the lateral profile was also used for the vertical profile. A schematic drawing of a cross-section of solution with 10 μm microbeads above the array chip is shown in Figure 2.7c. Due to the lower density of microbeads (compared to the surrounding solution), more beads are located closer to the glass slide at the top of the solution than they are to the array chip. Also, microbeads *in contact* with the glass slide do not move with the flow of
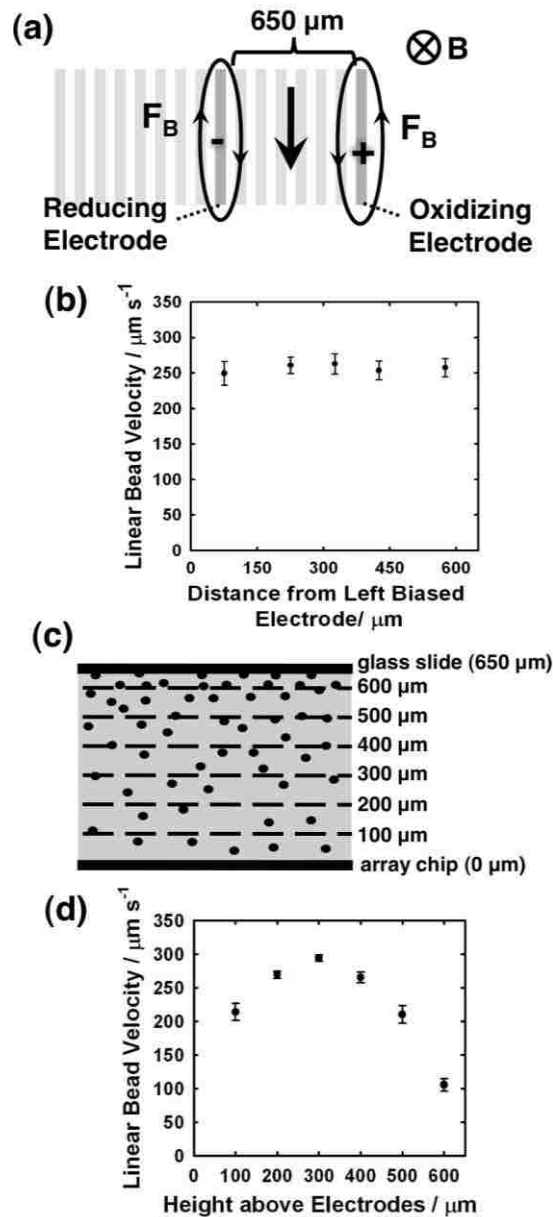
Figure 2.6. Flow profiles between two oppositely biased electrodes at 0.38 T. (a) Schematic drawing of flow between two oppositely biased 44 μm electrodes separated by 650 μm gap. The reducing electrode at -0.3 V is defined as 0 μm, and the oxidizing electrode at +0.3 V is defined as 650 μm. (b) Fluid velocity is plotted as a function of location between the two electrodes. The cell height was 350 μm. (c) Schematic drawing of cross-section of solution with microbeads above the array chip, showing where the velocities were measured to create the plot in (d). More beads are closer to the lid than to the array chip because they are less dense than the solution. (d) Fluid velocity obtained midway (~325 μm) between the two active 44 μm-wide electrodes as a function of height above the array chip. The cell height was 650 μm. The dashed curve is the best fit (u_{max} = 307 μm/s at R^2 = 0.819) for the data based on Poiseuille flow (parabolic profile) between two plates separated by 650 μm.

solution. Fluid velocity data as a function of height above the array chip are shown in Figure 2.6d.

The Hartman number, Ha, indicates the expected flow profile in an MHD experiment. Ha^2 is the ratio of the Lorentz forces to viscous forces and is defined by

$$Ha \ \blacksquare Bw \sqrt{(\blacksquare} \tag{5}$$

where w is half the distance between the plates, σ is the fluid conductivity, and μ is the viscosity. For flow between two stationary parallel plates with low (<<1) Hartmann numbers, a parabolic velocity profile is predicted that is characteristic of pressure-driven, Poiseuille flow.[51] This is certainly the case for the ferricyanide/ferrocyanide solution used in our experiments. The Ha value is approximately 0.0026 for a 650 μm high cell and 0.00036 for a 90 μm high cell (where B = 0.38 T, σ = 0.5 S/m,[52] μ = 1.10 x 10^{-3} kg/(m s))[53].

Given the low Hartman number for these experiments, we may proceed to fit the data in Figure 2.6d to a parabola. The fluid velocity, u, between parallel plates for pressure-driven flow is given by

$$u \ \blacksquare u_{max}(1 \ \blacksquare \frac{y^2}{w^2}) \tag{6}$$

where y is equal to the distance from the centerline between the two plates toward one of the plates. Therefore, fluid velocity is expected to equal 0 at the plates and a maximum value, u_{max}, at the centerline between the two plates.

The above equation holds under laminar conditions. These are expected when the Reynolds number, Re, is less than unity. Re is the ratio of inertia forces to viscous forces:

$$Re = \rho \mathrm{v} l / \mu, \qquad\qquad\qquad (7)$$

where v is the mean velocity, l is the characteristic length or hydraulic diameter ($D_h = 4$ x cross sectional area/wetted perimeter = 2 x separation (2w) between infinite parallel plates),[54, 55] and ρ is the density. Re values for our conditions ($\rho = 1127.6$ kg/m^3 and $\mu = 1.10$ x 10^{-3} kg/(m s) at 20 °C)[53] range from 0.018 (for a 90-µm PDMS thickness and 100 µm/s velocity) to 0.80 (for a 650-µm PDMS thickness and 600 µm/s velocity), which are less than unity.

The dashed curve in Figure 2.6d is the best fit of the data to the equation for Poiseuille flow between two plates separated by 650 µm, in the following form:

$$u = u_{max}(1-(x-325)^2/325^2) \qquad\qquad (8)$$

The value of u_{max} (in µm/s) was allowed to be determined by the fit (307 µm/s). Also, u is in units of µm/s, and x is the height above the electrode chip in units of µm.

It is apparent from Figure 2.6d that the experimental data do not closely follow a parabolic flow profile. The R^2 value of the fit is only 0.819. There is a curvature to the experimentally-obtained data where the maximum velocity appears near the middle and a decreased velocity is measured both close to the array chip (defined as a height of x = 0 µm) and the glass slide (x = 650 µm). Interestingly, though, the drop in velocity is shallower toward the floor of the electrochemical cell than it is toward its lid. This further supports the concept of a stronger $\mathbf{F_B}$ at the active electrodes on the array chip, as was suggested in the interpretation of the lateral flow profile. Vertical flow profiles involving applied current, instead of applied potential, which will be reported in Chapter 3, are consistent with this asymmetric behavior.

Maximum flow velocities and profiles. In order to determine the maximum flow rates obtainable for this microelectrode array device, a series of experiments was performed. Initial conditions were chosen to yield the highest current and velocity that were obtained to this point for single oppositely-biased electrodes, namely a reinforcing flow configuration, highest redox concentrations (0.300 M), and 650 μm cell height. The number of electrodes shorted together (one set held at +0.3 V on one side of the array and -0.3 V on the other side) was increased with a corresponding decrease in gap between the innermost oppositely-biased electrodes. A schematic of the electrode configurations resulting in the lowest (configuration a) and highest (configuration e) velocities are in Figures 2.7a and 2.7b, respectively. The yellow electrodes are those held at oxidizing potentials (+0.3 V) and the red are those held at reducing potentials (-0.3 V); the arrow indicates the direction of flow and the asterisk indicates the middle of the array (all measurements in the plot in Figure 2.7c are made relative to it). All other electrode configurations are not shown, but for example, configuration b would correspond to five electrodes at oxidizing potentials and five at reducing potentials, configuration c to four and four, and so on.

The maximum bead velocities were determined at 300 μm above the array and directly centered between the two sets of electrodes, indicated by the asterisk in Figures 2.7a and 2.7b. Maximum velocities decreased as the number of biased electrodes was decreased, as expected, due to a decrease in current with reduced electroactive area. A maximum bead velocity of 1.80 mm/s was achieved when all eight-44 μm electrodes were held at oxidizing potentials and the other eight-44 μm electrodes were held at reducing potentials with a gap of 50 μm between the oppositely-biased sets

(a)

-0.3 V   *   +0.3 V

(b)

config e
config d
config c
config b
config a

Bead Velocity / μm s⁻¹

Distance relative to middle of array / μm

(c)

-0.3 V   *   +0.3 V

(d)

6.059 186.073 366.087 546.101 726.115 906.129 1086.143 1266.157 1446.171 1626.185 1806.199

43
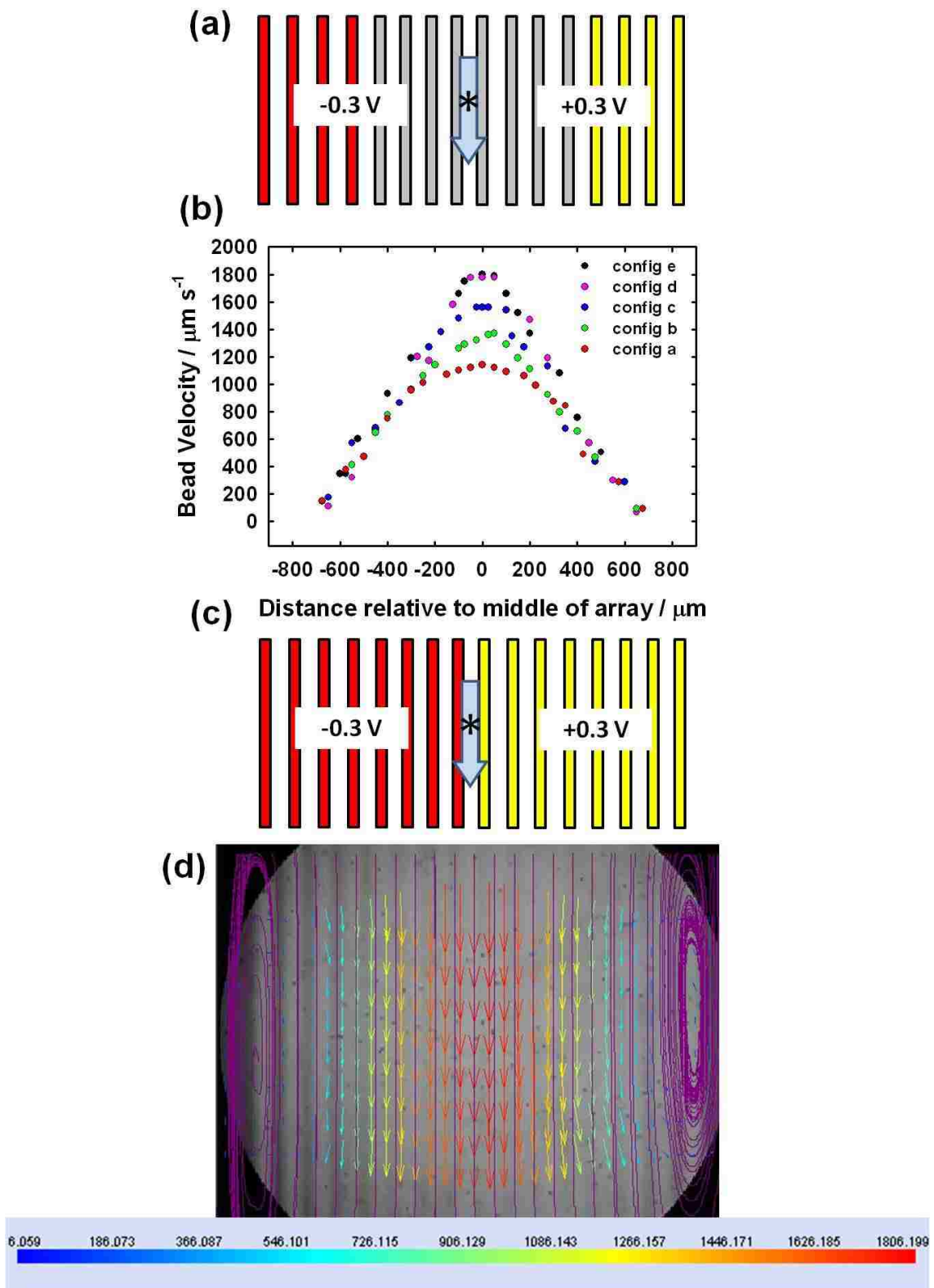
Figure 2.7. (a) Schematic of electrode configuration e. Red electrodes are held at -0.3 V and yellow electrodes are held at +0.3 V. Gray electrodes are not active. The arrow indicates the direction of flow and the asterisk indicates the center of the array, where maximum velocities were determined. Electrode configuration d has five electrodes at oxidizing potentials and five at reducing potentials with five inactive electrodes between; electrode configuration c has six at oxidizing and six at reducing with three inactive between; electrode configuration b has seven and seven with two inactive electrodes between. (b) Plot of bead velocity as a function of distance from the center of the array (indicated by the asterisk in (a) and (c)). (c) Schematic of electrode configuration e, resulting in a maximum velocity of ~1800 μm/s, corresponds to PIV image in (d). (d) PIV image of flow between biased electrodes in configuration a. The colored arrows represent different velocities, as indicated on the scale below. The purple streamlines indicate the overall flow path. The vortices indicate where flow rates are approximately 0 μm/s.

(configuration e). The flow profile, shown in Figure 2.7c for all configurations, between the innermost oppositely-biased electrodes is flat, consistent with the case for reinforcing flow between single electrodes (reported above). Over the electrodes, however, the velocities decreased quickly, reaching ~0 μm/s, at ~$\pm$700 μm from the middle, where the center of rotation for the circular flow was observed. As the number of biased electrodes was decreased, the flow profile flattened due to an increase in distance between the active electrodes. This shifts the center of rotation further from the center of the array and thus, the drop-off in velocity is not as steep, resulting in relatively flat flow profiles. A PIV image for flow in electrode configuration a is shown in Figure 2.7d. Velocities are relatively constant directly in the center of the array (red arrows) and drop off at distances away from the center reaching ~0 μm/s as indicated by the vortices in the streamlines (purple). This image is consistent with the profiles shown in Figure 2.7c.

Conclusions

Our approach to monitor fluid flow at individually-addressable microelectrode arrays has allowed us to observe several significant characteristics of redox-MHD on the small scale that have not previously been reported. (1) We have recorded the lowest redox concentration to-date that produces convection near a microelectrode at a low B-field (0.38 T), which is important toward establishing chemical compatibility with analytes and their analysis (e.g. protein-binding, enzyme activity, and enzyme substrates). (2) Flat flow profiles were demonstrated in the horizontal cross section and have importance in separating mixtures. (3) Electrodes located near walls can offset the zero-slip boundary effect, suggesting that profiles in channels are tunable. (4) The dependence

of fluid speed on reinforcing ($\mathbf{F_B}$ in same direction) flows is essential in designing chip-based redox-MHD devices for both pumping and stirring. (5) Fluid direction can be controlled without channel sidewalls. The latter two characteristics suggest a new "channelless" concept for μTAS devices that could simplify fabrication and allow a single design to be suitable for many different redox-MHD microfluidic applications. Preliminary results on this concept are described in a later chapter. Finally, redox-MHD could offer a significant advantage for applications requiring volumes and flow rates that are too large for electrokinetic pumping.

References

(1)   Qian, S. Z.; Bau, H. H. *Mechanics Research Communications* **2009**, *36*, 10-21.

(2)   Weston, M. C.; Gerner, M. D.; Fritsch, I. *Analytical Chemistry* **2010**, *82*, 3411-3418.

(3)   Aguilar, Z. P.; Arumugam, P. U.; Fritsch, I. *J. Electroanal. Chem.* **2006**, *591*, 200-209.

(4)   Anderson, E. C.; Fritsch, I. *Anal. Chem.* **2006**, *78*, 3745-3751.

(5)   Arumugam, P. U.; Fakunle, E. S.; Anderson, E. C.; Evans, S. R.; King, K. G.; Aguilar, Z. P.; Carter, C. S.; Fritsch, I. *J. Electrochem. Soc.* **2006**, *153*, E185-E194.

(6)   Clark, E. A.; Fritsch, I. *Anal. Chem.* **2004**, *76*, 2415-2418.

(7)   Weston, M. C.; Anderson, E. C.; Arumugam, P. U.; Yoga Narasimhan, P.; Fritsch, I. *Analyst* **2006**, *131*, 1322-1331.

(8)   Grant, K. M.; Hemmert, J. W.; White, H. S. *J. Am. Chem. Soc.* **2002**, *124*, 462-467.

(9)   Leventis, N.; Gao, X. *Analytical Chemistry* **2001**, *73*, 3981-3992.

(10)   Lee, J.; Ragsdale, S. R.; Gao, X.; White, H. S. *Journal of Electroanalytical Chemistry* **1997**, *422*, 169-177.

(11)   Leventis, N.; Chen, M.; Gao, X.; Canalas, M.; Zhang, P. *Journal of Physical Chemistry B* **1998**, *102*, 3512-3522.

(12)   Leventis, N.; Gao, X. *Journal of Physical Chemistry B* **1999**, *103*, 5832-5840.

(13)   Here we have adopted the notation F_B and terminology "magnetic force" from Leventis et al. (see Leventis, N. G., X. Analytical Chemistry 2001, 73, 3981-3992) to represent the magnetohydrodynamic force.

(14)   In an attempt to avoid confusion among the chemistry, e., and physics communities, we have adopted the notation of the lower case j to represent "charge flux" in units of Coul/(s m2), which appears widely in the literature.   The "charge" may be either ions or electrons. We think it is more appropriate than using the captital J or the lower case i, which also appear in the MHD literature. We have chosen not to use the capital J, because in chemistry, J often refers to flux of chemical species and is expressed in different units (mol/(s m2)). Leventis

et al. (see Leventis, N.; Chen, M.; Gao, X.; Canalas, M.; Zhang, P., J. Phys. Chem. B 1998, 102, 3512-3522 and Leventis, N.; Gao, X., J. Phys. Chem. B 1999, 103, 5832-5840) have used the parameter i, instead of J to make this distinction. Although the units of i are Coul/(s m2), the measured current between two electrodes in an electrochemical experiment does not indicate the spatial distribution of ion movement (redox-, electrolyte-, and counter-ions) in the solution. It is the components of local velocities of the ions (at the microscopic level) at right angles to the B-field, not the net current measured in the electrode conductor, that lead to the MHD-induced flow patterns. The letter j, then, is consistent with the definition that means charge "flux", and its lower case indicates that the units are in Coulombs, not in moles.

(15)   The field B is called the "magnetic field" here, which is consistent with the more modern usage of the term. See E. M. Purcell, "Electricity and Magnetism: Berkeley Physics Course", Vol. 2, 2nd ed., 1985, McGraw-Hill, Inc.:Boston, pp. 433-434. It is synonymous with "magnetic flux density" and "magnetic induction" and has units of Tesla, T, (or webers per squared meter, or volt second per squared meter). Historically, the field H was originally called the "magnetic field", but it is more recently known as the "magnetic field strength" or "magnetic field intensity" and has units of amperes per meter.

(16)   Feynman, R.; Leighton, R. B.; Sands, M. *The Feynman Lectures on Physics*; Addison-Wesley: Reading, MA, 1964.

(17)   Nishiyama, S.; Aogaki, R. *Bull. Chem. Soc. Jpn.* **2000**, *73*, 1919-1923.

(18)   Lemoff, A. V.; Lee, A. P. *Sensors and Actuators B* **2000**, *63*, 178-185.

(19)   Sadler, D. J.; Changrani, R. G.; Chou, C.-F.; Zindel, D.; Burdon, J. W.; Zenhausern, F. *Proceedings of SPIE*, San Francisco, CA, 22-24 October 2001; 162-170.

(20)   West, J.; Karamata, B.; Lillis, B.; Gleeson, J. P.; Alderman, J.; Collins, J. K.; Lane, W.; Mathewson, A.; Berney, H. *Lab Chip* **2002**, *2*, 224-230.

(21)   Lemoff, A. V.; Lee, A. P. *Biomedical Microdevices* **2003**, *5*, 55-60.

(22)   Homsy, A.; Koster, S.; Eijkel, J. C. T.; van den Berg, A.; Lucklum, F.; Verpoorte, E.; de Rooij, N. F. *Lab Chip* **2005**, *5*, 466-471.

(23)   Kim, S. J.; Lee, C. M. *Experiments in Fluids* **2000**, *28*, 252-260.

(24)   Andreev, O.; Thess, A.; Haberstroh, C. *Physics of Fluids* **2003**, *15*, 3886-3889.

(25)   Cierpka, C.; Weier, T.; Gerbeth, G.; Uhlemann, M.; Eckert, K. *J. Solid State Electrochem.* **2007**, *11*, 687-701.

(26)   Dattarajan, S.; Johari, H. *Physics of Fluids* **2008**, *20*.

(27)   Mohanta, S.; Fahidy, T. Z. *Can. J. Chem. Eng.* **1972**, *50*, 434-435.

(28)   Leventis, N.; Dass, A. *Journal of the American Chemical Society* **2005**, *127*, 4988-4989.

(29)   Leventis, N.; Gao, X. *Journal of the American Chemical Society* **2002**, *124*, 1079-1086.

(30)   Grant, K. M.; Hemmert, J. W.; White, H. S. *J. Electroanal. Chem.* **2001**, *500*, 95-99.

(31)   Ragsdale, S. R.; White, H. S. *Analytical Chemistry* **1999**, *71*, 1923-1927.

(32)   Pullins, M. D.; Grant, K. M.; White, H. S. *Journal of Physical Chemistry B* **2001**, *105*, 8989-8994.

(33)   Qian, S.; Zhu, J.; Bau, H. H. *Physics of Fluids* **2002**, *14*, 3584-3592.

(34)   Bau, H. H.; Zhu, J.; Qian, S.; Xiang, Y. *Sensors and Actuators B* **2003**, *88*, 205-216.

(35)   Bau, H. H.; Zhong, J. H.; Yi, M. Q. *Sensors and Actuators B-Chemical* **2001**, *79*, 207-215.

(36)   Qian, S.; Bau, H. H. *Sensors and Actuators B* **2005**, *106*, 859-870.

(37)   Xiang, Y.; Bau, H. H. *Physical Review E* **2003**, *68*, 016312.

(38)   Bard, A. J.; Faulkner, L. R. *Electrochemical Methods: Fundamentals and Applications*, 2nd ed.; John Wiley & Sons, Inc.: New York, 2001.

(39)   Aoki, K.; Tokuda, K.; Matsuda, H. *J. Electroanal. Chem.* **1987**, *225*, 19-32.

(40)   Stackelberg, M. v.; Pilgram, M.; Toome, V. *Zeitschrift für Elektrochemie* **1953**, *57*, 342-350.

(41)   Gao, X.; Lee, J.; White, H. S. *Anal. Chem.* **1995**, *67*, 1541-1545.

(42)   Grant, K. M.; Hemmert, J. W.; White, H. S. *Electrochemistry Communications* **1999**, *1*, 319-323.

(43)   Lee, J.; Gao, X.; Hardy, L. D. A.; White, H. S. *J. Electrochem. Soc.* **1995**, *142*, L90-L92.

(44)   Mehta, D.; White, H. S. *Chemphyschem* **2003**, *4*, 212-214.

(45)   Ragsdale, S. R.; Lee, J.; Gao, X.; White, H. S. *Journal of Physical Chemistry* **1996**, *100*, 5913-5922.

(46)   Bousse, L.; Cohen, C.; Nikiforov, T.; Chow, A.; Kopf-Sill, A. R.; Dubrow, R.; Parce, J. W. *Annual Review of Biophysics and Biomolecular Structure* **2000**, *29*, 155-181.

(47)   Aaboubi, O.; Chopart, J. P.; Douglade, J.; Olivier, A.; Gabrielli, C.; Tribollet, B. *Journal of the Electrochemical Society* **1990**, *137*, 1796-1804.

(48)   Ragsdale, S. R.; Lee, J.; White, H. S. *Anal. Chem.* **1997**, *69*, 2070-2076.

(49)   Kabbani, H.; Wang, A. H.; Luo, X. B.; Qian, S. Z. *Physics of Fluids* **2007**, *19*.

(50)   Qian, S.; Bau, H. H. *Physics of Fluids* **2005**, *17*, 067105-067101 - 067105-067112.

(51)   Zhong, J.; Yi, M.; Bau, H. H. *Sensors and Actuators A* **2002**, *96*, 59-66.

(52)   Ikeshoji, T. B. d. N., F. N. J. Electroanal. Chem., 296, 19-36. *J. Electroanal. Chem.* **1990**, *296*, 19-36.

(53)   Weast, R. C., Ed. *CRC Handbook of Chemistry and Physics*, 66th ed.; CRC Press, Inc.: Boca Raton, FL, 1985.

(54)   Munson, B. R.; Young, D. F.; Okiishi, T. H. *Fundamentals of Fluid Mechanics*, 5th ed.; John Wiley & Sons: USA, 2006.

(55)   Nguyen, N.-T.; Wereley, S. T. *Fundamentals and Applications of Microfluidics*, 2nd ed.; Artech House, Inc.: Norwood, MA, 2006.

Chapter 3

Manipulating Fluid Flow on a Chip Through Controlled-Current Redox

Magnetohydrodynamics

Abstract

The use of controlled current at microelectrodes to generate ion flux allows precise and quantitative fluid manipulation on a small scale with redox-magnetohydrodynamics (redox-MHD). The MHD force, $\mathbf{F_B}$, equals the cross product of the ion flux, $\mathbf{j}$, and magnetic flux density, $\mathbf{B}$. Here, a quantitative relationship is experimentally established between these parameters and experimental conditions, namely the fluid velocity, $\mathbf{v}$, and current passing through the electrodes, i, providing a practical means by which to predict and control fluid flow on a small scale with great precision. The data show for our setup that the relationship between $\mathbf{v}$ and i is linear for a fixed $\mathbf{B}$, suggesting that applying current directly to the electrodes, instead of the usual approach of applying a potential, should offer fine tuning of microfluidics and at a level and with simplicity that is not possible with other common micropumping methods. When a potential is applied, the resulting current will fluctuate in time and from one experiment to the next because of less controllable factors: electron transfer kinetics, mass transfer (e.g. changes in convection from MHD itself), concentration (e.g. depletion of redox species) and fouling of the electrode. A comparison is made between fluid flow generated by redox-MHD using applied current and that using applied potential. The data also show that the relationship between $|\mathbf{v}|$ and $|\mathbf{B}|$ is linear. In addition, effects of cell geometries on velocities were investigated. The studies involved microscope visualization to track microbeads to monitor fluid velocity in a small volume of solution containing electroactive potassium ferri- and ferrocyanide at microband arrays in the presence of permanent magnets.

Introduction

Unique from existing studies of magnetohydrodynamics (MHD), this report demonstrates a highly controlled approach for manipulating fluid flow on a small scale by carefully controlling the generation of ions through direct application of a current to an electrode in solution. This kind of fine tuning is critical for the development and design of microfluidic systems The magnetohydrodynamic force ($\mathbf{F_B}$) is equal to the cross product of the ion flux, $\mathbf{j}$, and magnetic flux density, $\mathbf{B}$,

$$\mathbf{F_B} = \mathbf{j} \times \mathbf{B} \tag{1}$$

where $\mathbf{j}$ refers only to the local ion flux which is at a right angle to the B-field there, not the net current, i (C/s), measured between the electrodes. Because there is a non-uniform spatial distribution of ion flux in the system described here, due to the non-symmetric electrode placement relative to the cell walls, it is important to distinguish between the ion flux in solution, $\mathbf{j}$(x,y,z) at a given location and i.

MHD as a microfluidic technique is advantageous for several reasons. First, the composition of the electrically conducting liquid can vary greatly and include both aqueous and non-aqueous solutions. MHD does not require moving parts thereby simplifying device fabrication over mechanical pumping methods, such as centrifugal and syringe pumps [1]. MHD also offers the advantage of bi-directional pumping without the use of valves, which is readily accomplished by changing the polarity of either the magnetic field or the ion flux. Also, its ability to pump in a loop is of interest for chromatographic applications [2]. Addition of electroactive species which undergo faradaic

processes at electrodes (redox-MHD) alleviates problems of electrode degradation and bubble generation due to electrolysis [3-5].

The majority of fundamental studies of MHD fluid flow from the literature have focused on controlling potential [2, 6-17]. Although the potential defines the ratio of oxidized and reduced species at the electrode surface, the resulting current can change over time and between experiments, because it depends on several factors that can vary, such as the kinetics of the electron transfer, mass transfer of species to the electrode surface, uncompensated resistances in the cell, density gradients, electroactive electrode area (which can change with fouling), and redox concentrations [18]. A changing current will cause a change in ion flux and therefore a variation in fluid velocity from MHD.

If current is applied, instead of potential, greater control over MHD fluid velocity can be achieved from short to long times. A drawback is that it is critical for the current to remain below the mass transfer limit to avoid bubble formation or electrode degradation. Because of this, the current and resulting velocities will be lower than those in an applied potential situation.

There are very limited reports in the literature of controlling the current to manipulate MHD-induced convection in solutions. Jang and Lee [12] showed an approximate linear dependence of velocity on current, where the current resulted from applied voltages, but there was a lot of scatter in the plot and the relationship was not quantified. Large voltages from 10 to 60 V were needed because the solution contained only supporting electrolyte; also, bubble generation was a problem. In a study performed by Bau, et al. [19] for an MHD system, it was determined that by maintaining the current at

a fixed value in the presence of a magnetic field, the velocity remained constant over time. This 'controlled current' approach was used for a single current magnitude and a single electrode configuration only, and without added redox species. In the presence of redox species, as is the case in our work, the known electrochemical processes facilitate a systematic study of MHD flow. There is one other report in the literature of operating an MHD pump via applied current. This one involved redox species in the form of a chloroaluminate ionic liquid, but the studies were only qualitative and performed with a single cell geometry on the scale of several millimeters. In addition, no comparisons were made to applied potential [20].

In the work described here, redox-MHD induced convection is generated by application of a current to an electrode in an electroactive solution (containing redox species) to generate a controlled ion flux in the presence of a magnetic field. The induced convection around individually-addressable microband electrodes is visualized using microbeads (as opposed to the polypropylene float used in the chloroaluminate studies) for a known concentration of redox species (potassium ferricyanide and ferrocyanide) to more definitively determine the factors which affect fluid flow as well as obtain quantitative flow profiles, horizontally and vertically, throughout the cell. We have recently used microbeads to observe redox-MHD fluid flow where the potential was controlled, but the studies could only be semi-quantitative because of the many variables that affect the current magnitude during each experiment [5]. The work described herein is unique in that the absolute current at the electrodes can be held constant and thus changes in flow velocities and profiles are due solely to changes in the experimental setup. Thus, drawing quantitative relationships of experiment to theory is possible.

The goal of this work, is to quantitatively study the relationship between the current passing through the electrode, i, the magnetic flux density, **B**, and the resulting MHD-induced fluid velocity in channelless, small-volume systems. To our knowledge, such a relationship has not previously been *experimentally* established and is only now possible with the ability to determine localized velocities by tracking particles, fabricate microelectrode designs and electrochemical cells of known dimensions, and keep constant many factors which influence velocity, such as wall placement relative to the force, and fluid viscosity. (Relationships between current, magnetic flux density, **F_B**, and velocity have only been studied through simulation and theory, and for a symmetric electrode system, only, in which the ion flux is unidirectional [21, 22].) The specific series of studies reported herein parallels those in previous work [5] (the microband arrays, PDMS thicknesses, solution composition, and magnets used here are all the same) where potential was controlled instead of the current, so that comparisons can be drawn between the two approaches for generating and controlling ion flux. The results provide quantitative insight for design of future automated microfluidic devices.

Experimental

Chemicals and materials. All chemicals were of analytical grade and used as received. Aqueous solutions were prepared with reagent grade deionized water from Ricca Chemical Company (Arlington, TX). Potassium ferricyanide ($K_3Fe(CN)_6$) was obtained from EM Science (Gibbstown, NJ) and potassium ferrocyanide trihydrate ($K_4Fe(CN)_6 \cdot 3H2O$) was from J.T. Baker (Phillipsburg, NJ). Potassium chloride was purchased from Aldrich Chemical Co. (St. Louis, MO). Six and ten micron diameter polystyrene latex microspheres, functionalized with surface sulfate groups (2.5 wt%

dispersion in water), were obtained from Alfa Aesar (Ward Hill, MA). Polybead® amino six micron diameter microspheres (2.69% solids-latex in water) were purchased from Polysciences, Inc (Warrington, PA). Polydimethylsiloxane (PDMS) supplies (Sylgard® 184 silicone elastomer base, Sylgard® 184 silicone elastomer curing agent, and OS-30 solvent) were obtained from Dow Corning Corp. Silicon wafers (125 mm diameter and 600-650 μm thickness) with 2 μm of thermally grown SiO_2 were purchased from Silicon Quest International (Santa Clara, California) and were used as the substrate materials for electrode array fabrication. A gold coin (Canadian Maple Leaf, 99.99%) and a chromium-plated tungsten rod (Kurt J. Lesker Company, Clairton, PA) were used for metal deposition onto the silicon wafer for the electrode arrays. Benzocyclobutene, BCB, (Cyclotene 4024-40) was used to insulate the electrode leads and was purchased from Dow Corning Company.

Microelectrode array chips. Each microelectrode array chip is 1 in. × 1 in. and contains 16, individually-addressable Au microband electrodes which are 2 mm in length with equal, nominal widths and gaps of 25, 50, or 100 μm. Each chip also contains four larger Au features, two that are 8 mm × 4.5 mm and often used as counter electrodes and two that are 6 mm × 0.5 mm and often serve as quasi-reference electrodes. Detailed fabrication of the microelectrode array chips is reported elsewhere [5]. Due to the wet metal etching used in fabrication, electrode widths were slightly less than nominal widths above and measured using an optical microscope to be 15, 43, and 92 μm.

Magnetic field. Unless otherwise stated, a NdFeB sintered 1 in. × 1 in. x 0.5 in. magnet (1.23 T residual induction, 0.55 T on the surface) from Magnet Sales Co. was

used. The magnet was positioned directly beneath the array chip, with the magnetic field oriented parallel to the chip normal and directed from the top to the bottom of the chip. The magnetic field was simulated by Amperes 3D Magnetic v. 6.4 (Integrated Engineering Software, Winnipeg, Manitoba, Canada). Figure 3.1a shows streamlines and magnetic field direction. Figure 3.1b illustrates a contour plot of the magnetic field on the x-y surface of the magnet. The variation in $\mathbf{B_z}$ across the x-y plane of the array region (approximated to be 3 mm x 3 mm) is only 0.2% (0.2 T/m). Figure 3.1c shows a contour plot of $\mathbf{B_z}$, zoomed in on the array region, from the top of the microarray chip (the cell floor) to the bottom of the glass microscope slide (the cell lid); the variation of the z-component of the magnetic field for a 650 μm cell height is ~5% (27 T/m). The magnetic flux density was measured to be 0.38T at the top of the array chip above the magnet. For studies of fluid velocity as a function of magnetic flux density, seven NdFeB disc magnets (Ni-Cu-Ni plated and 1 in. diameter × 0.25 in. thick, Amazing Magnets®) were stacked one by one to obtain increasing magnetic flux density, from ~0.27 T for a single magnet (measured on the surface of the chip on top of the magnet) to 0.54 T for all seven magnets. Magnetic flux densities were measured by a DC magnetometer (AlfaLab Inc.).

Experimental set-up. A schematic of the experimental setup is shown in Figure 3.2a. A rectangular opening (14.0 mm x 5.5 mm) was cut into a PDMS film to expose the array region as well as portions of the counter and quasi-reference electrodes and was placed on top of the array chip to form the electrochemical cell (a diagram of the PDMS opening, showing the array, reference, and counter electrodes is shown in Figure 3.2c).
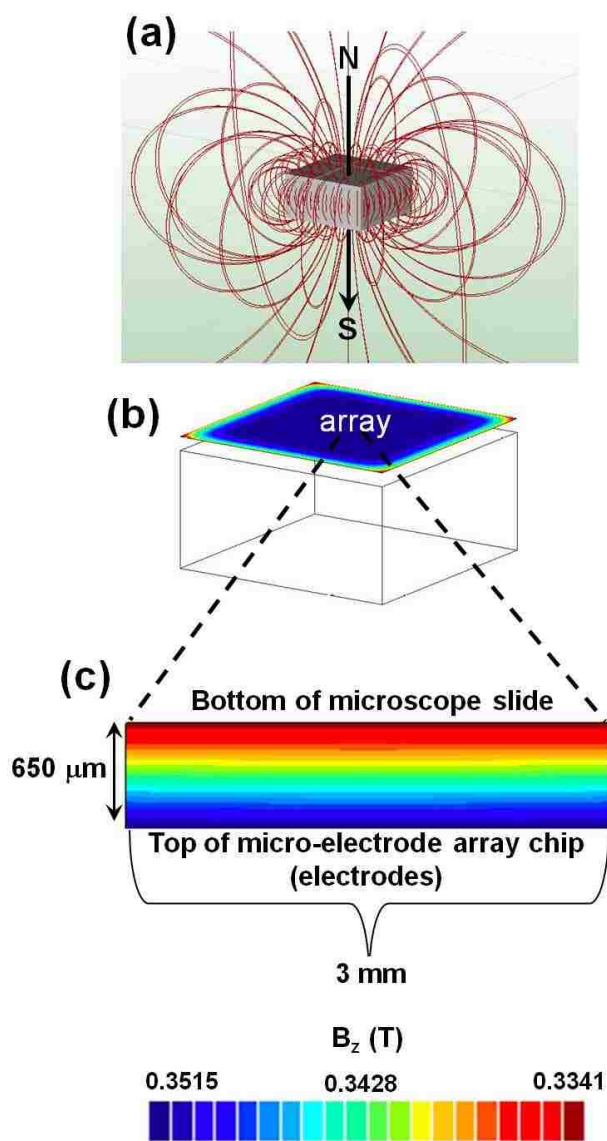
Figure 3.1. (a) Image of a 1 in. x 1 in. NdFeB permanent magnet showing direction of the B-field ($\mathbf{B_z}$) and simulated streamlines. (b) Simulated contour plot of the B-field of the x-y plane of the magnet. (c) Expanded view of the contour plot of the B-field in the array region, across 3 mm, from the bottom of the electrochemical cell to the top of the cell for a PDMS thickness of 650 μm.
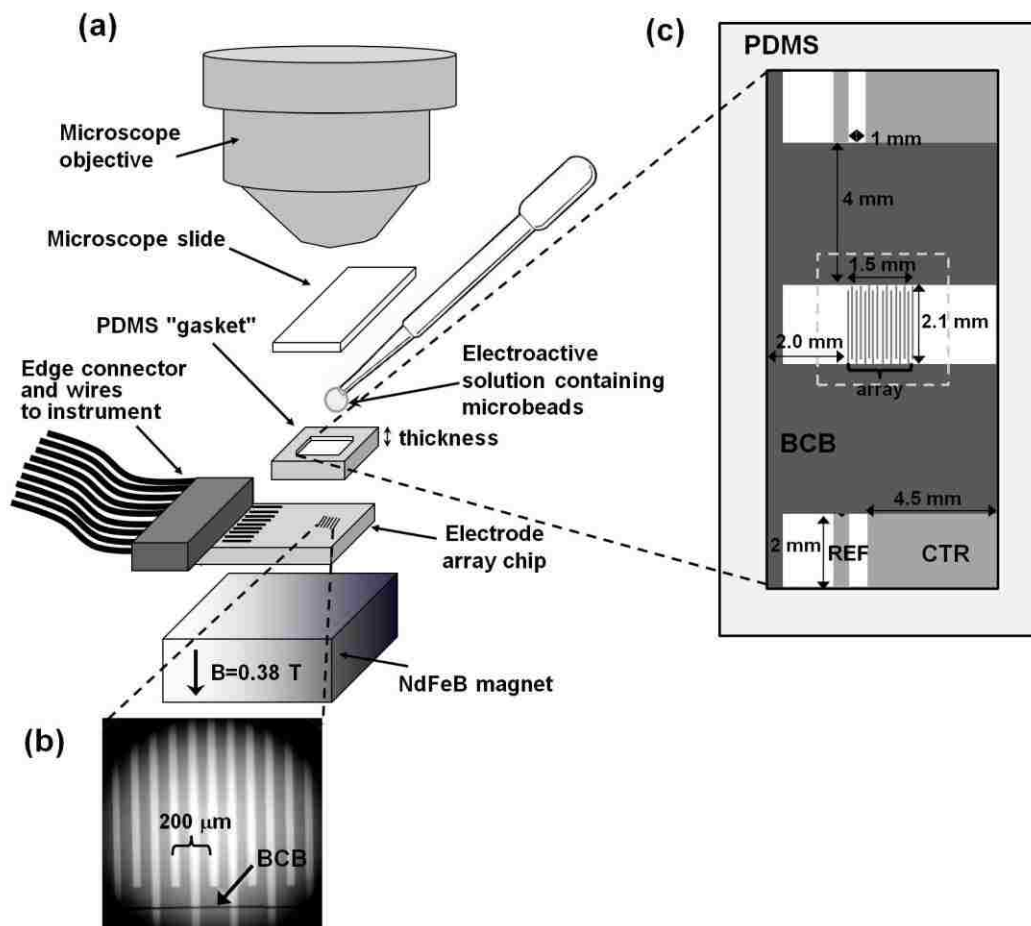
Figure 3.2. (a) Diagram showing assembly of electrochemical cell for viewing the motion of microbeads resulting from magnetoconvective effects at an array of microband electrodes. (b) Optical microscope image of Au array electrodes (11 of 16 bands are shown) with BCB insulator visible to the side of the array region. These microband electrodes were designed with nominal dimensions of 2 mm length, with 50 μm width, having 50 μm gaps between them. (c) Diagram showing a top-down view of the PDMS opening, exposing the array region and parts of the counter and reference electrodes, with dimensions listed. The gray box (dashed-line around array) indicates the approximate region where magnetic field simulation measurements were performed. The variation of $\mathbf{B_z}$ in the x-y plane across that region is only 0.2%.

The cell was then filled with the redox solution containing microbeads. A glass microscope slide was placed on top of the PDMS to serve as the cell lid. The entire apparatus was placed under a Nikon Eclipse ME600 microscope interfaced to a Nikon COOLPIX 990 digital camera to record movies. The microscope was focused into solution to track individual microbeads. Unless otherwise stated, linear bead velocities were measured approximately halfway between the array chip and microscope slide, and in the case of reinforcing flows, halfway between the working and combined auxiliary/quasi-reference electrodes. Average speeds and standard deviations were calculated from speeds of several microbeads determined from the distance they traveled over a given time, using the electrode array as a length scale and the time stamp on the video recording.

Electrochemical control. A CHI 760B bipotentiostat (CH Instruments, Austin, TX) was used for cyclic voltammetry (CV), chronoamperometry (CA), and chronopotentiometry (CP). Anodic currents are reported as negative values throughout. Unless otherwise specified, the solution contained 0.3 M $K_3Fe(CN)_6$, 0.3 M $K_4Fe(CN)_6$, and 0.1 M KCl. The suspension of microbeads were pipetted into the redox solution to achieve a 30X dilution (from 2.5% to 0.083% wt dispersion), and thereby diluted each form of the redox couple to 0.29 M.

Results and Discussion

Electrochemical characterization. Typical electrochemical responses obtained at the microband electrodes are shown in Figure 3.3. The cyclic voltammetry (CV; -0.3 → +0.3 V vs Au; n = 50 mV/s) responses in the absence of a magnet at 15 μm (solid

line), 43- (dotted line) and 92- dashed line) μm electrodes (Figure 3.3a) make a transition from a sigmoidal-shape at the smallest electrode to shapes having increasing peaks for the larger electrodes. This trend is expected and is associated with radial diffusion dominating the mass transfer at the small electrodes and increasing contributions from linear diffusion at the larger electrodes. Chronoamperometry (CA) and chronopotentiometry (CP) were used in MHD experiments where microbead movement was monitored after the potential or current, respectively, was stepped to oxidizing values. Thus, examples of responses at a 43 μm-wide electrode are shown in Figure 3.3b for CA (potential stepped to +0.3 V vs. Au quasi-reference) and CP (current held at -45 μA). All of the electrochemical responses were obtained in a closed cell configuration (650 μm thick PDMS) and in the presence of a magnet ($|\mathbf{B}| = 0.38$ T).

The magnitude of the pseudosteady-state current in a CA experiment was always higher at oxidizing potentials (~ −50 μA when stepped from 0 to +0.3 V at a 43 μm band electrode) than that at reducing potentials (~ +40 μA when stepped from 0 to -0.3 V). The absolute value of the pseudosteady state current for anodic and cathodic excursions is expected to be the same at a microband electrode for a 1:1 mol ratio of a reversible redox couple and is predicted to be 37 μA, as determined from the following equation [23]:

D is the diffusion coefficient (6.5×10^{-6} cm^2 s^{-1} for K$_4$Fe(CN)$_6$ at 25° C) [24], l is the electrode length, C^* is the concentration of redox species, t is the time, and r_o is the electrode radius which may be substituted by the electrode band width / 4. This expected
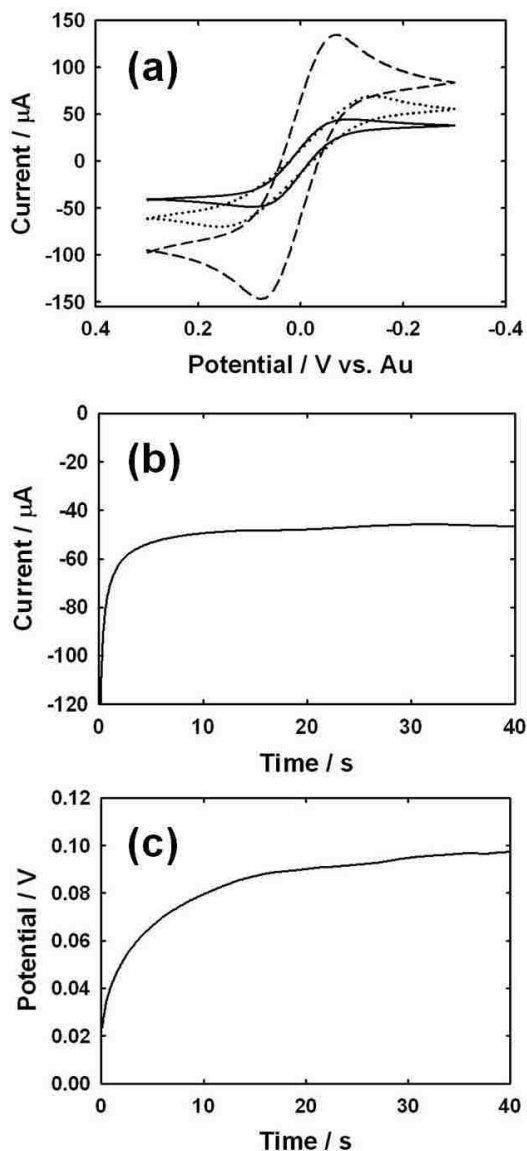
Figure 3.3. (a) Typical electrochemical responses at band electrodes in a solution of 0.3 M $K_4Fe(CN)_6$, 0.3 M $K_3Fe(CN)_6$, and 0.1 M KCl. The on-chip counter and quasi-reference electrodes were used. (a) Cyclic voltammograms collected at 50 mV/s at 15 (solid line), 43 (dotted line), and 88 (dashed line) μm width band electrodes (b) Chronoamperometry performed at a 43 μm band electrode. The potential was stepped from 0 to +0.3 V. (c) Chronopotentiometry performed at a 43 μm band electrode. An anodic current of -45 μA was applied to the electrode. The signals were obtained in a closed cell configuration using 650 μm PDMS and in the presence of a magnet (B=0.38 T).

63

current is closer to the observed cathodic current (within 7% of the expected values) than the observed anodic current (within 25% of the expected value).

One possible reason for the large deviation of the anodic current from theory is that of additional convection caused by density gradients, which cause variation in signal, especially during oxidation of $Fe(CN)_6^{4-}$ at an electrode on the floor of the cell. Volume elements having a composition of lower density (the oxidized form $Fe(CN)_6^{3-}$ and only three associated K^+) rise while the surrounding volume elements that contains $Fe(CN)_6^{4-}$ (and four associated K^+) fall to replace the rising solution. Such fluctuations are noticeable in both CA and CP which are present at the high concentrations of redox species used here. Density gradients have been noted for larger electrochemical systems in which MHD-induced convection has been shown to offset density gradients and is characterized by a decrease in the observed current [25, 26]. The direction of the solution movement caused by these gradients as observed when beads are tracked in the absence of a magnetic field (data not shown) is different than the movement from MHD and is approximately only about 15 μm/s (for a 43 μm band biased to 0.3 V) or ~13% of the magnitude of the MHD velocities (~110 μm/s for the same scenario [5]). Consequently, the net fluid motion in the presence of a magnet as described in more detail below is interpreted as mainly due to the MHD effect. The effect of density gradients on fluid motion is being evaluated further by others in the lab and will be reported on in the future.

Fundamental studies around a single band electrode. Redox-MHD induced convection at a singly biased anode or cathode using the on-chip counter and reference electrodes (labeled in Figure 3.1c) far away from the working electrode will result in

circular flow around the electrode. The flow is generated as a result of the interaction of the magnetic field with the ion flux (which, during oxidation, is directed away from the surface of the electrode and during reduction, toward the electrode surface) to produce a circular MHD force. The MHD force acts on current-carrying species only. Transfer of momentum from these ions to bulk solution gives rise to the flow.

Before performing applied current experiments (CP), the mass transfer limited current was first determined by CA at the electrode(s) when biased to +0.3 V. This current was not exceeded in the applied current experiments to avoid bubble formation and oxidation of the gold electrodes.

Linear bead velocity as a function of applied current was studied. One electrode on the far edge of the array was biased. Beads were measured as they were moving up the side of that electrode away from the other unbiased Au bands, at approximately 300 μm from the biased electrode's center, and 450 μm above the electrode. The bead velocities varied linearly with applied current, from 81 μm/s at −40 μA to 1.6 μm/s at −1 μA. The regression line is $y = 2.05 \ \mu m \ s^{-1} \ \mu A^{-1} \ x - 0.95 \ \mu m \ s^{-1}$, $R^2 = 0.998$. Bead movement was too slow to be measurable when the applied current was smaller than −1 μA. This is the first report, to the authors' knowledge, to quantitatively demonstrate a linear relationship between redox-MHD-induced velocity and current for a given electrode configuration and cell geometry. This has huge implications for future work in redox-MHD microfluidics: as long as current is programmed below the mass transfer limit, velocities can be finely tuned by varying the current without concern over electrode fouling, solution composition, or experiment duration. Thus, additional investigations

with applied current were performed to further elucidate its effect on velocity and to compare with previous applied potential studies as elaborated below.

Electrode size. There is one example in our previously reported applied potential studies where potential was tuned to achieve a constant current (-27 µA) to study fluid flow. That work was performed at band electrodes of three different widths (15 µm, 43 µm, and 92 µm) [5]. This is an interesting example to compare with the case when current is directly held constant. We applied -30 µA in a similar series of experiments but with the PDMS height and location of bead measurements above the electrode being different. Linear bead velocities of 45.5 ± 2.9, 57.5 ± 2.8, and 83.9 ± 4.1 µm/s for those widths were obtained, respectively. In both the applied potential and the applied current studies, the velocity at the 92 µm band was 46% higher than that at the 15 µm band and 32% higher than that at the 43 µm band. This dependence of increasing flow velocity with increasing width is explained by closer opposing flows on each side of narrower electrodes that slow flow because of shear stress.

Using the Auxiliary Electrode for Reinforcing Flow with Applied Potential and Applied Current. Until now, redox-MHD at microband electrode arrays have used an auxiliary electrode that is outside of the array region. In a small volume system, ion flux at the auxiliary electrode and between it and the working electrode(s) can introduce additional fluid motion that needs to be accounted for and can complicate interpretation of the convection in fundamental studies. An electrode configuration in which the auxiliary electrode plays an intentional, active role in the fluid flow solves this problem. An electrode configuration was chosen for further studies in which the auxiliary lead

from the potentiostat made contact to other microband electrodes within the array to produce a reinforcing flow. Reinforcing flows at microband arrays in the past [5] involved the use of a four-electrode experiment using a bipotentiostat to oppositely bias two working electrodes, while separate auxiliary and quasi-reference electrodes were located on the chip but far from the array. The liquid then moves in a path between the two electrodes, as has been shown for MHD in a channel [7, 14, 17, 27]. In addition to simplifying the interpretation of the system by giving the auxiliary electrode an intentional role in the fluid dynamics, only a monopotentiostat is needed to achieve reinforcing flow. One benefit of a reinforcing configuration at the microband electrode array is a faster fluid velocity when compared to circular flow around a singly biased electrode [5]. Another benefit is the fairly uniform fluid velocity between the electrodes, allowing for more reproducible flow measurements than around a single band electrode. In the setup described herein, a single band electrode served as the oxidizing, working electrode, while two band electrodes served as the combined auxiliary and quasi-reference. A schematic representation of the current vectors, magnetic field, and resulting MHD force (and resulting flow) is shown in Figure 3.4a.

It is fitting to start with applied potentials using the simplified electrode configuration for reinforcing flow (presented in this section), because that had been the emphasis previously, and then to expand studies to applied current (presented in the next section). The electrochemical cell consisted of an array containing 43 μm-wide band electrodes and a PDMS thickness of 650 μm. The working and combined auxiliary quasi-reference electrodes were separated by 150 μm (with a single passive electrode between them). Different potentials were applied to the working band electrode and fluid
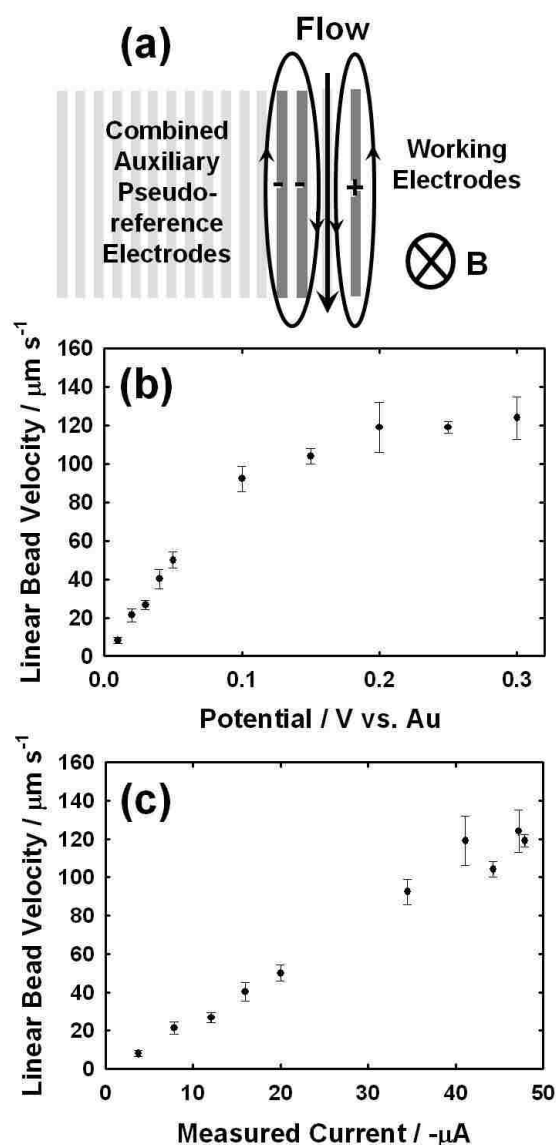
Figure 3.4. (a) Schematic drawing of the flow that results when a single band electrode held at an oxidizing potential or current serves as the working electrode and two other band electrodes serve as the combined auxiliary and quasi-reference electrode. (b) Effect of applied potentials on linear bead velocity. Curve is linear from 0 to 0.10 V (y = 925 (μm s^{-1} V^{-1}) x + 1.21 μm s^{-1}; R^2=0.9943). (c) Bead velocity as a function of measured currents resulting from applied potentials (Figure 3.4a) results in a fairly linear relationship (2.61 (μm s^{-1} μA^{-1}) x + 1.37 μm s^{-1}, R^2=0.982). A PDMS thickness of 650 μm was used. Measurements were made 450 μm above the array. The markers and error bars represent an average velocity and standard deviation, respectively, of five different beads measured in solution over a three second period.

velocities were measured at 450 μm above the array after a steady-state current was

reached (~20 s into the experiment). The effect of linear bead velocity on applied

potential is shown in Figure 3.4b. An ANOVA analysis of the linear bead velocities from

0.3 to 0.2 V concludes that they are the same at the 95% confidence level. Between these

potential values a maximum steady-state mass transfer-limited current was attained, and

therefore a constant MHD force was achieved, thereby resulting in a constant flow rate.

Below 0.2 V, the anodic current and resulting MHD force decreased with decreasing

potentials (in a Nernstian fashion as one nears the $E_{1/2}$ value, which is 0 V), and thus

slower flow rates were observed. This is shown in Figure 3.4c in which the velocity is

plotted as a function of the *measured* current that was produced by the applied potential.

This relationship is linear (y = 2.61 (μm s^{-1} μA^{-1}) x + 1.37 μm s^{-1}, R^2=0.982).

Consequently, the fluid velocity is indeed tunable by directly applying a potential, but it

is an indirect approach with a nonlinear velocity response over a narrow range of

voltages.

Another disadvantage of an applied potential experiment, compared to an applied

current one, is the ability to control $\mathbf{F_B}$ over long times. At the beginning of an

experiment where the electrode potential is stepped to a voltage away from the potential

of zero chage and far negative or far positive of $E_{1/2}$, redox species adjacent to the

electrode and of the appropriate form (oxidized or reduced, respectively) can be

electrochemically converted, resulting in a large *transient* faradaic current. As the starting

species there are depleted, the current magnitude drops and and so does the

corresponding fluid velocity, until a steady-state is reached (if at all). However, when a

current is applied to an electrode and maintained throughout the length of the experiment,
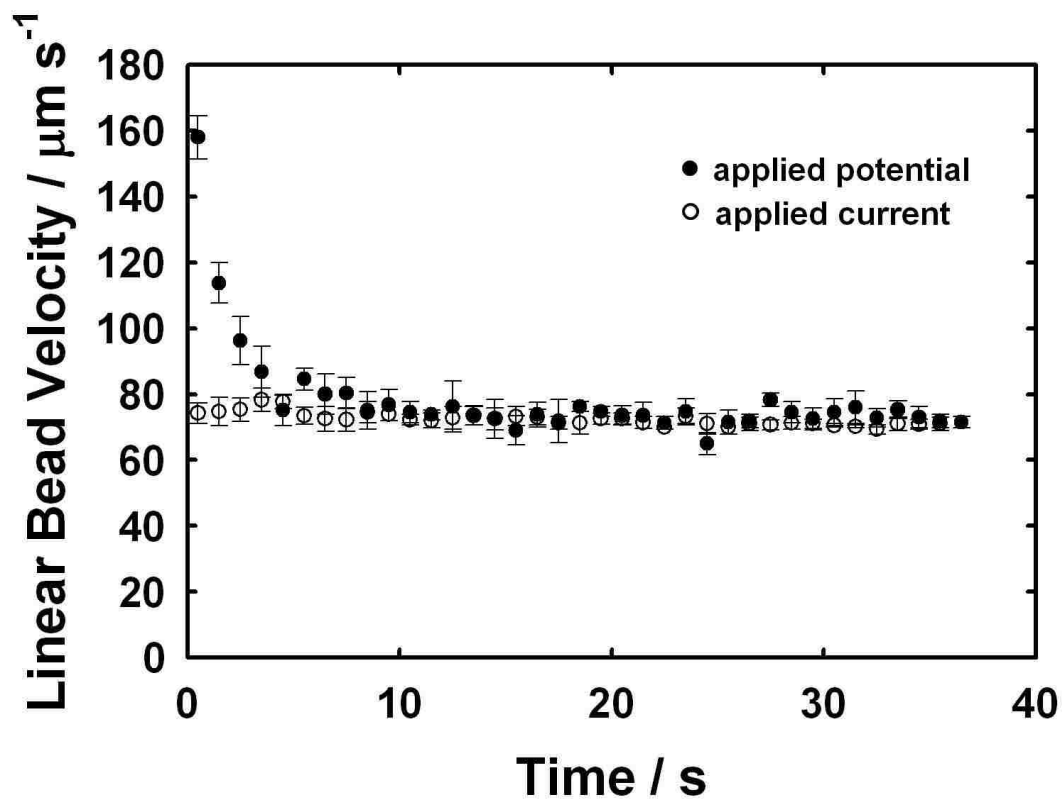
<u>Figure 3.5.</u> A plot of fluid velocity as a function of time for an applied potential experiment (solid circles; a potential of +0.1 V was applied to a 43 μm band) and an applied current experiment (open circles; a current of -30 μA was applied to a 43 μm band). The markers and error bars represent an average velocity and standard deviation, respectively, of four different beads measured in solution over a one second period. A PDMS thickness of 650 μm was used. Bead measurements were made 300 μm above the array.

the resulting velocities should also be constant over the entire time. This is demonstrated in Figure 3.5, in which linear bead velocity is plotted as a function of time for both an applied current experiment and an applied potential experiment. When a potential of +0.1 V is applied to a 43 μm band electrode, the velocity varies from 158 μm/s at 0.5 s to 74.2 μm/s at 36.5 s into the experiment, corresponding to a 53% variation in fluid velocity over this period. When a current of -30 μA is applied to the same electrode, the variation in velocity is only 4% over the same time interval. This could be a very important aspect in microfluidic systems if the delivery of analytes to a certain surface/location is time dependant or if precise pumping rates are required.

Quantifying the relationships among the MHD force, velocity, current, and magnetic flux density. The precise control of applied currents can now be used to explore the relationships between redox-MHD velocity and its experimental parameters more quantitatively than has been reported in the past. A reinforcing flow experiment similar to the one described in the previous section was performed with applied current, instead of applied potential. The linear bead velocity is plotted as a function of the applied current in Figure 3.6a, and produces a highly linear regression line of y = 2.87 (± 0.103) μm s^{-1} μA^{-1} x – 1.07 (± 2.15) μm s^{-1}, R^2 = 0.994. Once again we see that linear bead velocity is directly proportional to current, whether the current was directly controlled (Figure 3.6a) or resulted from a controlled potential (Figure 3.4c). This linearity has now been observed for two separate electrode configurations, although in one single cell geometry. Thus, in order to expand this relationship to other fluidic cells and electrode geometries, further studies are necessary. Consistent with applied potential studies [5], velocity, in the reinforcing flow configuration, is greater (by a factor of ~1.5

71

times) than that for circular flow, and is quantified by a slope of the line in Figure 3.6a

that is nearly 30% greater than that obtained for applied current around a singly biased

electrode (given above).

The effect of magnetic flux density on flow velocities was also investigated with

an applied current approach in reinforcing flow configuration under similar conditions as

above, but by measuring bead velocities in the presence of different magnetic fields at

one constant current of -30 μA. A plot of velocity as a function of magnetic flux density

is shown in Figure 3.6b. Velocities increased with magnetic flux density from 61.6 μm/s

at 0.27 T to 122.3 μm/s at 0.54 T. The regression line emphasizes the strong linearity of

the relationship and is y = 225 ($\pm$ 5.70) μm s^{-1} T^{-1} x + 2.10 ($\pm$ 2.68) μm s^{-1}, R^2 = 0.997. It

is worthwhile to note that there has not been any observed electrophoretic forces acting

on the charged microbeads. Control experiments have revealed that movement in the

absence of the magnetic field is due to density gradient effects (briefly described above)

and not electrophoretic mobility (the direction of movement of the negatively charged

beads in the control experiments is toward the cathode and away from the anode, the

opposite direction as for electrophoresis.), Given the plots in Figure 3.6, the measured

and experimental parameters can now be quantitatively related to the parameters in the

equation governing the MHD force (eq. 1). Essentially, how fluid velocity, |$\mathbf{v}$| relates to

|$\mathbf{F_B}$| and applied current i to |$\mathbf{j}$|, for a given cell geometry, can be demonstrated. The

details are described below. All of the following assumptions only hold true for beads

measured at a single location and time and moving along the y-axis defined in the

direction of the long dimension of the band electrodes, which is the case for both studies
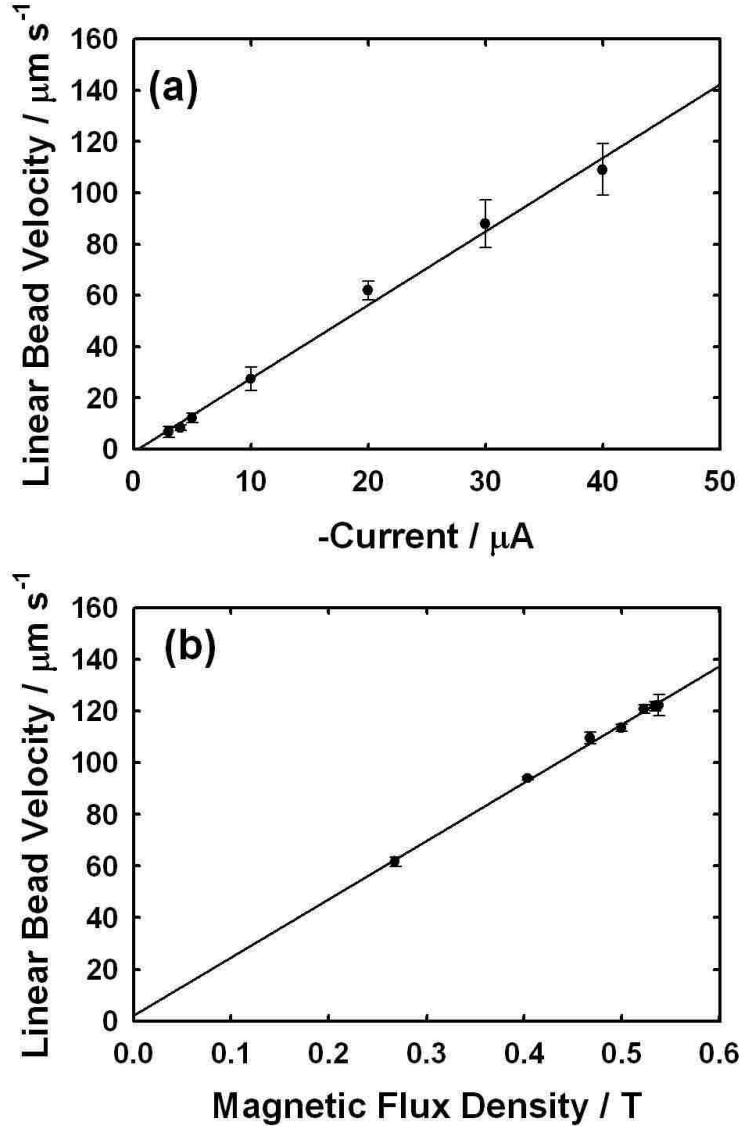
Figure 3.6. (a) Effect of applied current on linear bead velocity. Varying currents were applied to a 43 μm band electrode in the presence of a 0.38 T magnetic flux density. The equation and correlation coefficient of the line are y = 2.87 μm s^{-1} μA^{-1} x − 1.07 μm s^{-1} and 0.994, respectively. (b) Effect of magnetic flux density on fluid velocity. A current of -30 μA was applied to a 43 μm band electrode in the presence of varying magnetic fields. The equation and correlation coefficient of the line are y = 225 μm s^{-1} T^{-1} x + 12.1 μm s^{-1} and R^2=0.997, respectively. Experimental conditions are the same as those listed in Figure 3.4. The markers and error bars represent an average velocity and standard deviation, respectively, of five different beads measured in solution over a three second period.

in Figure 3.6. Thus, vector functions have been removed from the following discussion and the variables are defined as scalars in the x, y, and z directions.

If we assume that F_{By} is proportional to fluid velocity in that direction (v_y), through a pressure and viscosity factor (γ) from the Navier-Stokes equation for incompressible flow of a Newtonian fluid [28], then we get the relationship in eq. 2,

$$F_{By} = \gamma v_y \tag{2}$$

where γ is a constant relating F_{By} to velocity.

If we further assume that the ion flux, j_x, is related to the applied current (i) through a geometric and mass transfer factor (k) from the Nernst-Planck equation [18], then we can write eq. 3,

$$j_x = ki \tag{3}$$

where k is a constant relating ion flux, in a direction perpendicular to the B-field only, to the applied current, passing through the electrodes.

Substituting eq. 2 and eq. 3 into eq. 1 and rearranging terms yields an expression (eq. 4) for measured velocity as a function of known experimental parameters, the applied current and magnetic field, as well as the fluid properties and cell geometry,

$$v_y = \frac{k}{\gamma} i B_z \tag{4}$$

By using the slopes from the regression lines for velocity as a function of applied current (Figure 3.6a, where $|B| = 0.38$ T) and velocity as a function of magnetic flux density (Figure 3.6b, where i = -30 μA), it is possible to solve for the constant, k/γ, which should be the same for both cases. The slope in Figure 3.6a was 2.87 ± 0.10 μm s^{-1} μA^{-1}

and yields a k/γ value of 7.54 (± 0.27) μm s^{-1} T^{-1} μA^{-1}, and that in Figure 3.6b was 225 ±

5.7 μm s^{-1} T^{-1}, yielding a value of 7.52 (± 0.19) μm s^{-1} T^{-1} μA^{-1} for k/γ. The constants

from the plots are the same at the 95% confidence level. Therefore, the assumptions hold

true: velocity is directly proportional to **F$_B$**, applied current is directly related to the ion

flux, and velocity can be obtained from the product of the applied current and magnetic

flux density, knowing the proportionality constant, k/γ.

To determine whether the exponents of i and B$_z$ in eq. 4 are indeed unity (when n

= 1 and m = 1 as in eq. 5), regression lines to the plots of log(v$_y$) vs log(i) and of log(v$_y$)

vs log(B$_z$) were obtained (not shown).

$$v_y \quad \blacksquare \quad B_z^m \tag{5}$$

The exponents *n* and *m* in eq. 5, determined from the slopes of the log-log plots, were 1.1

± 0.03 and 0.99 ± 0.02, respectively. These values are close to unity, indicating that *i* and

B$_z$ contribute approximately equally to fluid flow v$_y$, and therefore to F$_{By}$.

Cell height. The effect of electrochemical cell height on redox-MHD generated

fluid velocity in small volume cells has not been reported previously. Because of the

ability to control current and monitor fluid flow with the microbeads, we can now

investigate the effects of the proximity of the no-slip boundaries from the lid and floor,

and of the force-generating electrodes on fluid flow. It would be more difficult to

interpret results of cell height studies using applied potential, because the current can

vary greatly depending on the time scale of the experiment and the relative cell height-to-

electrode width ratio, resulting in competing processes of radial diffusion, linear

diffusion, and "thin-cell" depletion of redox species in the small volume as has been

discussed previously [29]. The reinforcing electrode configuration was used like that already described above, but in which a constant current of -40 µA was applied and the PDMS thickness that defines the cell height was varied from 75 to 2600 µm.

Flow velocity measurements were made at two different locations for each cell height: halfway between the array chip and lid, and at a constant height of 150 µm above the array. Particle velocities as a function of PDMS thickness for each of the two different measurements are shown in Figures 3.7a and 3.7b, respectively. When measurements were made at a constant height above the array chip it was observed that velocities increased with increasing cell height up to 650 µm and then leveled off at heights greater than that. In this system, there is a zero-velocity no-slip boundary condition at both, the floor of the cell (at the electrode surface) and at the lid. As the cell height is increased, the no-slip condition at the lid moves farther away from the single distance (150 µm above the chip) where beads are measured, and thus velocities increase until the lid has moved far enough away (> 650 µm) such that it has a negligible effect on flow rates, thereby causing velocities to level off.

When measurements were made halfway between the array chip and cell lid, the velocities increased with cell height up to 500 µm and then began to decrease as PDMS thicknesses increased further. There are several phenomena associated with fluid convection in this cell. The first of which involves the location of the walls that affects the fundamental fluid dynamics of the cell. This plays an important role when a very thin PDMS gasket is used and the glass lid and array chip are very close together (bringing the two, zero-velocity no slip boundary conditions together). This in turn causes resistance to
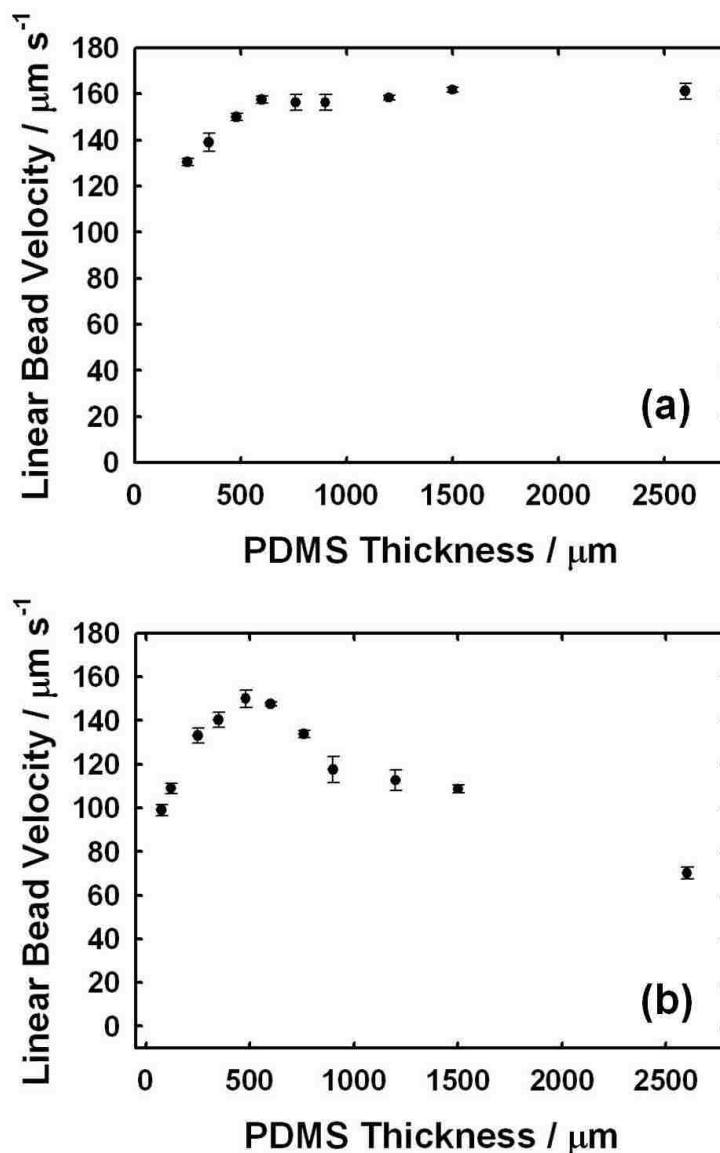
<u>Figure 3.7.</u> (a) Effect of PDMS thickness on linear fluid velocity. A constant current of -40 μA was applied to a singly biased 43 μm electrode. A combined auxiliary and quasi-reference was placed 150 μm from the biased working electrode. (a) Linear fluid velocity plotted as a function of PDMS thickness for measurements made 150 μm above the array. (b) Linear fluid velocity plotted as a function of PDMS thickness for measurements made halfway between the array and the glass microscope slide. The markers and error bars represent an average velocity and standard deviation, respectively, of three different beads measured in solution over a three second period.

flow and results in the 10 μm particles moving much slower in the confined space (hence the reason for slower velocities at the small cell heights). Two other parameters to consider are the magnetic field gradient and the spatial distribution of the ion flux. In the thicker (deeper) cells, when the measurements are made halfway between the chip and the lid, beads are tracked much farther away from both the magnet and the electrodes. Because both B and j decrease with increasing distance from where they are generated, the resulting MHD force is expected to be lower and thus fluid velocities will decrease. These height studies are important in design considerations of the shape and size of a cell or channel in a redox-MHD microfluidic system. One way to better quantify the spatial distribution of $\mathbf{F_B}$ is to obtain velocity profiles as is described in the next section.

Flow profiles. Velocity profiles were determined in two directions for a reinforcing flow configuration and while controlling the current at a fixed value. Three 50 μm band electrodes with 50 μm gaps were held at 100 μA, 650 μm away from the four 50 μm band electrodes serving as the counter electrode (Figure 3.8a). This electrode configuration generated much higher velocities, as a result of the increased electrode area (and thus, the ability to apply greater currents). Also, the larger gap (650 μm gap as opposed to the 150 μm gap which was used throughout) made it possible to acquire more velocity measurements between oppositely biased sets of electrodes. One profile was horizontal, between the oppositely polarized electrodes at a height of 300 μm above the array, centered vertically between the array chip and the lid. The other was vertical across the height of the electrochemical cell from the array chip to the lid and centered horizontally between the electrodes. Microbead speeds were measured at 100 μm intervals.

The horizontal flow profile is shown in Figure 3.8b, where linear bead velocity is plotted as a function of distance from the working electrode (defined as 0 μm). What is startling and consistent with previous results [5] is the relatively flat flow profile between the pumping electrodes. Flat profiles are of interest in separations of mixtures. Therefore, redox-MHD microfluidics may offer benefits to that field. This uniform flow between pumping electrodes also suggests that if an array of immobilization or detection sites, for analytical applications, lay between the pumping electrodes, they will have similar exposure rates to the solution, allowing for similar incubation times and detection signals. A schematic illustrating where bead speeds were measured for vertical profile studies were made and the corresponding plot of linear bead velocity as a function of height above the array chip are shown in Figures 3.8c and 3.8d, respectively. The measurements were achieved by raising the focus of the microscope in 100 μm increments and determining the velocity of the microbeads that were in focus at each interval. The array chip was defined as height = 0 μm and the glass microscope slide as height = 650 μm. More beads are found near the top of the cell as they are less dense than the surrounding redox solution. The linear flow rate is at a maximum at a height of ~200 μm above the array chip and drops off steeply toward the lid. When the beads are very close to either the chip or the lid (i.e. the no-slip boundaries), they should be slowed due to drag, which we attribute as the reason why the fastest flow rate is not observed closest to the array. Flow velocities will be faster near the array as the MHD force is strongest there. This is because the largest ion flux resides at the electrodes. Further from the array, the MHD force is not as strong and velocities are slower. This decrease in F_B is due to a combination of the decrease in ion flux further from the electrodes as well as a decrease
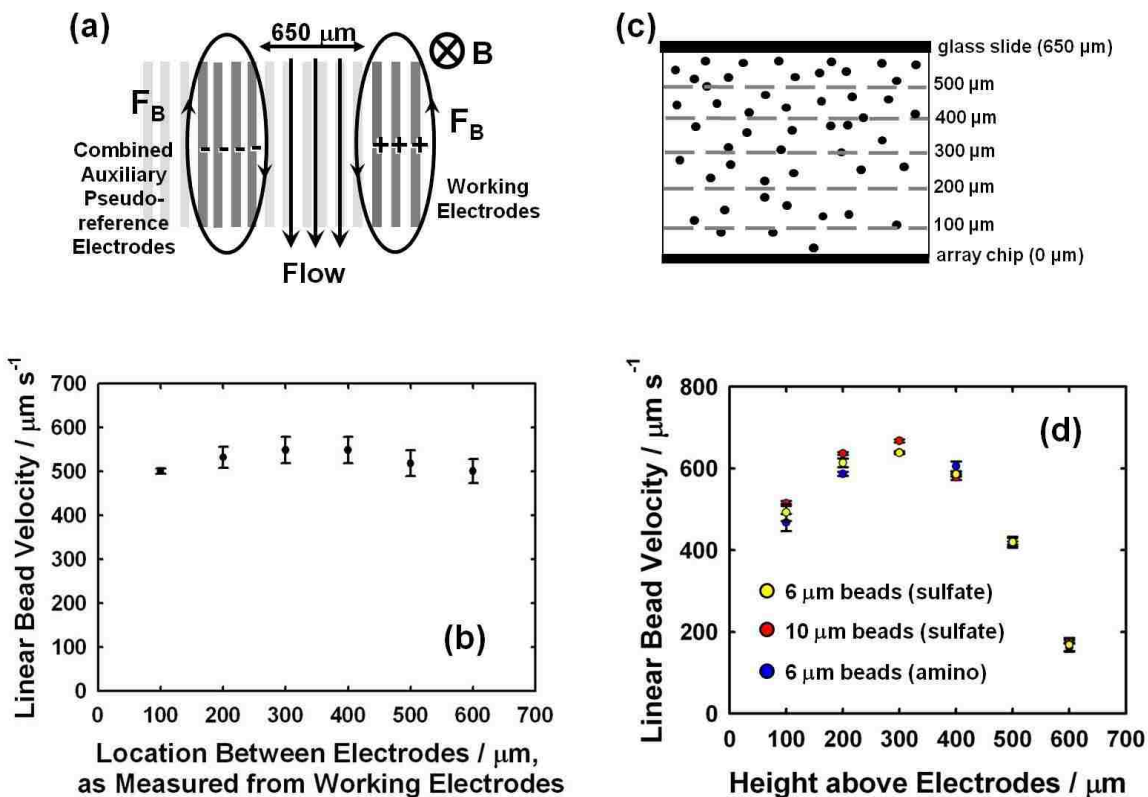
Figure 3.8. (a) . Flow profiles between two oppositely biased electrodes. (a) Schematic drawing of flow between three-43 μm band electrodes (serving as working electrodes) and four-43 μm band electrodes (serving as combined auxiliary and quasi-reference electrodes) separated by a 650 μm gap. The reducing electrodes are defined as 0 μm, and the oxidizing electrodes (held at an anodic current of -100 μA) are defined as 650 μm. (b) Fluid velocity is plotted as a function of location between the two electrodes. (c) Schematic drawing of cross-section of solution with microbeads above the array chip, showing where the velocities were measured to create the plot in (d). (d) Fluid velocity obtained midway between the working and combined auxiliary and quasi-reference electrodes, at ~325 μm, as a function of height above the array chip. The solution consisted of either 6 μm negatively charged beads (yellow), 6 μm positively charged beads (blue) or 10 μm negatively charged beads (red) in 0.3 M $K_4Fe(CN)_6$, 0.3 M $K_3Fe(CN)_6$, and 0.1 M KCl. A magnetic field of 0.38 T and PDMS thickness of 650 μm were used.

in magnetic flux density further from the permanent magnet. Three different types of beads were used in this experiment: 10 and 6 μm polystyrene beads stabilized with a slight anionic charge from surface sulfate groups and 6 μm poly-amino beads, which are expected to be positively charged at the pH of the solution (pH = 7.5). An ANOVA analysis determined that there is no significant difference in the magnitude of the linear velocity for the 6 μm beads of varying functional groups for a given location in the cell at the 95% confidence level. However, the 10 μm beads have slightly higher velocities in the region close to the array but are the same as the 6 μm beads at the 95% confidence level at distances further from the array (500 and 600 μm above the array). The reason for this is unknown at this time. However, the overall flow profile is similar for all three types of beads, indicating that there is no direct MHD force on the beads. Rather, their movement results primarily from the force and resulting fluid flow initiated by the oxidation and reduction of the redox species.

Conclusions

We have demonstrated that applying a current in a small-scale redox-MHD system to generate convection attains the same outcomes as applying a potential but is much easier to control. We have also simplified the electrode configuration by incorporating the auxiliary electrode into the array to produce reinforcing flow instead of having a distant auxiliary electrode. This design is unique in that a channel-like flow is produced without requiring integration of channel sidewalls into a device. Interpretation of results is also simplified due to the fairly flat profile that is obtained in the reinforcing flow configuration. These tools can allow exploration of the fundamentals of redox-MHD

on a small scale more quantitatively. We have already demonstrated this by establishing

linear relationships between velocity and current (i) and velocity and |**B**| which coincide

with the theoretical linearity of $\mathbf{F_B}$ with **j** and **B**. This indicates that velocities attained in

redox-MHD microfluidic systems can be finely tuned by simple adjustments of i or **B**.

We anticipate that the application of current, instead of potential, to obtain ion flux is

likely to lead to better implementation and reproducibility in future applications of redox-

MHD.

References

(1)   Pamme, N. *Lab on a Chip* 2006, *6*, 24-38.

(2)   Eijkel, J. C. T.; Dalton, C.; Hayden, C. J.; Burt, J. P. H.; Manz, A. *Sensors and Actuators B* 2003, *92*, 215-221.

(3)   Qian, S. Z.; Bau, H. H. *Mechanics Research Communications* 2009, *36*, 10-21.

(4)   Weston, M. C.; Gerner, M. D.; Fritsch, I. *Analytical Chemistry* 2010, *82*, 3411-3418.

(5)   Anderson, E. C.; Weston, M. C.; Fritsch, I. *Analytical Chemistry* 2010, *82*, 2643-2651.

(6)   Aguilar, Z. P.; Arumugam, P. U.; Fritsch, I. *Journal of Electroanalytical Chemistry* 2006, *591*, 201-209.

(7)   Arumugam, P. U.; Fakunle, E. S.; Anderson, E. C.; Evans, S. R.; King, K. G.; Aguilar, Z. P.; Carter, C. S.; Fritsch, I. *J. Electrochem. Soc.* 2006, *153*, E185-E194.

(8)   Bau, H. H.; Zhong, J. H.; Yi, M. Q. *Sensors and Actuators B-Chemical* 2001, *79*, 207-215.

(9)   Grant, K. M.; Hemmert, J. W.; White, H. S. *J. Am. Chem. Soc.* 2002, *124*, 462-467.

(10)   Homsy, A.; Koster, S.; Eijkel, J. C. T.; van den Berg, A.; Lucklum, F.; Verpoorte, E.; de Rooij, N. F. *Lab Chip* 2005, *5*, 466-471.

(11)   Homsy, A.; Linder, V.; Lucklum, F.; de Rooij, N. F. *Sensors and Actuators B-Chemical* 2007, *123*, 636-646.

(12)   Jang, J.; Lee, S. S. *Sensors and Actuators A* 2000, *80*, 84-89.

(13)   Nguyen, B.; Kassegne, S. K. *Microfluidics and Nanofluidics* 2008, *5*, 383-393.

(14)   Qian, S.; Bau, H. H. *Sensors and Actuators B-Chemical* 2005, *106*, 859-870.

(15)   Wang, L. S.; Flanagan, L.; Lee, A. P. *Journal of Microelectromechanical Systems* 2007, *16*, 454-461.

(16)   West, J.; Karamata, B.; Lillis, B.; Gleeson, J. P.; Alderman, J.; Collins, J. K.; Lane, W.; Mathewson, A.; Berney, H. *Lab Chip* 2002, *2*, 224-230.

(17)   Zhong, J. H.; Yi, M. Q.; Bau, H. H. *Sensors and Actuators a-Physical* 2002, *96*, 59-66.

(18)   Bard, A. J.; Faulkner, L. R. *Electrochemical Methods: Fundamentals and Applications*, 2nd ed.; John Wiley & Sons, Inc.: New York, 2001.

(19)   Bau, H. H.; Zhu, J. Z.; Qian, S. Z.; Xiang, Y. *Sensors and Actuators B-Chemical* 2003, *88*, 205-216.

(20)   Wilkes, J. S.; Williams, M. L.; Musselman, R. L. *Electrochemistry* 2005, *73*, 742-744.

(21)   Aogaki, R.; Fueki, K.; Mukaibo, T. *Denki Kagaku* 1976, *44*, 89-94.

(22)   Boum, G. B. N.; Alemany, A. *Electrochimica Acta* 1999, *44*, 1749-1760.

(23)   Nagale, M. P.; Fritsch, I. *Analytical Chemistry* 1998, *70*, 2902-2907.

(24)   Stackelberg, M. v.; Pilgram, M.; Toome, V. *Zeitschrift für Elektrochemie* 1953, *57*, 342-350.

(25)   Gao, X.; Lee, J.; White, H. S. *Anal. Chem.* 1995, *67*, 1541-1545.

(26)   Leventis, N.; Gao, X. *Journal of the American Chemical Society* 2002, *124*, 1079-1086.

(27)   Anderson, E. C.; Fritsch, I. *Anal. Chem.* 2006, *78*, 3745-3751.

(28)   Davidson, P. A. *An Introduction to Magnetohydrodynamics* Cambridge University Press: New York, 2001.

(29)   Lewis, P. M.; Sheridan, L. B.; Gawley, R. E.; Fritsch, I. *Analytical Chemistry*, *82*, 1659-1668.

Chapter 4

Redox-Magnetohydrodynamic Microfluidics Without Channels and

Compatible with Electrochemical Detection Under Immunoassay Conditions

The following chapter was published in a very similar form as:

Melissa C. Weston, Christena K. Nash, and Ingrid Fritsch, "Redox-Magnetohydrodynamic Microfluidics Without Channels and Compatible with Electrochemical Detection Under Immunoassay Conditions." *Anal. Chem.* **2010**, *82*, 7068-7072.

Abstract

A unique capability of redox-magnetohydrodynamics (redox-MHD) for handling liquids on a small scale was demonstrated. A 1.2 µL solution plug was pumped from an injection site to a detector without the need for a channel to direct the flow. The redox pumping species did not interfere with enzymatic activity in a solution compatible with enzyme-linked immunoassays. Alkaline phosphatase (AP), a common enzyme label, converted p-aminophenyl phosphate (PAPP) to p-aminophenol (PAP_R) in the presence of 2.5 mM $Ru(NH_3)_6Cl_2$ and 2.5 mM $Ru(NH_3)_6$ Cl_3, in 0.1 M Tris buffer (pH = 9). A solution plug containing PAPP (no AP) was pumped through the surrounding solution containing AP (no PAPP), and the enzymatically generated PAP_R was easily detected and distinguishable electrochemically from the pumping species with square wave voltammetry down to 0.1 mM concentrations. The test device consisted of a silicon chip containing individually-addressable microband electrodes, placed on a 0.5 T NdFeB permanent magnet with the field oriented perpendicular to the chip. A 8.0 mm wide $\times$ 15.5 mm long $\times$ 1.5 mm high volume of solution was contained by a poly(dimethylsiloxane) gasket and capped with a glass slide. A steady-state fluid velocity of ~30 µm/s was generated in a reinforcing flow configuration between oppositely polarized sets of pumping electrodes with ~2.1 µA.

Introduction

There is great interest in developing lab-on-a-chip devices that provide advantages over traditional laboratory analysis including low sample consumption and waste generation, faster analysis times, low fabrication costs, and portability.[1] These systems can be employed in applications such as environmental monitoring, separations, and biodetection. The most common microfluidic technique presently of interest for development of these devices is electrokinetic pumping. Electrokinetic pumping, however, requires high voltages (~100 V) that cause bubble formation from electrolysis of water[2, 3] and is highly dependent on the physicochemical properties of the walls, and thus, flow rates change with solution composition and over time.[4] Redox magnetohydrodynamics (redox-MHD) is an alternative approach to microfluidics and offers advantages such as low voltages, easy bidirectional pumping, simplicity of fabrication (in part, due to the variety of substrates suitable for device fabrication which do not affect redox-MHD pumping), and compatibility with and wettability by a variety of different solvents. [5-8] The only compositional requirement for device materials that is unique to redox-MHD pumping involves providing ion flux, which in our case is accomplished by the presence of electrodes.

In redox-MHD, the oxidation or reduction of an added electroactive species generates an ion flux, $\mathbf{j}$ (coulomb/(second square meter)), in the presence of a magnetic field, $\mathbf{B}$ (tesla), to produce a magnetohydrodynamic force, $\mathbf{F_B}$ (newton/cubic meter), whose magnitude and direction are governed by the cross product relationship, $\mathbf{F_B} = \mathbf{j} \times \mathbf{B}$, following the right-hand rule. Redox-MHD offers a significant improvement

over traditional MHD where large voltages are applied at electrodes in solutions containing supporting electrolyte alone to achieve desired fluid flow.[9-15] However, in redox-MHD, the ion flux is controlled with redox chemistry that can be turned on and off at electrodes at strategic locations at low voltages (<1 V) and, thus, avoids bubble generation and electrode degradation. A shortcoming of redox-MHD that has been reported previously[6, 8, 16] is the need for a high concentration (100s of mM) of redox species to provide a large enough current (and ion flux) so that a sufficient MHD force can be generated with the low magnetic fields of permanent magnets that are suitable for hand-held devices. High concentrations of redox molecules could cause interferences in detection methods through chemical or electron transfer reactions with the analyte of interest.

We have previously demonstrated redox-MHD for the enhancement of anodic stripping voltammetry.[16-18] In those studies, the same electrode was used for both convective and detection functions. It is also an example of how MHD can "grab" a fluid element and move it without requiring channel sidewalls for guidance. However, the high concentration of redox species used for convection in the deposition step needs to be rinsed away before the detection (stripping) step to avoid a high background signal. Also, millimeter-sized electrodes were needed to achieve a large enough j and, therefore, large F_B to cause sufficient flow to increase analyte delivery to the electrode surface and significantly enhance the signal 2- to 3-fold. To use redox-MHD to enhance convection at microelectrodes in low B fields, as might be of interest in a microfluidic device, it would be more efficient to separate the pumping (or stirring) function (taking place at larger electrodes, 100s μm to several mm) from the detecting function (taking place at smaller

electrodes, ≤ 100 µm). This would offer the advantage of a flow-through system, capable of introducing sample and rinsing solutions across a surface in an automated fashion. In addition, we have recently determined that it is possible to observe MHD convection in low concentrations of redox species (10 mM)[19] indicating that rinsing away the pumping species might not be necessary. Given these new developments, the goal of the work herein is to ascertain the suitability of redox-MHD microfluidics under conditions that are directly relevant to a lab-on-a-chip application, specifically enzyme-linked immunoassays with electrochemical detection.

Heterogeneous immunoassays have high specificity and have been built on multiple substrates including glass, silicon, polymers, and gold, all of which can be readily integrated into microfluidic systems.[20-23] Immunoassays are often limited by mass transfer, driven by diffusion, rather than binding kinetics to capture antigens and secondary antibodies and to generate detectable enzymatic products. This results in longer incubation times because of the small diffusion coefficients associated with large biological species. [24] Stirring, therefore, helps to increase the flux of the antigen and further decrease incubation times. Because of MHD's unique abilities to direct, mix, and position fluids, all on a single device, redox-MHD-induced convection could serve as a method to introduce and replace solutions containing immunoassay components and wash buffers in addition to mixing these components on-chip to decrease incubation times.

In the work described here, we focus on the use of redox-MHD induced convection as an effective way to transport components of an immunoassay while detecting an electrochemically active species, simultaneously. The redox-MHD-induced

convection is achieved by application of a low voltage (-0.25 V vs Au quasi-reference) to a set of electrodes in a solution containing the pumping redox couple of $Ru(NH_3)_6^{2+/3+}$ at low concentrations in Tris buffer in the presence of a magnetic field (from a small, NdFeB permanent magnet). p-Aminophenol (PAP_R), which is the product of the reaction of p-aminophenylphosphate (PAPP) with the enzyme alkaline phosphatase (AP) commonly used in electrochemically based, heterogeneous enzyme-linked immunoassays,[25, 26] is directed by redox-MHD flow, with pumping electrodes, to a separate detecting electrode where square wave voltammetry (SWV) is performed for detection of PAP_R in the presence of the pumping species. The Tris buffer allows AP to exhibit excellent enzyme efficiency and PAPP to show good stability.[27]

Experimental

Chemicals and materials. All chemicals were reagent grade and used as received. Aqueous solutions were prepared with high purity deionized water from Ricca Chemical Co. (Arlington, TX). AP from bovine intestinal mucosa in lyophilized powder form, p-aminophenol hydrochloride, palladium (10 wt % on activated carbon), magnesium chloride hexahydrate, and 0.02% (w/v) sodium azide were obtained from Sigma (St. Louis, MO). Polystyrene latex microspheres (10 μm diameter, 2.5 wt % dispersion in water), 4-nitrophenyl phosphate disodium salt hexahydrate, and ruthenium(II) hexaammine chloride were obtained from Alfa Aesar (Ward Hill, MA). The as-received ruthenium(II) hexaammine chloride contained the oxidized form, ruthenium(III) hexaammine chloride, as well. Solutions prepared from this solid were composed of approximately a 1:1 mol ratio of the two forms, as determined by cyclic voltammetry at a microband electrode. Tris(hydoxymethyl)aminomethane was acquired

from J. T. Baker. Pieces cut from a gold coin (Canadian Maple Leaf, 99.99%) placed in a molybdenum boat (Kurt J. Lesker Co., Pittsburgh, PA) and a chromium-plated tungsten rod (Kurt J. Lesker Company, Clairton, PA) served as Au and Cr sources for metal deposition, respectively. Silicon wafers (125 mm diameter, 600-650 μm thickness, and (100) orientation) with 2 μm, thermally grown SiO_2, purchased from Silicon Quest International, were used as substrates for microband array fabrication. Benzocyclobutene, BCB (Cyclotene 4024-40) was obtained from Dow Chemical Company. Electrical connection of the potentiostat to on-chip contact pads was made using an edge connector (solder contact, 20/40 position, 0.05 in. pitch) from Sullins Electronics Corp. (San Marcos, CA). Ultra high purity compressed argon gas was obtained from AirGas, Inc. (Radnor, PA).

PAPP synthesis. The *p*-aminophenyl phosphate (PAPP) was synthesized in-house as previously described.[28] 4-Nitrophenyl phosphate disodium salt hexahydrate (210 mg, 0.57 mmol), obtained from Alfa Aesar (Ward Hill, MA), and palladium/carbon catalyst (64 mg), from Sigma (St. Louis, MO, were dissolved in 30 mL of deionized water and the pH was adjusted to 6.5 by addition of 6 M HCl (Fisher Scientific, Pittsburgh, PA). The solution was placed under 1 atm H_2 to allow reduction to proceed at room temperature for 2 h. The catalyst was removed by filtration. The clear filtrate was lyophilized under high vacuum (< 0.5 mm Hg). The product was characterized by ^{1}H NMR (Bruker 300 MHz, D_2O, δ): 6.51 (2H, doublet, J = 8.4 Hz), 6.70 (2H, doublet, J = 8.4 Hz).

Buffer solution. The 0.1 M Tris buffer solution was prepared with 0.10 M tris(hydroxymethyl)aminomethane, 1 mM magnesium chloride, and 0.02% (w/v) sodium

azide at pH 9.0 (adjusted with 6 M HCl or 6 M NaOH). All solutions used were made from 0.1 M Tris buffer (pH 9.0) that was purged for at least 20 min before use, and all solutions were kept under Ar between runs to minimize oxidation of $Ru(NH_3)_6{}^{2+}$ and PAP_R.

Microelectrode array chips. Detailed fabrication and characterization of microelectrode array chips is described elsewhere.[19] The 1 in. × 1 in. chips contained 16 individually addressable Au microband electrodes (each was 2 mm long and 92 μm wide, and separated from adjacent bands by 107 μm gaps). A single electrode in the middle of the array, electrochemically oxidized (after masking off part with tape) to shorten it to be 1 mm long, served as the detecting electrode. Each chip also contained two on-chip Au quasi-reference electrodes (6 mm x 0.5 mm).

Electrochemical control. A CHI 760B bipotentiostat (CH Instruments, Austin, TX) was used for chronoamperometry (CA) and square wave voltammetry in a three-electrode configuration. The detecting electrode was connected to working lead "one" from the bipotentiostat. Five microbands that were shorted together to form one set of pumping electrodes were attached to working lead "two". Six shorted microbands on the other side of the detecting electrode and 1100 μm away from the first set of pumping electrodes formed the second set of pumping electrodes at an opposite bias and were connected to the auxiliary lead. The distant on-chip quasi-reference electrodes were shorted together (2.0 mm^2 total active area).

Experimental setup. The general experimental setup (see Figure 4.1a) and visualization of redox-MHD flow using microbeads were reported previously.[19] A

poly(dimethylsiloxane), or PDMS, gasket (1500 μm thick with a rectangular cutout of 8.0

mm × 15.5 mm) was placed on top of the array chip and defined the height of the cell.

The walls lining the cutout of the PDMS gasket were far enough from the pumping

electrodes such that they did not define a "channel" but rather served to contain the

solution. Thus, lateral movement of the solution plug was guided by the MHD force,

instead of channel sidewalls. Two, 1 mm diameter holes were drilled through a glass

microscope slide (25.0 mm x 12.0 mm) to form "ports" and allowed for solution

introduction and removal. The glass slide was then taped (with single-sided invisible

tape, Staples, Framingham, MA) to the PDMS–array chip assembly to seal and hold the

device together to ensure that the solution would not leak out (see Figure 4.1a). The

volume of the solution plug was large enough so that the array chip, the floor of the

device, and the glass slide, the lid of the device, prevented the plug's movement in the

vertical dimension. The MHD force then directed the plug's movement laterally in only

two dimensions. This assembly was placed on top of one of the flat sides of a NdFeB

cylindrical permanent magnet (a rod having dimensions of 1 in. diameter x 1 in. long,

Amazing Magnets®, Irvine, CA), so that the microband array (having overall dimensions

of ~3.1 mm x 2 mm for the set of 16 electrodes) was centered in the middle of the much

larger circularly-shaped plane of the magnet. A dc magnetometer, AlfaLab, Inc.,

measured 0.5 T at the array. The cell was filled with ~250 μL of supporting electrolyte

(0.1 M Tris buffer) containing a 1:1 mol ratio of oxidized and reduced forms of the

pumping species (2.5 mM $Ru(NH_3)_6^{2+}$ and 2.5 mM $Ru(NH_3)_6^{3+}$) through openings or
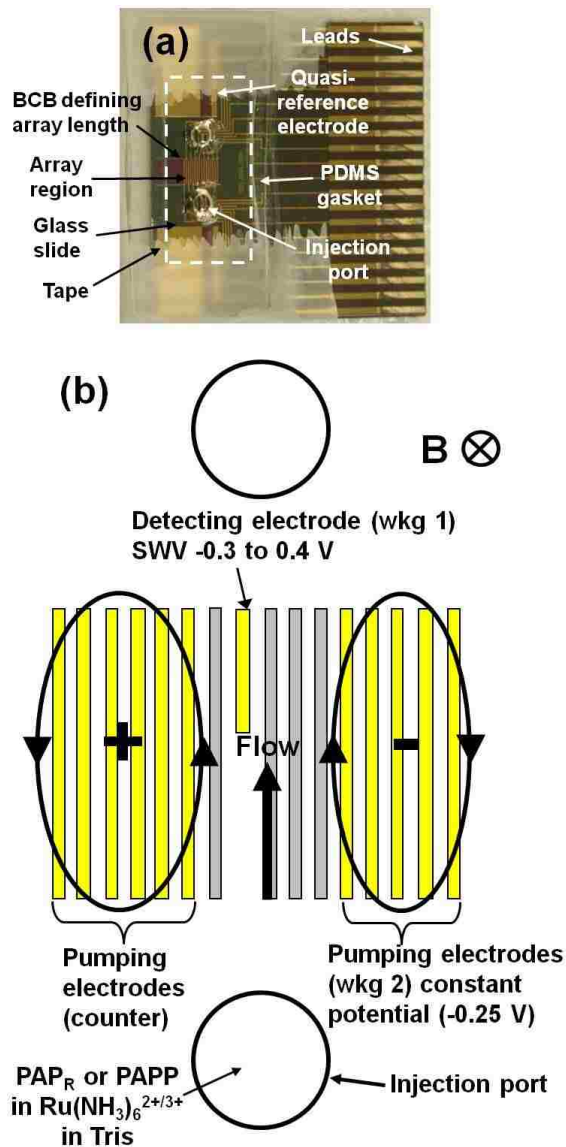
Figure 4.1. (a) Photograph of microelectrode array device showing PDMS gasket and glass slide with holes drilled through for solution access to cell, one serving as the injection site. The dashed white line traces the boundaries of the cutout in the PDMS that contains the solution. Tape secures the device together tightly to prevent leakage of solution and appears as a cloudy white boundary around three edges of the device. The magnet is not shown. (b) Schematic drawing of the experimental setup showing reinforcing flow over the detecting electrode between pumping electrodes. The injection site for introduction of plug (e.g. PAP_R or PAPP in Tris buffer) is also indicated.

ports in the glass lid. (For flow visualization experiments, microbeads were also added to the cell and tracked with video microscopy. Speeds were determined with a particle tracking software (World-In-Motion Physics Toolkit software (WIM, www.physicstoolkit.com).).) The 1:1 mixture provides the auxiliary electrode with electroactive species to counteract current at the working electrode(s) and avoid electrode dissolution and bubble formation. A 1.2 μL solution of 9.6 mM PAP_R (for control studies) or 8.3 mM PAPP (for enzyme conversion studies) in the pumping solution was then injected with a micropipet into the cell through the drilled hole upstream of the detecting electrode. The hole was strategically placed far enough from the array region that natural diffusion would take significantly more time than redox-MHD driven fluid flow to deliver species to the detector. The location of the injected fluid was also in line with the expected redox-MHD induced flow path.

Immediately after the plug was injected, the pumping and detecting electrodes were turned on in the presence of a magnetic field. A voltage of -0.25 V vs the quasi-reference electrodes at one set of pumping electrodes causes reduction there and oxidation at the other set of pumping electrodes (the auxiliary electrodes). In the presence of the magnet, this produces a reinforcing flow[19] pattern which causes solution to move in a path between the two sets of electrodes and across the detector, as illustrated in Figure 4.1b. Square wave voltammetry (SWV) from -0.3 to 0.4 V at a frequency of 25 Hz and amplitude of 50 mV at the detecting electrode allowed quantification of both, pumping species and PAP_R. Waveforms performed at each electrode are shown in Figure 4.5a,b.

Results and Discussion

96

To determine compatibility of this redox-MHD system for immunoassay applications, experiments were performed that involved detection of PAP_R, both, directly (control experiments), and PAP_R that was enzymatically generated by AP from its electroinactive PAPP substrate, in the presence of the redox-pumping species. This represents the signal transduction step in a typical heterogeneous, sandwich-type electrochemical immunoassay, where an enzyme such as AP is conjugated to a secondary antibody bound to the antigen that had been captured by an immobilized primary antibody. The PAP_R signal would then be proportional to the amount of antigen captured.[29]

Choice of pumping method: Reinforcing flows. Previous redox-MHD studies in a small confined volume have demonstrated that oppositely polarized microelectrodes result in a reinforcing flow configuration, which has several advantages.[19] One is that this configuration can achieve an increase in flow velocity by a factor of 2.5 compared to that for flow around a singly biased electrode. This configuration is also useful for pumping in a line, as if the device acts as a channel, but without walls. Additionally, the velocity profile between the active, oppositely biased electrodes is fairly uniform, minimizing flow distortion of the fluid front there and allowing for reproducible delivery of fluid between electrodes. Thus, all experiments were performed using this electrode configuration. An image and schematic of the experimental setup, for pumping studies (described below), are shown in Figures 4.1a and 4.1b, respectively.

Finding a compatible pumping species. One way to perform simultaneous pumping and detection without physically removing the redox pumping species is to find one that is compatible with the analyte of interest. Different redox species were

investigated to determine their electrochemical compatibility with a common, enzymatically generated species, PAP$_R$, produced in immunoassays. Cyclic voltammetry shows that the redox species Ru(NH$_3$)$_6{}^{2+}$ has a different half-wave potential than that of PAP$_R$ in 0.1 M Tris buffer (pH=9) and is therefore a suitable redox species to allow pumping to occur without oxidizing PAP$_R$. Thus, a solution containing 2.5 mM Ru(NH$_3$)$_6{}^{2+}$ and 2.5 mM Ru(NH$_3$)$_6{}^{3+}$ in 0.1 M Tris buffer (pH 9.0) was chosen as the pumping species. This concentration of pumping species was high enough to provide significant convection to move fluid across the detecting electrode and low enough to maintain ample detection of PAP$_R$ in its presence.

PAP$_R$ detection. The limit of detection for PAP$_R$, with and without the presence of the redox pumping species, was determined. Square wave voltammetry (SWV) was performed at the shortened detecting electrode (described below and indicated in Figure 4.1b) from -0.3 V to +0.4 V vs. Au quasi-reference at a frequency of 25 Hz and amplitude of 50 mV. Experiments were performed in an open cell (no PDMS or lid), without a magnet so that redox-MHD induced convection was not present, and in a Faraday cage. Previous studies have shown that at the low concentrations used here there is a minimal effect of the lid and magnet on the resulting voltammograms.[19] The detecting electrode was made shorter by taping off half of it and applying a very high potential (+5 V vs. Au quasi-reference) in a solution of 0.1 M Tris buffer to strip off the gold. The resulting electrode dimensions are 87-µm wide × 1-mm long. SWV responses, at this electrode, for varying concentrations of PAP$_R$ in 0.1 M Tris buffer are shown in Figure 4.2. The square wave voltammograms, as shown, represent a current difference (ΔI) between forward and reverse currents (similar to the anodic and cathodic currents
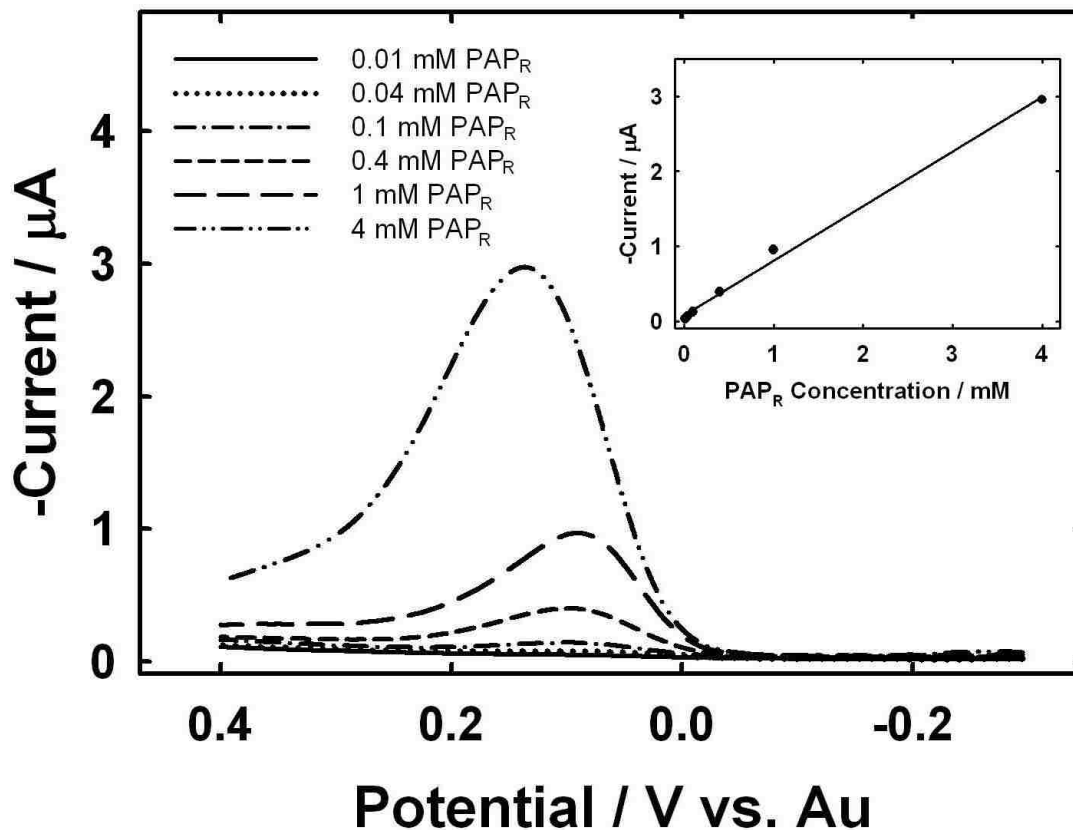
<u>Figure 4.2.</u> SWV responses at the 87-μm wide × 1-mm long Au detecting electrode in solutions of varying concentrations of PAP_R in 0.1 M Tris buffer (pH=9.0). An amplitude of 50 mV and frequency of 25 Hz were used. Experiments were performed in an open cell in the absence of a magnet. The inset is a plot of peak height as a function of PAP_R concentration. The equation of the best-fit line is y = 0.729 (± 0.0245) μA/mM x + 0.0783 (± 0.0415) μA, R^2 = 0.995. The experimental limit of detection for PAP_R was 0.01 mM.

observed in cyclic voltammetry); however, to be consistent with the present literature, the differential current is simply represented as "current" in the plots. The inset is a plot of peak current as a function of PAP_R concentration. PAP_R peak currents were determined by subtracting the maximum current for PAP_R (typically at ~+0.10 V) by the average of the background current in Tris (at -0.20 V). The equation for the calibration curve is $y = 0.729 (\pm 0.0245)$ μA/mM $x + 0.0783 (\pm 0.0415)$ μA, $R^2 = 0.995$. There appears to be a slight "roll-over" at the highest concentration (4 mM) in the calibration curve, but the source of that behavior has not been confirmed. It is possible that there was some electrode fouling in that concentration regime. The experimental limit of detection, as determined by a signal for PAP_R which was quantifiable over the background of Tris buffer, was 0.01 mM PAP_R. A limit of detection of 5.69 ± 0.19 μM was calculated using the standard equation, $3S_B/m$, where S_B is the standard deviation of the background (in our case, the standard deviation of six measurements of 0.1 M Tris (1.38 nA)) and m is the slope of the best fit line. (The error in the detection limit was obtained by propagating the error in the slope of the calibration curve (0.0245 μA/mM).) Detection limits reported in the literature range from ~5 to 1000 nM for varying electrochemical techniques including flow injection analysis with voltammetric detection,[29, 30] "twin mode" voltammetry (at an interdigitated electrode array),[26] cyclic voltammetry,[23] and amperometry and SWV using coated electrode surfaces.[31, 32]

In order to determine the limit of detection of PAP_R in the presence of the redox pumping species, SWV was performed on varying concentrations of PAP_R, all of which were prepared in a solution of 2.5 mM $Ru(NH_3)_6^{2+}$ and 2.5 mM $Ru(NH_3)_6^{3+}$ in 0.1 M Tris buffer. Raw data and the resulting calibration curve for PAP_R are shown in Figure 4.3.
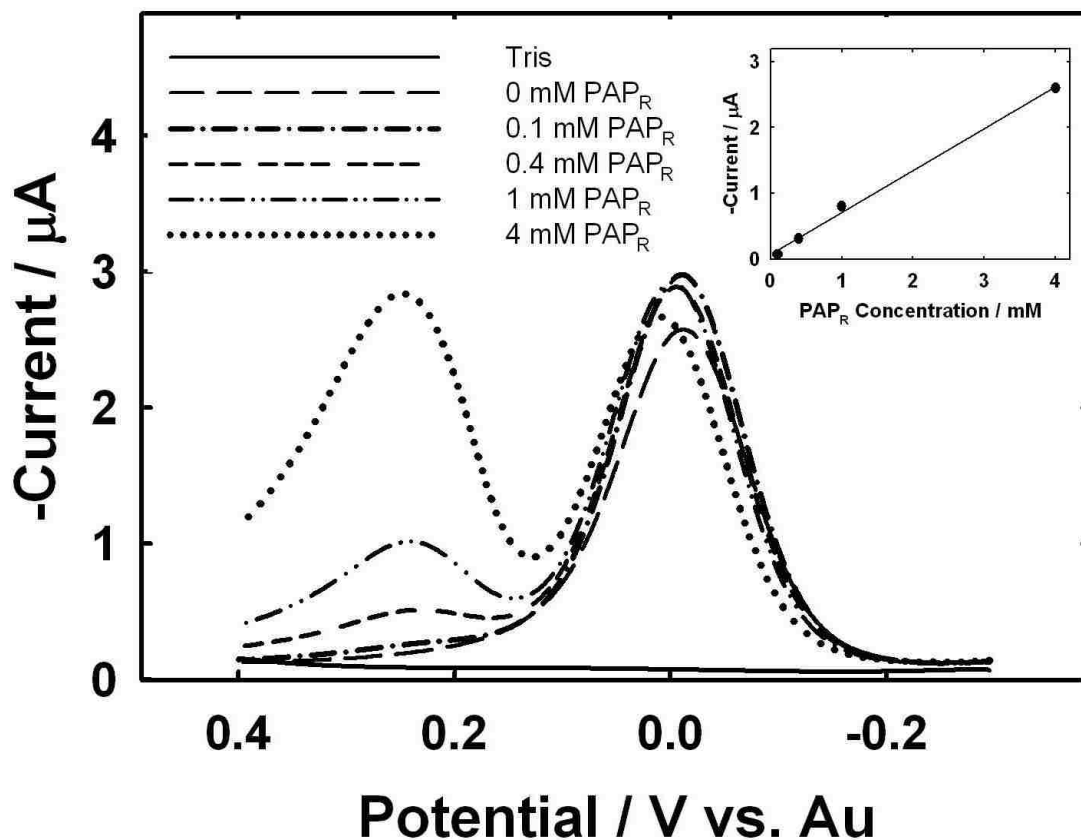
Figure 4.3. SWV responses obtained at an 87-μm wide × 1 -mm long Au detecting electrode of varying concentrations of PAP_R in a solution of 2.5 mM $Ru(NH_3)_6^{2+}$ and 2.5 mM $Ru(NH_3)_6^{3+}$ in 0.1 M Tris buffer (pH=9.0). An amplitude of 50 mV and frequency of 25 Hz were used. Experiments were performed in an open cell in the absence of a magnet. The inset is a plot of peak height as a function of PAP_R concentration. The equation of the best-fit line is $y = 0.638$ (± 0.0533) μA/mM x + 0.0678 μA (± 0.0257), R^2=0.997. The experimental limit of detection of PAP_R in the presence of the redox pumping species was 0.1 mM.

PAP$_R$ peak currents were determined by subtracting the maximum current at the half-wave potential for PAP$_R$ (at 0.26 V) by the average of the background current from Ru(NH$_3$)$_6$$^{2+/3+}$ (at 0.26 V). It was observed that the presence of the pumping species does in fact hinder the detection of PAP$_R$. This is due to the fact that the baseline of the signal from oxidation of ruthenium hexamine contributes to the background of PAP$_R$, thereby interfering with detection of PAP$_R$, at low concentrations. The equation of the best-fit line for the calibration curve is $y = 0.638$ ($\pm$ 0.0533) μA/mM $x + 0.0678$ μA ($\pm$ 0.0257), R^2=0.997. In the presence of the pumping species, the experimental limit of detection for PAP$_R$ was 0.1 mM, as determined by a signal for PAP$_R$ which was quantifiable over the baseline signal of Ru(NH$_3$)$_6$$^{2+/3+}$. This concentration of analyte is acceptable for the fundamental studies performed here. The calculated limit of detection for PAP$_R$ in the presence of the pumping species was 25.5 $\pm$ 1.0 μM, as determined by the equation above (the standard deviation of the background, 5.43 nA, was determined from the average current (n=5) of the signal from 2.5 mM Ru(NH$_3$)$_6$$^{2+}$ and 2.5 mM Ru(NH$_3$)$_6$$^{3+}$ in 0.1 M Tris buffer at +0.26 V). (The error in the detection limit was obtained by propagating the error in the slope of the calibration curve (0.0533 μA/mM).) This calculated detection limit is 4.5 times that for PAP$_R$ in the absence of the pumping species. Thus, a lower concentration of electroactive, pumping species, which does not interfere with detection of the analyte, but that still maintains sufficient flow velocities, is desirable (perhaps one where the E$°$ value has a greater separation from that of the analyte).

AP Enzyme Activity. The enzymatic generation of PAP$_R$ by AP from its electroinactive PAPP substrate, in the presence of the redox-pumping species, was evaluated. Varying concentrations of Ru(NH$_3$)$_6$$^{2+}$ and Ru(NH$_3$)$_6$$^{3+}$ in 0.1 M Tris buffer

were tested for their compatibility with the enzymatic reaction. Square wave voltammetry at a 44 μm wide x 2 mm long band electrode was performed in solutions containing PAPP and AP, only, in Tris buffer and PAPP, AP, and $Ru(NH_3)_6^{2+/3+}$ in Tris buffer. Plots of the electrochemical signal for PAP_R over time, in the absence and presence of different concentrations of redox-pumping species, are shown in Figure 4.4. Figure 4.4a shows results for a solution of 3.6 mM PAPP, and 0.5 mM AP, in the presence (red circles) and absence (black circles) of 2.5 mM total $Ru(NH_3)_6^{2+/3+}$. The slopes, indicated on the figure, represent the rate of change in electrochemical signal and thus correlate to the rate of generation of PAP_R (by AP) from PAPP. Figure 4.4b is a plot of PAP_R current over time, in Tris only, and in two different concentrations of redox-pumping species. The solutions consisted of 3.3 mM PAPP, 0.5 mM AP, and either, 2.5 mM each of $Ru(NH_3)_6^{2+}$ and $Ru(NH_3)_6^{3+}$ or 5 mM each of $Ru(NH_3)_6^{2+}$ and $Ru(NH_3)_6^{3+}$. The slopes were similar to the controls (no $Ru(NH_3)_6^{2+/3+}$ present) for the lower concentrations of redox-pumping species (2.5 mM and 5 mM total). When the concentration was increased to 10 mM total, even despite an increase in overall current, due to a greater background from the pumping species at that concentration, the slope was less than control studies. This may indicate that there is a decrease in enzymatic activity of AP at that high concentration of redox species or it may be attributed to difficulty in quantifying the signal for PAP_R in the presence of the high background signal.

Control Experiments Involving Introduction and Removal of PAP_R in the Plug (no enzyme present). Before introducing a more complicated solution involving an enzyme and one in which reactions take place, it was necessary to determine if PAP_R alone (no PAPP and no AP) could be directionally pumped and detected in the presence
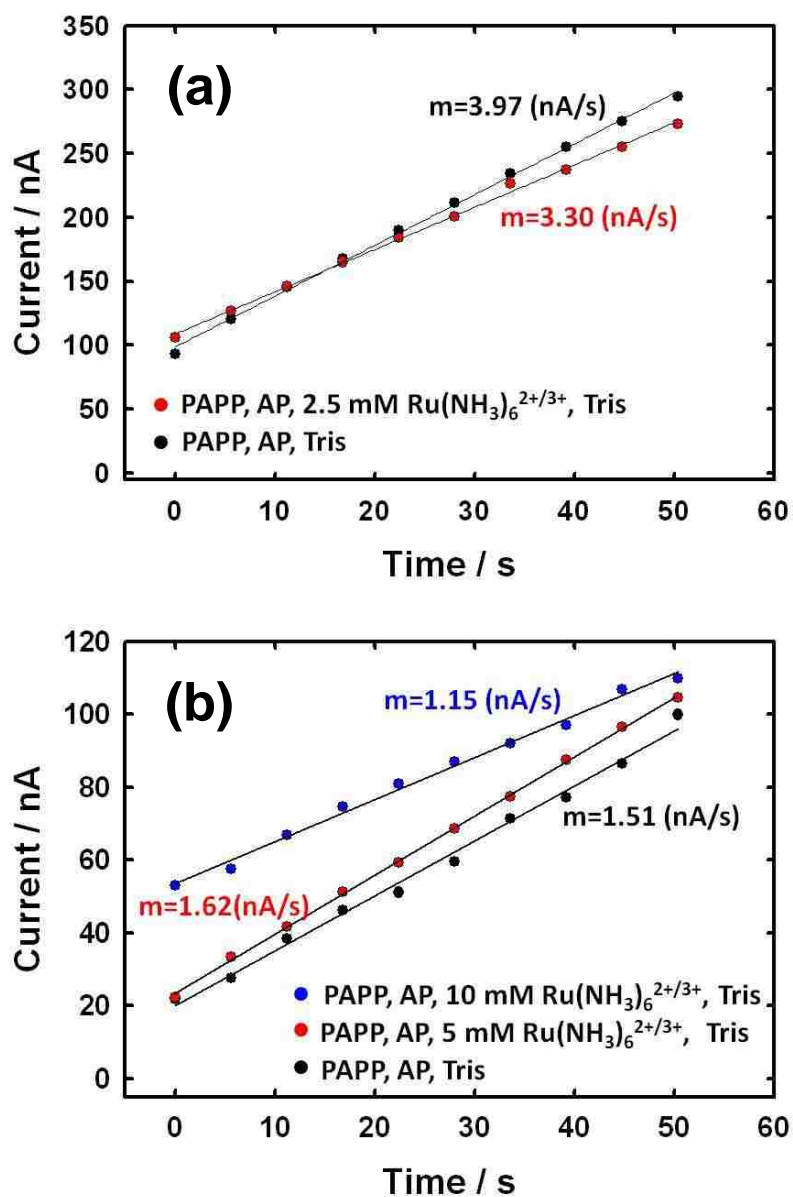
Figure 4.4. (a) Signal for enzymatically generated PAP_R over time in the presence (red circles) and absence (black circles) of 1.25 mM $Ru(NH_3)_6^{2+}$ and 1.25 mM $Ru(NH_3)_6^{3+}$. The solution also contained 3.6 mM PAPP and 0.5 μM AP. (b) PAP_R signal over time in the presence of 2.5 mM $Ru(NH_3)_6^{2+}$ and 2.5 mM $Ru(NH_3)_6^{3+}$ (red cirles), 5 mM $Ru(NH_3)_6^{2+}$ and 5 mM $Ru(NH_3)_6^{3+}$ (blue circles) and in the absence of any pumping species (black circles). The solution also contained 3.3 mM PAPP and 0.5 μM AP. The slopes from the best-fit lines are indicated on the plots.

of the redox pumping species. Also, the effect of the detecting electrode and of diffusion on the movement of the plug needed to be evaluated.

The introduction (arrival to the detecting electrode) and removal (departure of PAP_R away from the detecting electrode) of PAP_R was quantified by measuring its peak current at the detecting electrode in successive SWV responses (e.g. Figure 4.5a) and plotting the current as a function of time (Figure 4.5b for three different scenarios–one full and two control experiments). For all experiments, the cell was filled with a pumping solution of 2.5 mM $Ru(NH_3)_6{}^{2+}$ and 2.5 mM $Ru(NH_3)_6{}^{3+}$ in 0.1 M Tris buffer; a 1.2 μL plug of solution containing 9.6 mM PAP_R in the pumping solution was injected into the cell through the opening in the glass lid upstream of the detecting electrode. Injection of the plug was performed very carefully so as not to cause additional convection which might lead to faster or slower delivery of the PAP_R to the detecting electrode.

Visualization experiments were performed in a similar manner in which the cell was filled with the pumping solution containing 10 μm polystyrene microbeads, and a 1.2 μL plug of solution was injected. The device was placed under the microscope to determine if injection of the solution caused any convection. Bead movement was not observed when this was done indicating that this injection method does not lead to additional convection.

In one experiment, the pumping and detecting electrodes were turned on immediately after injection of PAP_R in the presence of a magnet, or "full operation mode". A top-down schematic representation of the movement of the plug from the injection site, across the array region, and to the detector is shown in Figure 4.5a. The

105

consecutive SWV responses are shown in Figure 4.5b and a plot of peak current over time for this scenario is represented by the closed circles in Figure 4.5c. It is observed that the signal for PAP_R increases over time from ~50 s (when PAP_R was initially detected) to a maximum between 150 and 160 s, indicating introduction of PAP_R to the detecting electrode. The signal then decreases indicating removal of PAP_R away from the detecting electrode. To quantify the rate of arrival of PAP_R at the detector, an equation of the best-fit line to the points on the rising slope of the curve was determined. Five points were used, the inflection point and the two points on either side. This is indicated by the black line in Figure 4.5c for the full operation mode only (regression lines for the control experiments were determined as well but are not shown on the figure). The equation of the best-fit line for arrival of PAP_R at the detector for that case is $y = 0.010$ (μA/s) $x -$ 0.56 μA ($R^2 = 0.995$). A control experiment was performed in which the pumping electrodes were not active and only the detecting electrode was turned on in the presence of a magnet. A plot of PAP_R signal over time for this scenario is shown in Figure 4.5c and is indicated by the filled squares. This study revealed that redox-MHD induced convection does occur, even when only the small detecting electrode is active. This was observed electrochemically in the rate of appearance of PAP_R, which was faster than experiments observed in the absence of a magnetic field, but slower than experiments performed with the pumping and detecting electrodes on.

The maximum peak current observed when only the detecting electrode was on was 37% that of the maximum current in full operation mode. The equation of the best-fit line for arrival of PAP_R at the detecting electrode was $y = 0.0021$ (μA/s) $x + 0.23$ μA ($R^2 = 0.992$), showing a growth of PAP_R signal that was only 20% of that during full

106
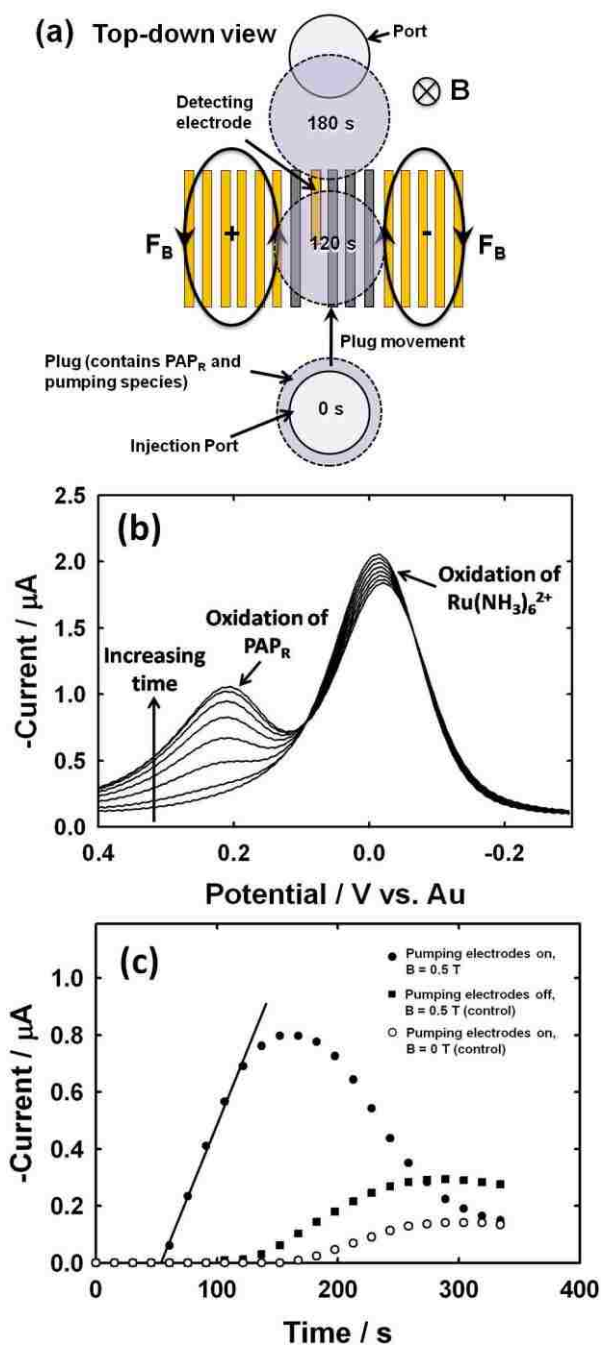
Figure 4.5.

Figure 4.5. (a) Top-down representation of pumping a plug (purple circle) at three different times from the injection site (at bottom of diagram) to the detecting electrode (at top) via reinforcing flow between pumping electrodes. (b) Example of SWV responses showing delivery of PAP_R in the plug to the detecting electrode over time during redox-MHD pumping. (c) Plots of the SWV peak current of PAP_R as a function of time. Filled circles correspond to the introduction and removal of PAP_R when pumping and detecting electrodes are on and with a magnet; raw data are in (b). Filled squares show PAP_R signal when only the detecting electrode is on (pumping electrodes off) and with a magnet. Open circles indicate peak current in the presence of active pumping and detecting electrodes but without a magnet. The solid line is the regression curve used to calculate the slope for the plug arrival rate during full operation.

operation mode. Changing the shape or decreasing the size of the detecting electrode may help to eliminate redox-MHD induced convection from the central detecting electrode so that it does not interfere with convection generated by the pumping electrodes. Smaller electrodes also provide advantages over larger electrodes such as a diminished iRu drop (therefore less error in potential experienced at the working electrode) and low capacitance (therefore lower background signal and faster response time).

Two final control experiments were performed to observe the effects of natural diffusion of the injected PAP_R plug in the absence of a magnet. The cell was filled with the pumping solution and a plug of 9.6 mM PAP_R was injected as before. In one case, both the pumping and detecting electrodes were turned on (Figure 4.5c, open circles), and in the other, only the detecting electrode was turned on (data not shown, but is consistent with pumping and detecting electrodes on). As shown in Figure 4.5c, the PAP_R peak current slowly grew in over time and eventually leveled off, as indicated by the open circles. The maximum peak current observed when the magnetic field was absent was 18% lower than that from the experiments described above, which were in the presence of a magnetic field. The best fit line equation for the arrival of PAP_R at the detecting electrode was y = 0.0014 (μA/s) x − 0.22 μA (R^2 = 0.997), having a slope that is only 13% of that when the magnet was present.

Several important outcomes from the above control experiments were revealed. It was observed that a plug of PAP_R introduced into the cell would eventually reach the detecting electrode. However, the arrival and departure of PAP_R at the detecting electrode was most efficient in the presence of a magnetic field and with both pumping

and detecting electrodes turned on. During full operation, the plug was pumped across the array, detected, and then pumped away from the detecting electrode. The plug arrival rate in full operation was five to seven times of those obtained from the control experiments. The presence of the detecting electrode in a magnetic field caused some redox-MHD induced convection; however it was not as great as when the pumping electrodes were turned on. Natural diffusion of PAP_R into the cell (control experiments performed with no magnetic field present) does occur but is much slower than any redox-MHD induced convection.

Effect of the Active Detecting Electrode on Redox-MHD Induced Convection by Monitoring Bead Movement. In the above discussion, the arrival and removal of PAP_R to and from the detecting electrode was determined by monitoring the current at that electrode, only. From these studies it was possible to infer an approximate time of the arrival of PAP_R at the detector based on the appearance of a signal for PAP_R in the SWV responses. However, these measurements did not reveal anything about the flow speed or overall path of the redox-MHD induced convection or the effect of an active detecting electrode between the pumping electrodes. Therefore, beads were monitored to further investigate the fluid flow more closely.

Flow visualization experiments were performed by filling the cell with a pumping solution of 2.5 mM $Ru(NH_3)_6^{2+}$ and 2.5 mM $Ru(NH_3)_6^{3+}$ in 0.1 M Tris buffer containing 10 μm polystyrene microbeads. To be consistent with the other experiments, a 1.2 μL volume containing PAP_R in the pumping solution was injected into the cell immediately before the electrochemistry was started. Bead movement in the presence of a magnet was observed with only the pumping electrodes on (waveform and flow path shown in
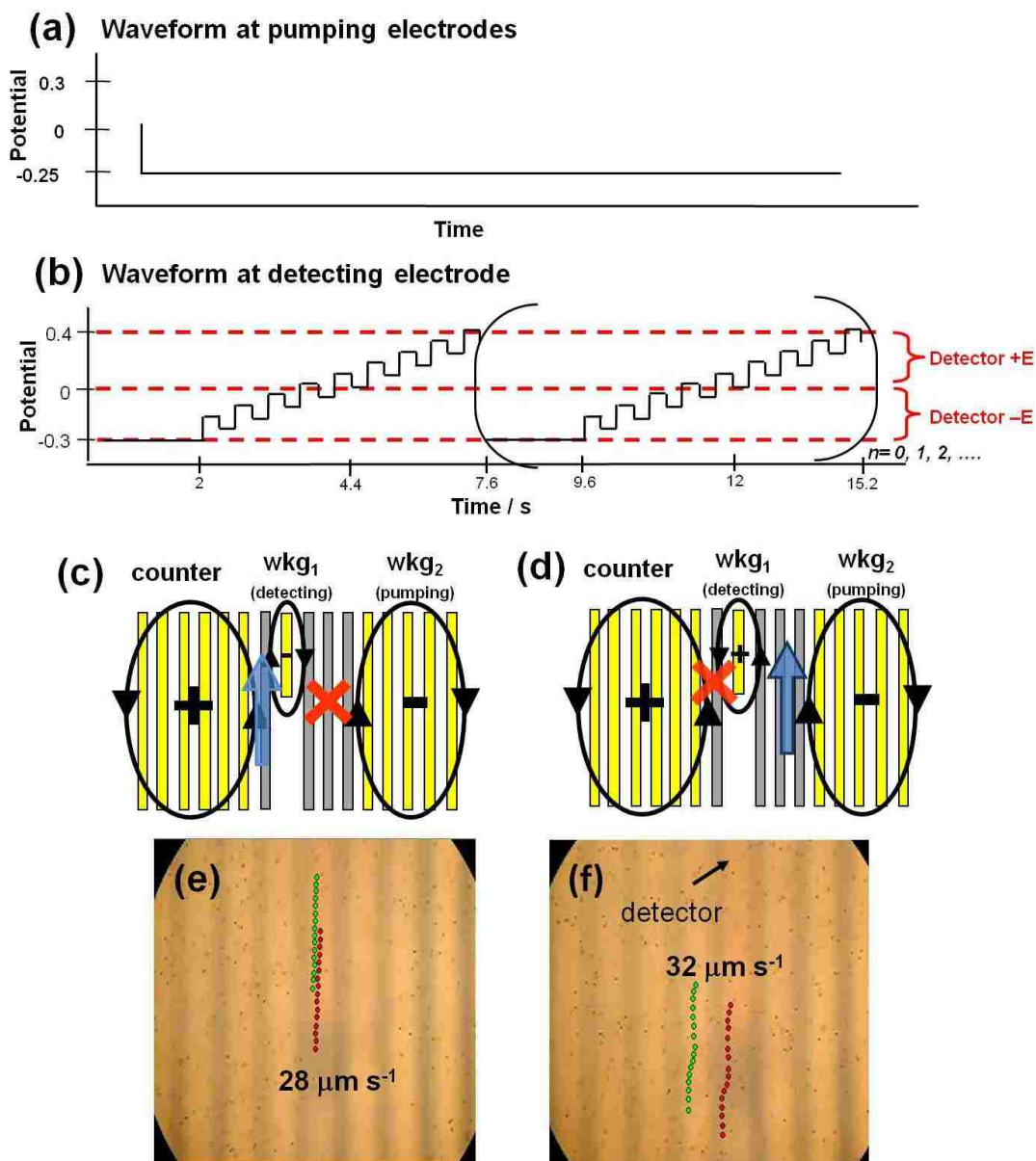
Figure 4.6. (a) Potential waveform performed at the pumping electrodes. A constant potential of -0.25 V vs. Au quasi-reference is applied to a set of five, 87-μm wide, 2-mm long Au bands. (b) Potential waveform performed at the detecting electrode. Square wave voltammetry is repeatedly performed from -0.3 to +0.4 V vs. Au quasi-reference at a single 87-μm wide Au band (shortened to 1 mm). A schematic representation of the expected flow path (during pumping) is shown when the detector is at reducing (c) and oxidizing (d) potentials during the SWV. Microscope images from video are shown where two microbeads were tracked (indicated as green and red) during the reinforcing flow caused by pumping electrodes when (e) the detecting electrode was off and (f) the detecting electrode was performing SWV. The average velocities of the beads, determined over 15 s, are indicated on the figure.

Figures 4.6a and 4.6e, respectively) and with both the pumping and detecting electrodes

on (waveforms are shown in Figures 4.6a and 4.6b, flow path is shown in 4.6f). Flow

patterns were slightly altered when the detecting electrode was on, as indicated by the

bead-tracking image shown in Figure 4.6f. Because the detecting electrode performs

SWV, from -0.3 to 0.4 V vs. Au quasi-reference, the electrode ramps from reducing (for

2.4 s) to oxidizing potentials (for 3.2 s) during the SWV run, thereby changing the

polarity of the current and the resulting flow velocities. Thus, at certain times, the flow

will be reinforcing on one side of the electrode and opposing on the other side, as shown

in Figures 4.6c and 4.6d, thereby causing the flow pattern shown in the Figure 4.6f.

However, it is observed that the particles move with similar *average* speed (~30 μm/s)

and in the same net direction for the case with and without an activated detecting

electrode. This is due to the fact that the current at the detecting electrode is much smaller

than the current at the pumping electrodes; thus the pumping electrodes dominate the

redox-MHD induced convection.

Experiments Involving Introduction and Removal of Enzymatically

Generated PAP$_R$ in the Plug. Once it was determined that PAP$_R$, injected directly into

the cell, could be pumped across the detector, and detected at an electrode separate from

the pumping electrodes in the presence of the redox-pumping species, a more

complicated system (one which involved the enzyme substrate, PAPP, and enzyme, AP,

to produce PAP$_R$) was tested. Again, the electrochemical cell was filled with 2.5 mM

Ru(NH$_3$)$_6$$^{2+}$ and 2.5 mM Ru(NH$_3$)$_6$$^{3+}$ in 0.1 M Tris buffer, but in this case, it also

contained AP at a concentration of 0.5 μM, which should be more than sufficient for

expedient conversion of PAPP to the electrochemically active species, PAP$_R$.[33] A plug of

8.3 mM PAPP (the enzyme substrate), in the pumping solution, was injected into the cell. A similar set of experiments to those performed above for control studies were carried out. A side-view schematic representation of the chemical and electrochemical reactions occurring in the cell is shown in Figure 4.7a. At the periphery of the plug, AP converts PAPP to PAP_R. At the working set of pumping electrodes, reduction of $Ru(NH_3)_6^{3+}$ takes place ($Ru(NH_3)_6^{3+} + 1\ e^- \rightarrow Ru(NH_3)_6^{2+}$), while at the counter set of pumping electrodes, oxidation of $Ru(NH_3)_6^{2+}$ occurs ($Ru(NH_3)_6^{2+} \rightarrow Ru(NH_3)_6^{3+} + 1\ e^-$). A steady-state current of ~2.1 μA was achieved at the pumping electrodes. Oxidation via SWV of both $Ru(NH_3)_6^{2+}$ and enzymatically generated PAP_R ($PAP_R \rightarrow PAP_O + 2\ H^+ + 2\ e^-$) takes place at the detecting electrode.

Consecutive SWV responses at the detecting electrode, demonstrating simultaneous monitoring of pumping species and PAP_R over time, are shown in Figure 4.7b and are consistent with control studies. It is observed that PAP_R is enzymatically generated in the plug, pumped across the detector, detected there, and then pumped away from the detector. PAP_R began to be detectable at ~50 s after introduction of the plug. The signal continued to increase until it reached a maximum of 0.48 μA at ~150 s. This current is only 9% of that which would be expected for an 8.3 mM solution of PAP_R (if complete conversion of PAPP to PAP_R were to take place) and corresponds to a concentration of enzymatically generated PAP_R of 0.65 mM (as determined from the calibration curve in Figure 4.3). The plug will undergo dilution as it travels from the injection port to the detector, which is responsible for some of the current loss, but it is also possible that there is incomplete conversion of PAPP to PAP_R as is further discussed below.

The change of signal with time was used to quantify the speed with which the plug components reach the detector. A plot of PAP_R signal over time is given in Figure 4.7c. The regression line for the delivery of enzymatically-generated PAP_R to the detector when the experiment was run in full operation, that is, pumping and detecting electrodes active in the presence of a magnet was y = 0.0071 (μA/s) x - 0.31 μA (R^2 = 0.994). When the pumping electrodes were left off as a control experiment, the maximum peak current was only 25% that of the maximum peak current from full operation and the best fit line was y = 0.0012 (μA/s) x - 0.12 μA (R^2 = 0.999), showing a growth of PAP_R signal that was only 17% of that with the pumping electrodes on. In a different control experiment, the absence of a magnetic field revealed an even lower maximum PAP_R peak current at 13% of the full operation maximum current with a best fit line of y = 0.0007 (μA/s) x - 0.08 μA (R^2 = 0.996), having a slope that is only 9.9% of that in full operation. A final control experiment in which AP was not present in the surrounding solution revealed no enzymatically generated PAP_R and results are overlain in Figure 4.7d.

These results show that the introduction and removal of in situ-generated PAP_R was most efficient during full operation, where the slope is 6–10 times of those from the control experiments. This indicates that the arrival of the plug is not just due to diffusion but rather due to substantial redox-MHD pumping that takes place, even with the low concentration of pumping species. Comparing these results to control experiments revealed that the maximum current for the detection of enzymatically generated PAP_R was only 67% of that expected for a plug of PAP_R injected directly into the cell and having the same starting concentration as the PAPP. (See Figure 4.5b) Because dilution effects should be similar for a plug containing PAPP and a plug containing PAP_R, the

(a) Side view of electrochemical cell

(b)

Oxidation of Ru(NH₃)₆²⁺

Increasing time

Oxidation of PAPᴿ

(c)

- Pumping electrodes on, B = 0.5 T
- Pumping electrodes off, B = 0.5 T (control)
- Pumping electrodes on, B = 0 T (control)
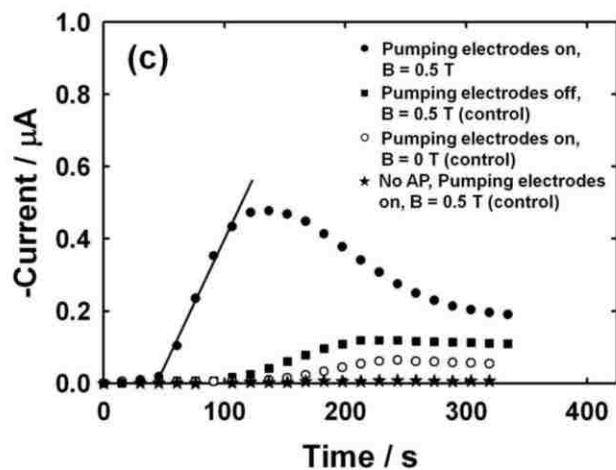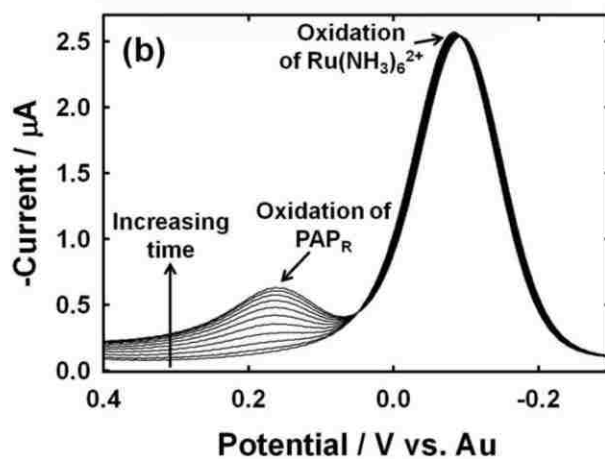- No AP, Pumping electrodes on, B = 0.5 T (control)
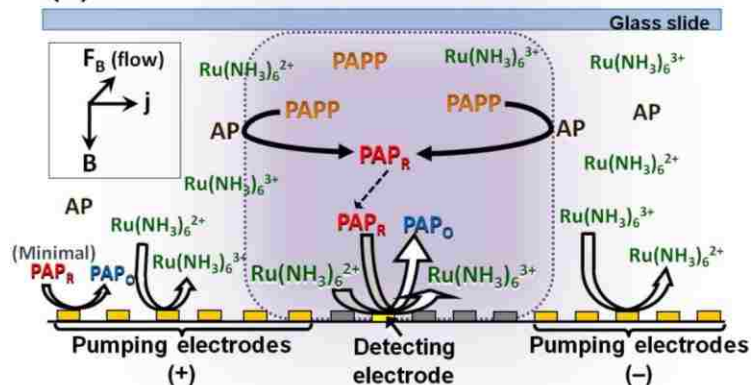
Figure 4.7

Figure 4.7. (a) Side-view of the electrochemical cell showing enzymatic conversion of PAPP to PAP_R via AP at the periphery of the plug (purple) and electrochemical determination of PAP_R at the detecting electrode. The oxidation and reduction of $Ru(NH_3)_6^{2+}$ and $Ru(NH_3)_6^{3+}$, respectively, at pumping electrodes in the presence of a magnetic field move the plug. The direction of the ion flux, magnetic flux density, and resulting F_B (flow) are indicated. (b) SWV responses showing delivery of enzymatically generated PAP_R to the detecting electrode with redox-MHD pumping over time. (c) Plots of SWV peak current of enzymatically generated PAP_R as a function of time show arrival and removal of enzymatically generated PAP_R. Filled circles show results obtained in full operation. Filled squares are for a control study when the detector was on, only, in the presence of the magnetic field. Open circles correspond to an experiment in the absence of a magnetic field. Stars represent results when AP was not present in the surrounding solution, but otherwise the device was in full operation. The solid line is the regression curve used to calculate the slope for the plug arrival rate during full operation.

lower current for the enzymatically generated PAP_R in the PAPP plug is likely due to insufficient time for complete conversion of the PAPP to PAP_R before the injected plug reaches the detector.

Conclusions

It has been demonstrated for the first time that pumping via redox-MHD, from oxidation and reduction of redox species at large microband electrodes, can be used to deliver a different electroactive species to a separate microelectrode for electrochemical detection there, all on a single device. This was accomplished using a low concentration of a redox-pumping species (5 mM total) so that detection of a separate analyte, in its presence, was possible without having to physically remove the pumping species before detection, thus overcoming original concerns of the use of redox-MHD for analytical applications. This is the lowest concentration reported to date to induce redox-MHD convection at microelectrodes in the presence of a low B-field for microfluidics in small volumes. A suitable pumping species ($Ru(NH_3)_6^{2+}$ and $Ru(NH_3)_6^{3+}$) for detection of PAP_R, the product of a common enzymatic reaction used in electrochemical immunoassays, while maintaining AP enzyme activity, and compatibility with enzyme substrate and buffer was found. Simultaneous pumping without a channel to guide a fluid plug (via redox-MHD) and detection (via electrochemistry) is possible. Channelless designs provide great flexibility in device fabrication. Directing flow to specific locations at different times is easily accomplished by activating different electrodes patterned on a chip. It was determined that a small detecting electrode between pumping electrodes only minimally alters flow velocities or trajectories. These preliminary results suggest that integrating redox-MHD microfluidics into a device offers unique opportunities for

and is compatible with lab-on-a-chip applications. Future work will involve performing a full, multistep assay which will require a modified microfluidic design to perform multisolution introduction and removal as well as regions for mixing on-chip to decrease incubation times.

Acknowledgements

References

(1)   Manz, A.; Graber, N.; Widmer, H. M. *Sensors and Actuators B-Chemical* **1990**, *1*, 244-248.

(2)   Bruin, G. J. M. *Electrophoresis* **2000**, *21*, 3931-3951.

(3)   Harrison, D. J.; Manz, A.; Fan, Z. H.; Ludi, H.; Widmer, H. M. *Analytical Chemistry* **1992**, *64*, 1926-1932.

(4)   Whitesides, G. M.; Stroock, A. D. *Physics Today* **2001**, *54*, 42-48.

(5)   Aguilar, Z. P.; Arumugam, P. U.; Fritsch, I. *Journal of Electroanalytical Chemistry* **2006**, *591*, 201-209.

(6)   Arumugam, P. U.; Fakunle, E. S.; Anderson, E. C.; Evans, S. R.; King, K. G.; Aguilar, Z. P.; Carter, C. S.; Fritsch, I. *J. Electrochem. Soc.* **2006**, *153*, E185-E194.

(7)   Qian, S. Z.; Bau, H. H. *Mechanics Research Communications* **2009**, *36*, 10-21.

(8)   Weston, M. C.; Gerner, M. D.; Fritsch, I. *Analytical Chemistry* **2010**, *82*, 3411-3418.

(9)   Bau, H. H.; Zhu, J. Z.; Qian, S. Z.; Xiang, Y. *Sensors and Actuators B-Chemical* **2003**, *88*, 205-216.

(10)   Eijkel, J. C. T.; Dalton, C.; Hayden, C. J.; Burt, J. P. H.; Manz, A. *Sensors and Actuators B* **2003**, *92*, 215-221.

(11)   Homsy, A.; Linder, V.; Lucklum, F.; de Rooij, N. F. *Sensors and Actuators B-Chemical* **2007**, *123*, 636-646.

(12)   Jang, J.; Lee, S. S. *Sensors and Actuators A* **2000**, *80*, 84-89.

(13)   Nguyen, B.; Kassegne, S. K. *Microfluidics and Nanofluidics* **2008**, *5*, 383-393.

(14)   West, J.; Karamata, B.; Lillis, B.; Gleeson, J. P.; Alderman, J.; Collins, J. K.; Lane, W.; Mathewson, A.; Berney, H. *Lab Chip* **2002**, *2*, 224-230.

(15)   Zhong, J. H.; Yi, M. Q.; Bau, H. H. *Sensors and Actuators a-Physical* **2002**, *96*, 59-66.

(16)   Anderson, E. C.; Fritsch, I. *Anal. Chem.* **2006**, *78*, 3745-3751.

(17)   Clark, E. A.; Fritsch, I. *Anal. Chem.* **2004**, *76*, 2415-2418.

(18)   Weston, M. C.; Anderson, E. C.; Arumugam, P. U.; Yoga Narasimhan, P.; Fritsch, I. *Analyst* **2006**, *131*, 1322-1331.

(19)   Anderson, E. C.; Weston, M. C.; Fritsch, I. *Analytical Chemistry* **2010**, *82*, 2643-2651.

(20)   Bange, A.; Halsall, H. B.; Heineman, W. R. *Biosensors and Bioelectronics* **2005**, *20*, 2488-2503.

(21)   Duan, C. M.; Meyerhoff, M. E. *Analytical Chemistry* **1994**, *66*, 1369-1377.

(22)   Fakunle, E. S.; Aguilar, Z. P.; Shultz, J. L.; Toland, A. D.; Fritsch, I. *Langmuir* **2006**, *22*, 10844-10853.

(23)   Aguilar, Z. P.; Vandaveer, W. R.; Fritsch, I. *Analytical Chemistry* **2002**, *74*, 3321-3329.

(24)   Driskell, J. D.; Uhlenkamp, J. M.; Lipert, R. J.; Porter, M. D. *Analytical Chemistry* **2007**, *79*, 4141-4148.

(25)   Choi, J. W.; Oh, K. W.; Thomas, J. H.; Heineman, W. R.; Halsall, H. B.; Nevin, J. H.; Helmicki, A. J.; Henderson, H. T.; Ahn, C. H. *Lab on a Chip* **2002**, *2*, 27-30.

(26)   Niwa, O.; Xu, Y.; Halsall, H. B.; Heineman, W. R. *Analytical Chemistry* **1993**, *65*, 1559-1563.

(27)   Thompson, R. Q.; Porter, M.; Stuver, C.; Halsall, H. B.; Heineman, W. R.; Buckley, E.; Smyth, M. R. *Analytica Chimica Acta* **1993**, *271*, 223-229.

(28)   Deriemer, L. H.; Meares, C. F. *Biochemistry* **1981**, *20*, 1606-1612.

(29)   Tang, H. T.; Lunte, C. E.; Halsall, H. B.; Heineman, W. R. *Analytica Chimica Acta* **1988**, *214*, 187-195.

(30)   Xu, Y.; Halsall, H. B.; Heineman, W. R. *Journal of Pharmaceutical and Biomedical Analysis* **1989**, *7*, 1301-1311.

(31)   Atta, N. F.; Galal, A.; Karagozler, A. E.; Russell, G. C.; Zimmer, H.; Mark, H. B. *Biosensors & Bioelectronics* **1991**, *6*, 333-341.

(32)   Zhang, X. H.; Wang, S. F.; Shen, Q. H. *Microchimica Acta* **2005**, *149*, 37-42.

(33)   Kreuzer, M. P.; O'Sullivan, C. K.; Guilbault, G. G. *Analytica Chimica Acta* **1999**, *393*, 95-102.

Chapter 5

Investigations into Maximizing Flow Velocities from Redox-Magnetohydrodynamic Induced Convection while Minimizing the Redox Species Concentration: Harnessing the High Ion Flux from the Faradaic Transient Current

Abstract

There is a need for a microfluidic pumping technique which is simple to fabricate, yet robust, compatible with a variety of solvents, and easy to control fluid flow. Redox-MHD offers these advantages. However, until recently, the presence of high concentrations of redox species, necessary to induce sufficient convection at low magnetic fields, limits the use of redox-MHD for analytical applications. A new method for redox-MHD pumping is investigated that takes advantage of the high faradaic transient current that occurs upon stepping the potential past $E°$ of the pumping redox species at an electrode. This approach increases flow velocity for a given redox concentration. An electronic switch was implemented between the potentiostat and electrochemical cell to alternately turn on and off different electrodes along the length of the flow path to maximize this transient current and as a result, the flow rates. Velocities were determined by tracking microbeads in a solution of electroactive potassium ferro- and ferricyanide in the presence of a magnetic field. Steady velocities were obtained with the switch that were 70% faster than velocities without the switch. This indicates that redox species concentrations can be lowered by a similar amount to achieve a given speed, thereby minimizing problems that can be associated with the presence of redox species in redox-MHD microfluidics.

Introduction

A well-known phenomenon associated with an electrochemical reaction is the transient faradaic current which occurs when the voltage at the electrode is stepped to potentials beyond the equilibrium potential of the solution to convert oxidized species to the reduced form, or visa versa. This results in a high, initial current due to conversion of the electroactive species at the electrode surface, which are initially at the highest concentration, the bulk concentration, before they are depleted by electron transfer events. The work reported herein involves investigations into using this transient current to maximize redox-magnetohydrodynamic flow in order to ultimately minimize the necessary concentration of redox species.

Magnetohydrodynamics (MHD) for use in analytical applications, and particularly for microfluidics, is still in its infancy. MHD is based on the interaction of a net ion flux, $\mathbf{j}$, perpendicular to a magnetic field, $\mathbf{B}$, to generate a magnetic force, $\mathbf{F_B}$, to induce fluid convection ($\mathbf{F_B} = \mathbf{j} \times \mathbf{B}$; where $\mathbf{F_B}$ can be proportional to velocity[1]). MHD has only recently (in the past ten years) been studied as a microfluidic technique. Most of these reports, many of which have been recently reviewed,[2-4] require high voltages to induce solution convection. These high voltages result in bubble formation, due to the electrolysis of water, which can cause interferences with the pumping. Electrode degradation is also a problem at these high potentials thereby limiting the lifetime of these devices.

Adding electroactive species, which undergo oxidation and reduction at the electrodes, can result in faradaic processes which yield high currents with low voltages

and can therefore alleviate problems of electrode degradation and water electrolysis. This approach, termed redox-MHD, is the focus of this work. Redox-MHD has often been characterized by measuring changes in currents and/or by using colored redox species to study convection.[5-9] However, most of these reports are fundamental studies of the phenomenon, and thus, do not have any direct, practical application. The reports that suggest the use of redox-MHD for application-based microfluidics[10-18] make use of relatively high concentrations of redox species to induce convection in the presence of the low magnetic flux densities of small permanent and microfabricated electromagnets of interest for small devices.

However, high concentrations of redox molecules cause interferences in detection methods by either "drowning out" the signal of the analyte of interest or through chemical or electron transfer reactions with the analyte of interest. For example, in redox-MHD enhancements of anodic stripping voltammetry,[11, 14, 17] it was necessary to perform a manual rinsing step to remove the pumping species prior to the detection step, complicating the procedure. In another example, redox-MHD was demonstrated for the simultaneous pumping and detection of a plug of solution using a low enough concentration (5 mM) of pumping redox species, so that a rinse step was not necessary and quantification of the analyte (enzymatically-generated p-aminophenol) was still possible.[19] Yet, the detection limits for the analyte were about five times higher in the presence of the pumping species than without. Thus, it is desirable, for the development of redox-MHD microfluidic systems, to further decrease the necessary concentration of the pumping redox species to maintain the same velocities, while lowering detection limits and lessening reactive interferences.

There are two ways in which the magnetic force can be increased to ultimately lead to enhanced velocities: increasing the ion flux or increasing the magnetic flux density. Generally, the largest magnetic flux densities are generated from electromagnets, in which the magnetic field is produced by an electric current. This therefore requires an additional, external power source which limits applicability for use in small-scale, portable devices. There may be ways in which to increase the field of permanent magnets while maintaining the small size by connecting two permanent magnets with a high magnetic permeability metal in the attracting position or by patterning magnets into microfluidic devices with screen-printed magnetic inks which could possibly eliminate the need for an external magnet at all. These options are interesting; however they are beyond the scope of this chapter. In attempts to improve redox-MHD fluid flow for a given redox concentration, or to use a lower redox concentration to obtain a given speed, a method for optimizing the current produced in the system is explored here.

There are a couple of methods possible for optimizing the current in the system. One method for increasing the current is to increase the electroactive area. However, significantly increasing the area will occupy precious space in small-scale devices which are desirable for lab-on-a-chip applications. It is also possible to increase the applied potential to generate higher currents but it is only possible to increase the potential to a point at which there are diminishing returns (the ratio of oxidized and reduced forms of a redox couple are determined by a logarithmic function of the Nernst equation) and where the current becomes mass-transfer limited. It is therefore, interesting, to study alternative approaches to increase the current in these systems.

The methods reported here for maximizing current while minimizing redox species concentration to yield faster velocities all involve using the high transient faradaic current associated with a potential step experiment. Fluid velocities, as estimated by tracking microbeads over microelectrode arrays in a small cell containing a solution of electroactive potassium ferri- and ferrocyanide, were studied as a function of time and with different potential waveforms, in the presence of a small permanent NdFeB magnet, to determine parameters that will lead to an enhanced magnetic force. Fundamental studies using the high, initial transient current to push fluid are presented. Velocities were enhanced by incorporating a "switch" between the potentiostat and electrochemical cell to alternate turning electrodes on and off at selected times to increase the current in the system. The results reported herein are significant for the development of redox-MHD microfluidic systems, in which the presence of redox species is necessary to avoid bubble formation and electrode degradation, but lower concentrations are desirable in order for quantification of other analytes to occur in its presence.

Experimental

Chemicals and materials. All chemicals were of analytical grade and used as received. Aqueous solutions were prepared with reagent grade, 18 megohm, deionized water from Ricca Chemical Company (Arlington, TX). Potassium ferricyanide ($K_3Fe(CN)_6$) was obtained from EM Science (Gibbstown, NJ) and potassium ferrocyanide trihydrate ($K_4Fe(CN)_6 \cdot 3H2O$) was from J.T. Baker (Phillipsburg, NJ). Potassium chloride was purchased from Aldrich Chemical Co. (St. Louis, MO). Polystyrene latex microspheres (10 μm diameter), functionalized with surface sulfate groups (2.5 wt% dispersion in water), were obtained from Alfa Aesar (Ward Hill, MA).

126

Polydimethylsiloxane (PDMS) supplies (Sylgard® 184 silicone elastomer base, Sylgard® 184 silicone elastomer curing agent, and OS-30 solvent) were obtained from Dow Corning Corp. Silicon wafers (125 mm diameter and 600-650 μm thickness) with 2 μm of thermally grown SiO_2 were purchased from Silicon Quest International (Santa Clara, California) and were used as the substrate materials for electrode array fabrication. A gold coin (Canadian Maple Leaf, 99.99%) and a chromium-plated tungsten rod (Kurt J. Lesker Company, Clairton, PA) were used for metal deposition onto the silicon wafer for the electrode arrays. Benzocyclobutene, BCB, (Cyclotene 4024-40) was used to insulate the electrode leads and was purchased from Dow Corning Company.

Microelectrode array chip fabrication. Array chips were fabricated through photolithography using two photoplot masks (Advance Reproductions Corporation, North Andover, MA): one for the metal electrode layer and one for the BCB layer. Oxidized silicon wafers were used as substrates for fabrication. The electrode layer consists of 50 Å Cr (for adhesion) and 500 Å Au, both deposited with an Edwards 306 Auto thermal evaporator. Positive photoresist (AZ4330RS) was spin-coated onto the gold-covered wafers at 6000 rpm for 60 s to create a 2.8 μm thick layer of photoresist. The photoresist underwent a soft-bake by placing the wafer in the oven for 20 min at 90 ºC. The photoresist was then patterned using the electrode photoplot mask, and was exposed to UV light for 10 s; exposed areas were dissolved away by AZ400K photoresist developer (Hoechst-Celanese). The unexposed areas of photoresist, which remained on the wafer after the development step, protected the underlying metal from the wet metal etch step. The Au was etched for 30 s with a solution of KI (50 g) and I_2 (12 g) in water (500 mL), and the Cr was etched for ~15 s with CEP-200 Chrome Etchant (Microchrome

Technology, San Jose, CA). The photoresist was then removed by exposing the wafer to UV light for 30 s and was dissolved away using the developer.

In order to insulate the leads and define the electroactive area, the wafers were spin-coated with 5 μm of BCB (a negative photoresist), using VM652 adhesion promoter (HD Microsystems). A soft-bake of the BCB was performed at 105 ^{0}C for 2 min followed by 45 ^{0}C for 30 s . The second photoplot mask was aligned using Au alignment marks present on the first layer in order to pattern the BCB. After exposure, the unexposed areas were dissolved away by DS2100 developer (Dow Chemical Company). The wafers were then rinsed with T1100 rinse solvent (Dow Chemical Company). The BCB was cured at 150 ^{0}C for 15 min, and at 250 ^{0}C for 60 min. A descumming procedure was then performed with reactive ion etching (RIE) to remove the polymer residue that remains behind in the developed regions. The 90 s RIE program used a mixture of O_2 (32 sccm) and SF_6 (8 sccm) at 250 mtorr and 200 W RF power (Unaxis PlasmaTherm SLR 720). After the RIE, the wafers were diced into 1 in. x 1 in. chips.

Experimental setup. The experimental setup is described in detail elsewhere.[12] Briefly, a microelectrode array chip is placed on top of a NdFeB permanent magnet. A PDMS film (760 μm thick) with a rectangular opening (14.0 mm x 6.0 mm) cut into it to expose the array region to solution, and serve as the cell sidewalls and define the height of the cell, is placed on top of the microelectrode array chip. The opening in the PDMS film is filled with a solution of potassium ferri- and ferrocyanide (at a 1:1 ratio) and potassium chloride in water containing microbeads. A glass microscope slide is placed on top of the PDMS gasket to confine the solution and form the top wall. The entire apparatus is placed under a Nikon Eclipse ME600P microscope, interfaced to a Sony

Handycam digital camera (model no. HDR-XR500V; 30 frames per second with 1920 x 1080 pixels per frame), to record movies for visualizing fluid flow. A photograph of the experimental setup is shown in Figure 1a. Video processing for bead tracking was performed using World-In-Motion Physics Toolkit software (WIM, www.physicstoolkit.com). A scale (pixel to distance ratio) was set in the WIM software and was based on the known, experimentally determined (via microscope measurements), distance between electrodes. The position of the bead at each frame was recorded with the WIM software. This data was then entered into Microsoft Excel and the bead velocity was calculated by dividing the total distance travelled by the amount of time from the first to last frame.

Magnetic field. A 1 in. x 1 in. x 0.5 in. permanent, NdFeB sintered magnet (1.23 T residual induction, 0.55 T on the surface, Magnet Sales Co.) was used for the redox-MHD studies. The array chip was placed directly on the magnet. The north pole pointed downward, perpendicular to the plane of the chip. The magnetic field at the array was measured to be 0.38 T by a DC magnetometer (AlfaLab Inc.).

Electrode configurations. There are two types of microelectrode arrays used in this study; each chip is 1 in. x 1 in. The first design consists of an array of 16 individually-addressable microband electrodes. The bands are 2 mm in length and 44 μm in width, separated horizontally by 56 μm gaps. Fabrication of these arrays is described in detail elsewhere[12] and is similar to that described above. This design is pictured in Figure 5.1b. The second design contains two parallel linear arrays of individually-addressable electrodes. The arrays are separated by a distance of 243 μm and each has 9
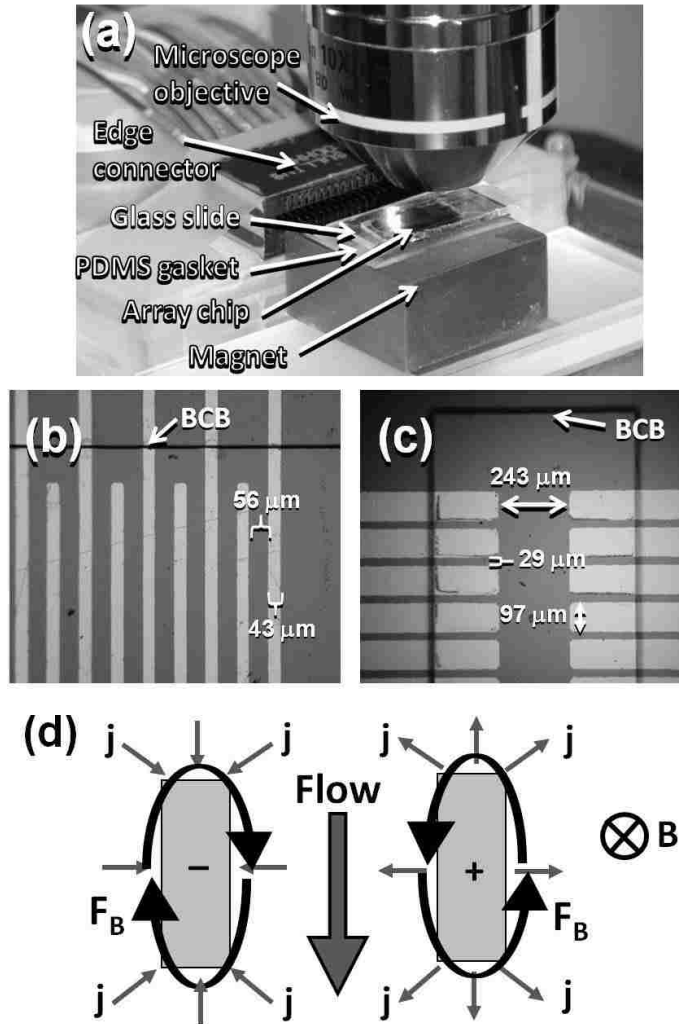
Figure 5.1. (a) Photograph of experimental setup showing method for tracking microbeads in solution. (b) Microscope image of the type of array used for "ratcheting flow" experiments. (c) Microscope image of type of array used for "switching" experiments. (d) Schematic of reinforcing flow achieved between oppositely biased electrodes. This configuration was used for all studies.

rectangular pumping electrodes, to total 18 all together. Each electrode is 215 μm in width and 97 μm in length, separated from adjacent electrodes within a linear array by 29 μm. The array region of this device is pictured in Figure 5.1c.

In both devices, the electrode configuration used is similar; one set of electrodes serves as the working electrode (anode) while another set of electrodes, some distance away from the working electrode, serves as the combined auxiliary and quasi-reference electrode (cathode). In this configuration, the MHD forces at the electrodes act in a reinforcing way, resulting in solution movement in a path between the two electrodes. A schematic representation of the current vectors, magnetic field, and resulting MHD force (flow) is shown in Figure 5.1d.

The effect of the distance between oppositely polarized electrodes producing ratcheting-reinforcing flows was investigated. This gap effect has been studied previously and results obtained here are fairly consistent with those obtained there.[12] The main difference between these studies and previous ones were that the auxiliary and quasi-reference electrodes were incorporated into the array to generate the reinforcing flows as opposed to other studies in which the auxiliary electrodes were far from the array and reinforcing flow was generated using two, oppositely polarized, working electrodes. It was observed that as the electrodes are moved very far apart, the interaction between the MHD forces will be less causing particle velocity to decrease. As they are moved closer together, the MHD forces begin to act in a reinforcing way, and velocities increase. However, as they are moved very close together, shear stress from solution moving in an opposite direction around the band electrodes causes velocities to further decrease. A separation of 550 μm was chosen as optimal and was used for the majority of the

131

following experiments. The second device design (Figure 5.1c) has yet to be optimized to achieve maximum flow velocities. A gap size of 243 μm between reinforcing flows was used for all studies involving that array chip.

Electrochemical control. A CHI 760B bipotentiostat (CH Instruments, Austin, TX) was used for chronoamperometry (CA) and sweep-step function (SSF). A CHI 1030A multipotentiostat was used for control (CA experiments) and switching experiments. For all studies, either one or two electrodes that served as the anode were connected to the working lead of the potentiostat and held at +0.3 V relative to two electrodes that served as the cathode and were connected to the shorted auxiliary and reference leads from the potentiostat. Switching experiments involved alternately activating (+0.3 V) and inactivating (open circuit) two sets of paired electrodes. The solution always contained a 1:1 mol ratio of $K_3Fe(CN)_6$ and $K_4Fe(CN)_6$, in 0.1 M KCl. Microbeads (polystyrene, 10 μm in diameter) were pipetted into the redox solution to achieve a 30X dilution of the beads (from 2.5% to 0.083% wt dispersion).

Switch design. An electronic circuit was designed to automatically switch the two sets of paired electrodes between active and inactive modes. Basically, the circuit consists of a clock pulse generator for timing and an analog switch to connect the leads from the potentiostat to the electrodes (cell). The clock pulse generator has two momentarily stable states, between which it continuously alternates, remaining in each form for a period of time and controlled by the adjustable circuit parameters. The clock is applied to the latches which switch the output of the potentiostat to the cell at designated times. A high transition of the clock switches on a latch, to transfer the voltage from the potentiostat to

132

the cell, for the duration of the clock; a low transition of the clock keeps the latch in the

off state.

Results and Discussion

       The transient-current response. A feature of the electrochemical signal obtained

when a potential-step (like in chronoamperometry, CA) is made to a value well-past E°

for a redox couple is an initial spike in current due to charging of the electrode surface

and electrochemical conversion of the species immediately adjacent to the electrode. The

faradaic portion dominates the transient current once most of the charging current has

died off and has a $t^{-1/2}$ decay due to depletion of species because of linear diffusion-

limited arrival at the electrode. For a microelectrode at long time scales in static solution

the current eventually reaches a steady- or pseudo-steady state due to the radial

component of diffusion. A plot of current as a function of time for a simple potential step

procedure at a 43 μm band electrode, separated from the combined auxiliary and pseudo-

reference by 150 μm, in a solution of 0.3 M $Fe(CN)_6^{3-}$ and 0.3 M $Fe(CN)_6^{4-}$, is shown in

Figure 5.2a and follows the expected trend. A plot of the corresponding bead velocity for

this current signal is shown in Figure 5.2b and an image of two beads tracked in solution

(black and white markers) from 0 to 2.6 s is shown in Figure 5.2c. The similar trends of

current and velocity with time suggest that current is proportional to velocity and is

consistent with previously reported results for redox-MHD in small volumes.[1] The

challenge that arises in using a simple potential step to harness the faradaic transient
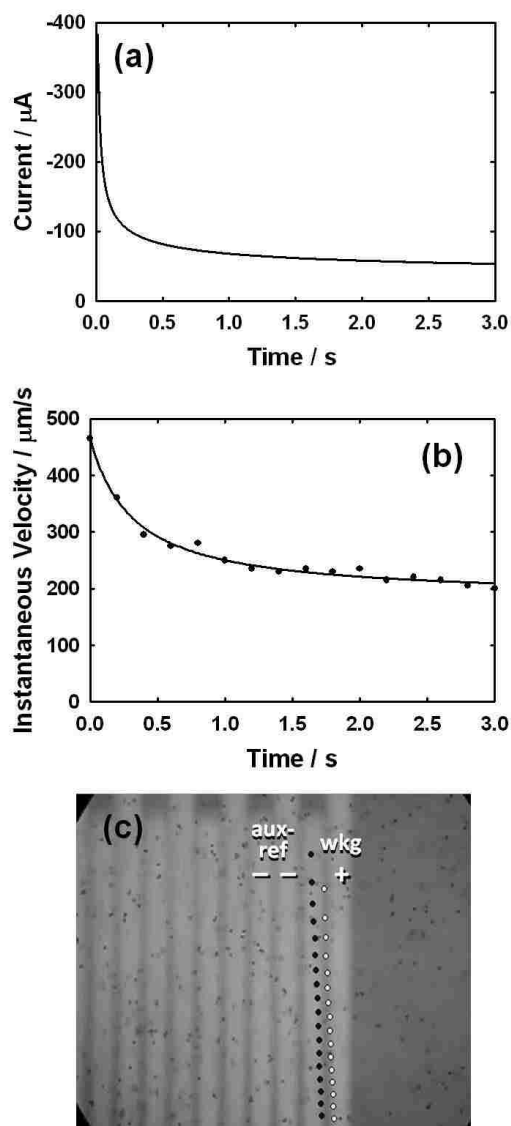
Figure 5.2. (a) Plot of current over time resulting from a potential step experiment (CA $0 \rightarrow +0.3$ V) at a 43 μm band electrode in a solution of 0.3 M $K_3Fe(CN)_6$, 0.3 M $K_4Fe(CN)_6$, and 0.1 M KCl. The combined counter and pseudo-reference electrode was 150 μm away from the working electrode. (b) Plot of instantaneous bead velocity ( ) over time for the experiment in (a),

where there was 0.2 s between t_{n+1} and t_n. (c) Microscope image showing two beads (black markers) tracked in solution over a three second period for the experiment in (a). Markers were placed at t_n and t_{n+1}. The working (anode) and combined auxiliary and pseudo-reference (cathode) electrode are indicated on the figure.

current to enhance fluid propulsion is that recovery of the depleted redox species cannot take place causing the current, and therefore the fluid velocity, to decrease over time.

Sweep-step function (SSF). Initial studies which first demonstrated the effect of the transient current showed that, when the potential at a set of electrodes was first stepped (to +0.3 V), the beads moved very quickly and then slowed to a steady state. Once the potential was reversed (to -0.3 V) the beads changed directions quickly, moved with a burst of acceleration and then, again, slowed to a steady state. As the potential was switched back and forth for equal amounts of time, there was no net displacement over time.[12] Thus, a potential waveform which would attempt to make use of the transient current while generating a flow in a net direction was investigated. A sweep-step potential waveform, shown in Figure 5.3, serves to fulfill these two functions. The potential is first swept from +0.3 V to -0.3 V, in which the scan rate determines the length of the sweep. Immediately following the sweep, the potential is stepped from -0.3 V to +0.3 V and held for some duration of time. The sweep portion of the potential waveform should allow for re-generation of the reduced form of the electroactive species in the diffusion layer to further allow the following step function to result in the same, high, initial current as would be present if the experiment were to start from "scratch." This is repeated for 12 cycles (six sweeps and six steps). This is the maximum amount of cycles possible with our instrumentation. Velocities were determined by measuring the distance the microbeads travelled over a certain time (essentially, an overall "displacement" per time). During the second portion of the sweep which involves electrochemical reduction of ferricyanide, the beads moved upward between the biased electrodes (see Figure 5.3).
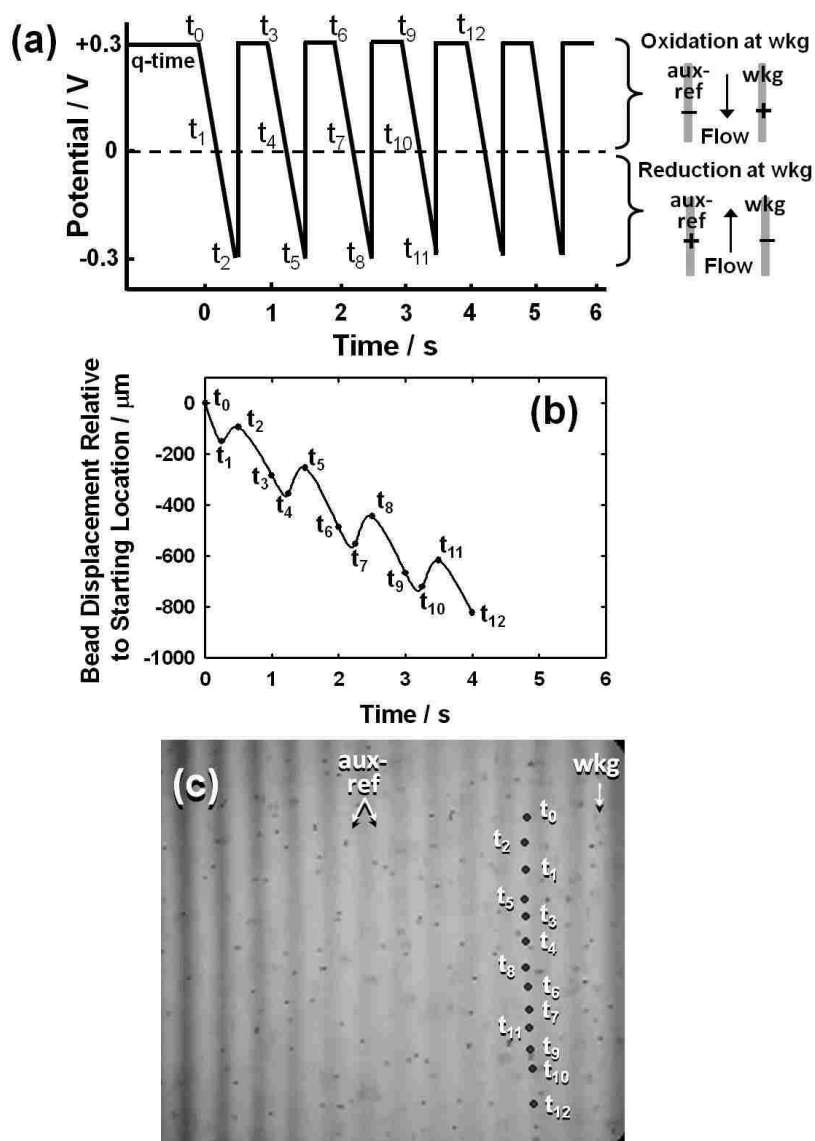
Figure 5.3. (a) Potential waveform for the sweep-step function (SSF). Potential is first swept at the working electrode from oxidizing to reducing potentials (+0.3 to -0.3 V vs the combined auxiliary-reference electrode) and then stepped back to oxidizing potentials (+0.3 V). Each step and sweep (scan rate = 1.2 V/s) segment lasted 0.5 s. They were repeated six times, resulting in 12 segments total. A schematic of the resulting flow directions between electrodes for excursions positive of $E_{1/2}$ and negative of $E_{1/2}$ are shown to the right. (b) Microscope image showing a single bead (black markers) tracked in solution throughout the SSF. Times indicated on the figure, next to the beads, correspond to the times throughout the waveform in (a). The working and combined counter and pseudo-reference electrode are indicated on the figure. A separation of 550 μm was used between the electrodes.

136

The beads then quickly changed direction, moving downward, as the potential was stepped to oxidize ferrocyanide. There was a net movement of the beads in the downward direction between the biased electrodes from the oxidation of ferrocyanide. This is referred to as "ratcheting" flow throughout this chapter. Bead movement was tracked over the course of the experiment. A still image of bead location with respect to particular times throughout the potential waveform is shown in Figure 5.3b. The sweep-step waveform was performed at a 43 μm band electrode, which was 550 μm from the combined counter and quasi-reference (indicated on the figure), in a 0.1 M KCl solution of 0.3 M $Fe(CN)_6^{3-}$ and 0.3 M $Fe(CN)_6^{4-}$.

Comparison of SSF to CA. In order to determine whether the ratcheting flow has any advantage over normal flow, velocities were compared between the sweep-step function (SSF) and a normal step function (CA). Figure 5.4 shows bead velocities resulting from a sweep-step potential function as well as a potential step function for solutions containing 0.003 M, 0.03 M, and 0.3 M each of $Fe(CN)_6^{3-}$ and $Fe(CN)_6^{4-}$. One 43 μm band served as the working electrode while two others, 550 μm away, served as the combined auxiliary and pseudo-reference electrodes. The velocities and currents (indicated on the figure) are reported over 3.0 s. The markers indicate the average of the overall bead velocity (from 0 to 3.0 s) from two separate beads tracked in solution (the error bars represent ± one half of the range between velocities measured from two different beads). As expected, lower concentrations result in lower velocities due to the lower currents and resulting F_B values. It was observed that the average velocities from the CA experiment were higher than those obtained from the sweep-step experiment for all concentrations. It was thought that sweeping the voltage back to reducing potentials,
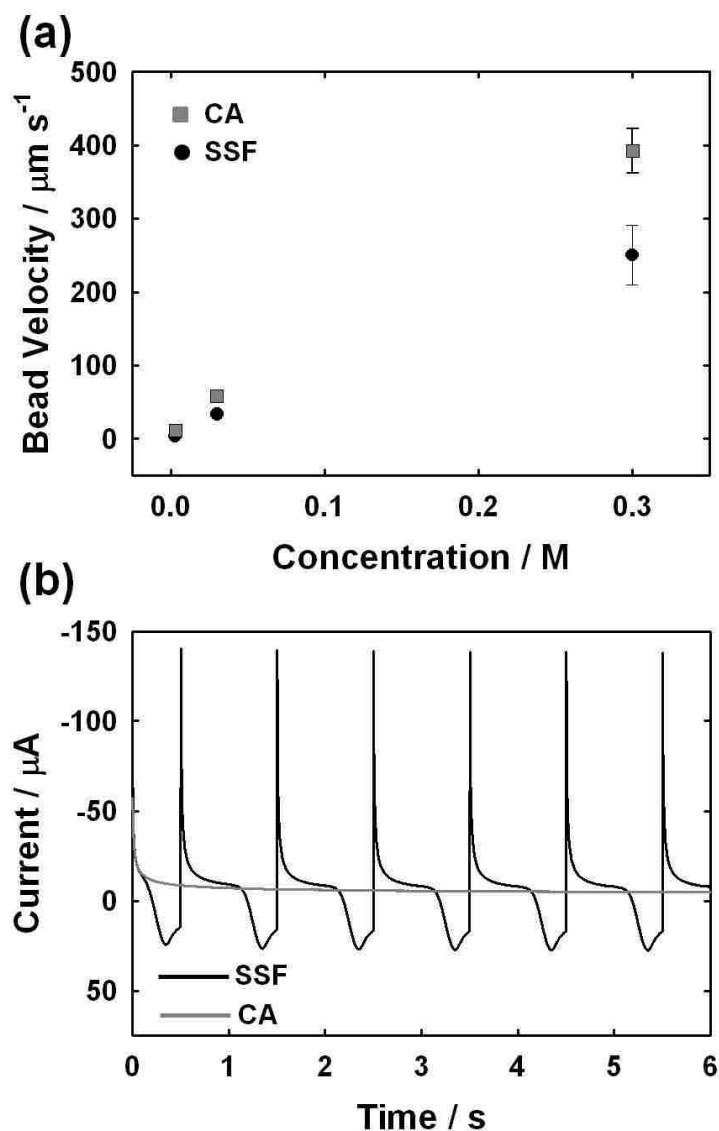
Figure 5.4. (a) Plot of bead velocity over time for three different concentrations of solution (0.3 M, 0.03 M, and 0.003 M each of $K_3Fe(CN)_6$ and $K_4Fe(CN)_6$ in 0.1 M KCl) comparing a SSF (black circles) to a CA (gray squares) experiment. Each marker corresponds to the average velocity between two beads; error bars represent the standard error between the two measurements. Velocities were determined over a 3 s period (for the SSF, this included three sweep and three step segments). The working electrode was a 43 μm band, separated from the combined auxiliary and pseudo-reference electrode by 550 μm. (b) Resulting electrochemical signals for the SSF (black) and CA (gray) experiments.

should allow the diffusion layer to become replenished, thereby yielding higher transient currents and faster overall flows. This was demonstrated for the 0.03 M solutions and the SSF experiment, in which the current during the step segment does decrease with each consecutive step, from 16.7 μA, for the first step (0.5 to 1 s), to 14.9 μA, for the sixth step (11.5 to 12.0 s), but corresponds to only a 11% decrease over time, whereas the current during a simple applied potential experiment decreases from 7.74 μA, from 0.5 to 1 s, to 4.37 μA, from 11.5 to 12.0 s, corresponding to a 43% decrease over time. Despite this enhancement in current during the SSF, from the repetitive high, transient currents, the reverse flow (and opposite current associated with it) which occurs during the reduction segment in the SSF causes the net displacement to be less and resulting overall velocities to be slower for this waveform when compared to a simple potential step (CA), during which, the current and flow are continuous in the same direction. Thus, a modification of this waveform in which reverse flow is minimized or eliminated is desirable.

Minimizing Reverse Flow. A similar sweep-step function was explored to eliminate reverse flow in which the potential was swept to 0 V instead of -0.3 V during the sweep segment. This waveform is shown in Figure 5.5a. Instead of the beads moving in the reverse direction during the sweep, they simply stopped for a brief amount of time and then continued movement, down the length of the electrodes, during the step segment. By increasing the scan rate during the sweep segments, the amount of time that the flow is stationary for can be reduced. Thus, the waveform was first optimized by determining bead velocities as a function of scan rate. The electrode configuration was the same from that above. The solution was 0.03 M $Fe(CN)_6^{3-}$ and 0.03 M $Fe(CN)_6^{4-}$. A

139
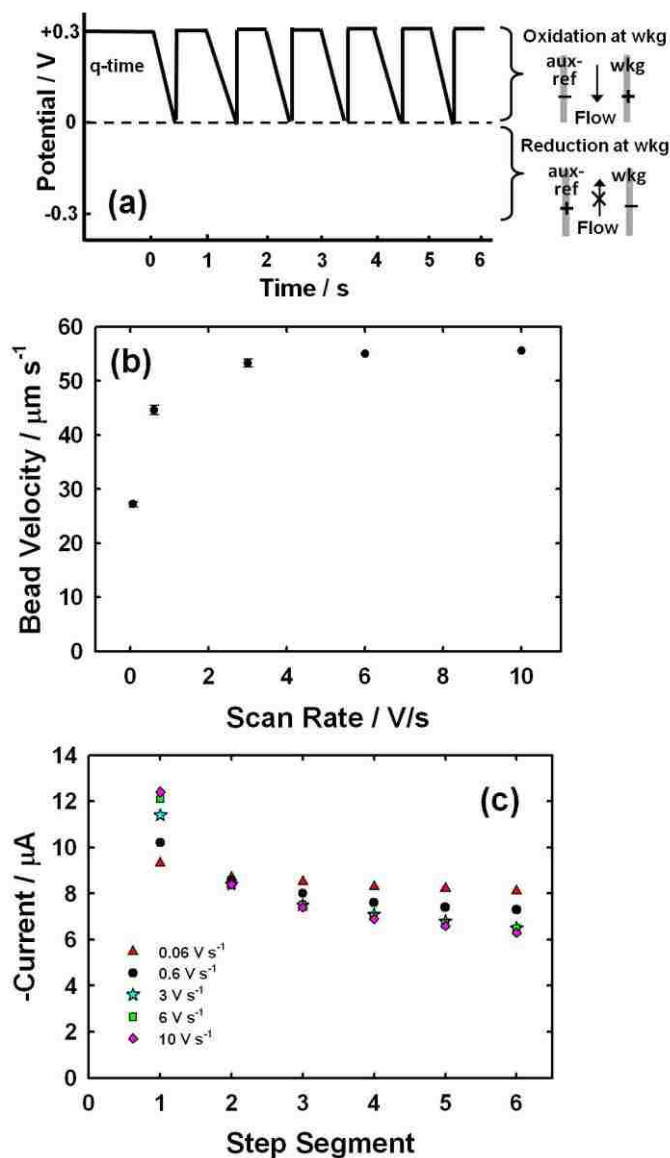
Figure 5.5. (a) Potential waveform for the sweep-step function (SSF) when the potential is only swept from +0.3 to 0 V and then stepped back to +0.3 V vs Au. The step segment lasts 0.5 s; the time of the sweep segment varies depending on the scan rate used. A schematic of the resulting flow directions is shown to the right of the waveform (upward flow should be eliminated by employing this SSF waveform). (b) Plot of bead velocity as a function of scan rate. Bead velocities were determined over the entire duration of the experiment (all 12 segments). (c) Plot of the average current over a 0.5 s step for each step segment in the SSF for varying scan rates during the sweep segments. Experimental parameters are the same as those in Figure 5.4.

plot of bead velocity as a function of scan rate is shown in Figure 5.5b. Bead velocities

were determined over the duration of the experiment (which was different for each scan

rate) so as to include every sweep and step segment. It was observed that the velocity

increased with increasing scan rate, as predicted, but leveled off beyond 3 V/s. A plot of

current as a function of each step segment during the SSF is also given in Figure 5.5c.

The current decreases at each sequential step and drops off more quickly at higher scan

rates. This is expected, as faster scan rates will allow less time for the diffusion layer to

become replenished between steps and thus, the resulting transient current will be lower

each time. A comparison between the optimized SSF (sweep from $0.3 \rightarrow 0$ V @ 10 V/s)

and CA revealed that the velocities were similar in each case: 55.3 μm/s for the SSF and

53.7 μm/s for CA, indicating that the SSF does not offer an advantage over a regular step

experiment. For SSF experiments (10 V/s sweeps), the current started out at 12.4 μA for

the first step (from 0 to 0.5 s) and decreased to 6.3 μA at the last step (2.68 to 3.18 s). For

CA experiments, the current was 13.7 μA from 0 to 0.5 s and decreased to 5.8 μA from

2.68 to 3.18 s. In both cases, the SSF and the CA experiment, flow velocities and

corresponding currents initially start out high and then decrease to a quasi-steady-state.

The challenge is that the transient results from depletion of redox species immediately

adjacent to the electrode; thus, when the potential is stepped repetitively at the electrode

to achieve another transient, the redox species is depleted, and over long times, the signal

eventually drops to that of steady state and there is no improvement of bead movement.

This is an interesting redox depletion and recovery problem.

Switching Experiments. It has been demonstrated that redox-MHD is capable of

affecting fluid flow at locations quite distant to the microelectrodes that generate the ion

flux.[12] Thus, it should be possible to allow almost complete recovery of depleted redox species, while sustaining fluid flow enhanced by faradaic transients, by alternately switching on and off different sets of electrodes located outside of each others' diffusion layers and with the right timing. To accomplish this, a device was fabricated with a design that breaks up pumping electrodes into multiple pairs separated length-wise by gaps. A switch was employed between the potentiostat and device to alternately turn on and off every other pair to allow pumping to continue in the same direction while allowing enough time of recovery of redox species by diffusion and convection. For switching procedures, one set of electrodes (set A on Figure 5.6a and 5.7a) originally serves as the working anodes while the other set (set C) serves as the combined auxiliary and quasi-reference cathodes ($\Delta E = 0.3$ V) for some amount of time (starting at "time 1" on the figure), based on the frequency of the switch. The sets are then switched at "time 2" and set B serves as the anodes while set D is the combined auxiliary and pseudo-reference cathodes, for the same amount of time (Figure 5.6b and 5.7b). While set A and C are active, set B and D are inactive (i.e. at open circuit) and vice versa. This switching is repeated and was investigated here at three different frequencies (119 ms, 220 ms, 450 ms) for 90 s. For control procedures (no switching), set A is the working anodes and set C is the combined auxiliary and pseudo-reference cathodes (Figures 5.6a and 5.7a).

Two different electrode configurations were explored. In the "small gap" configuration, the distance between each set of similarly biased electrodes (e.g. between anodes or between cathodes) was 155 μm (Figure 5.6a and 5.6b). In the "large gap" configuration, the distance was 407 μm (Figure 5.7a and 5.7b). The experimental parameters were as follows: the solution consisted of 0.1 M $Fe(CN)_6^{3-}$ and 0.1 M
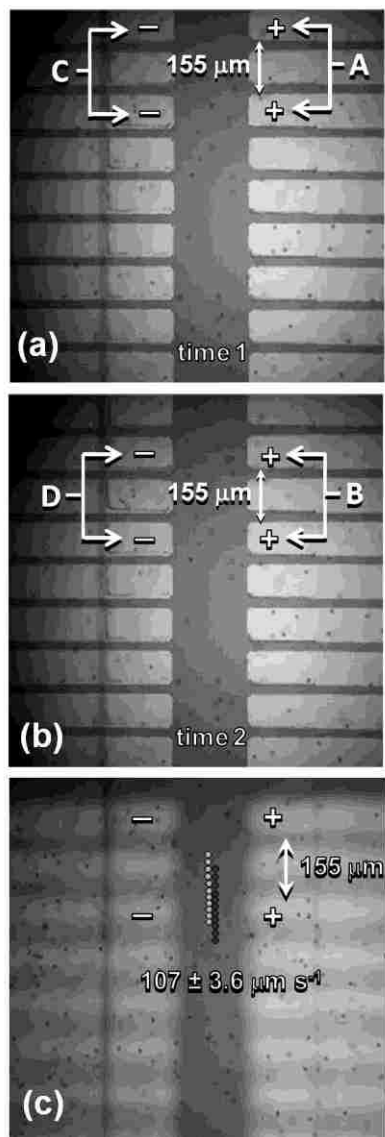
Figure 5.6. Diagram of switching procedures for the small gap configuration. (a) Set A initially serves as the working electrodes (anodes, +), while Set C serves as the combined counter and pseudo-reference electrodes (cathodes, -) at "time 1". The potential is held constant until "time 2" when the electrodes are switched. (b) Set A and Set C go to open circuit, while Set B is activated as the working anodes and Set D serves as the combined counter and pseudo-reference cathodes. Again, the potential is held constant. This cycle is then repeated. The gap between similarly biased pumping electrodes at any given time is 407 μm. (The electrodes used for the control procedures, when there was no switching, consisted only of (a). (c) Microscope image showing two beads tracked between the electrode Sets A and C (control experiment). The solution consisted of 0.1 M $K_3Fe(CN)_6$ and 0.1 M $K_4Fe(CN)_6$ in 0.1 M KCl. The potential difference applied between electrodes was 0.3 V. The average bead velocity is indicated on the figure.

143
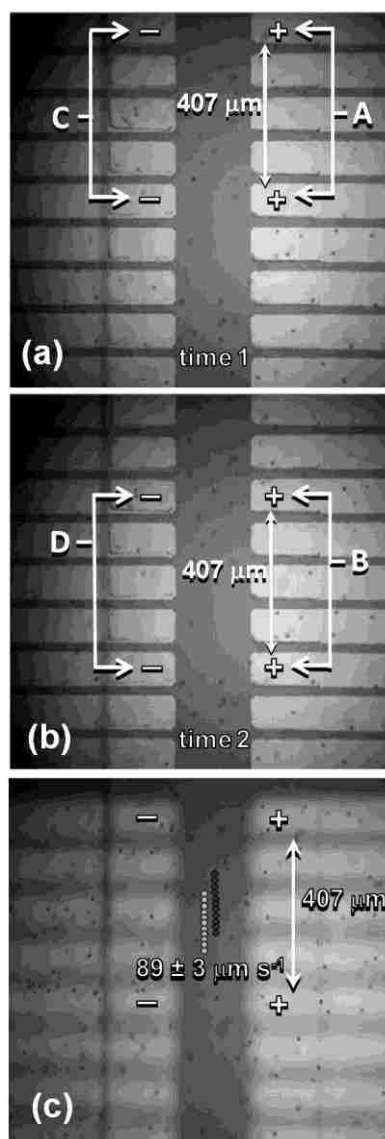
Figure 5.7. Diagram of switching procedures for the large gap configuration. Details are given in Figure 5.6. The gap between similarly biased pumping electrodes at any given time is 407 μm. (The electrodes used for the control procedures, when there was no switching, consisted only of (a). (c) Microscope image showing two beads tracked between the electrode Sets A and C (control experiment).

$Fe(CN)_6^{4-}$ in 0.1 M KCl containing 10 μm beads, a PDMS thickness of 760 μm was used, and a magnetic flux density of 0.38 T was employed. Velocity measurements were made approximately centered between the four biased electrodes, where the maximum flow rates were observed. A tracking image showing the path of the beads and the location of velocity measurements, for the small and large gap sizes, are indicated on Figures 5.6a and 5.7a, respectively. The beads are tracked over 1.67 s; markers are placed every 167 ms. There was no visible difference in flow trajectory between the switching (not shown) and control experiments. It is interesting to note that the flow is continuous down the length between oppositely biased electrodes of the two arrays, rather than circulating around individual pumping electrodes, even for a large gap size of 407 μm. This phenomena demonstrates an advantage of redox-MHD for fluid flow: pumping electrodes positioned far from one another can still direct flow without the need for channel walls.[19] The raw current responses obtained from the switching (black) and control or "no switching" (gray) procedures for the large gap configuration (Figure 5.7) and a switch time of 220 ms are given in Figure 5.8a. The currents achieved from the switching procedure were consistently higher than those from control studies. Likewise, the bead velocities from the switching procedure were also consistently higher than those from control studies as shown in Figure 5.8b. However, unlike the current transients, we did not observe velocity transients–the speeds appeared continuous as represented by the small error bars in that figure. The plotted bead velocities in Figure 5.8b are the average velocities of four different beads over a 1.67 s period at six different times throughout the experiment (1, 5, 10, 30, 60, and 90 s into the experiment).
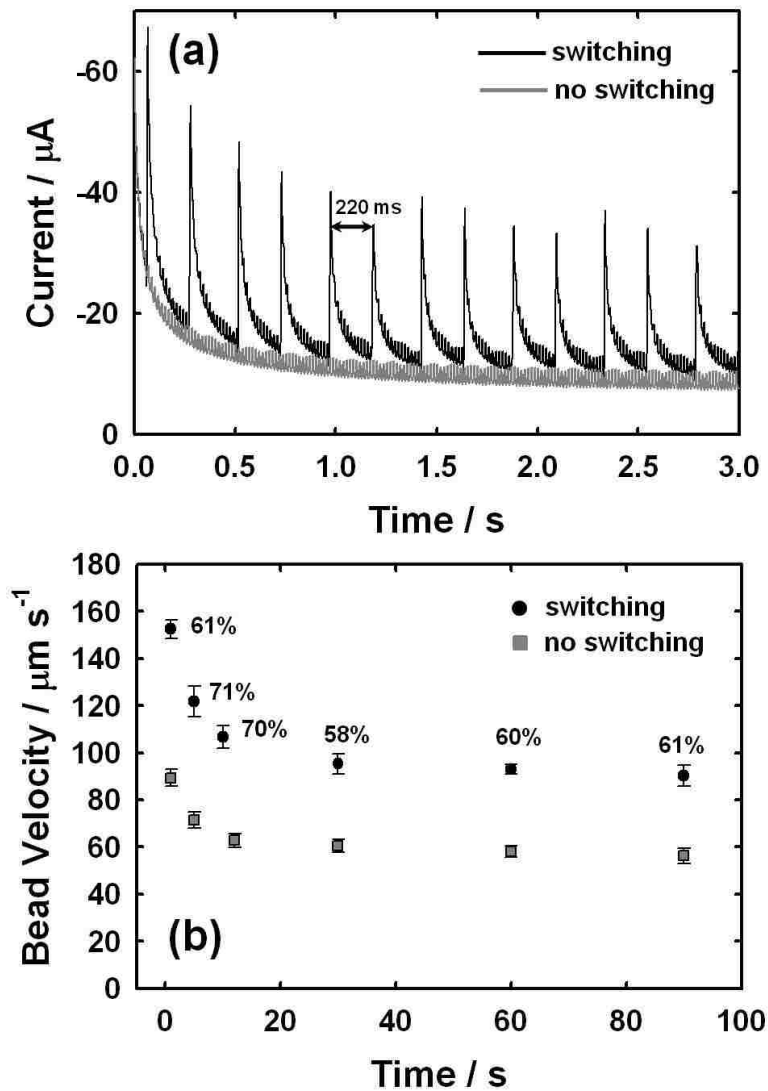
<u>Figure 5.8.</u> Comparison of (a) raw current responses and (b) corresponding bead velocities over time for control (gray curve and square markers, and setup in Figure 5.7a) and switching (black curve and circle markers, and setup in Figure 5.7a and 5.7b) procedures for the large gap configuration. Velocities were sampled at six different times throughout the experiment. Each marker corresponds to an average of four different velocity measurements. Error bars represent plus/minus one standard deviation over the four measurements. The percent enhancement of velocities obtained for the switching procedure over those for the control are indicated on the figure. The switching time was 220 ms.

The percent enhancements of velocities obtained with switching over the control procedure, at each time, are indicated on Figure 5.8b

(). Unfortunately, the high velocities achieved at the beginning of the experiment are not maintained throughout. For both, control and switch operations, the current and resulting velocities initially start high and then slow to a steady-state. A plot of current over time for both procedures is shown in Figures 5.9a and 5.9b, respectively. An approximate 32% decrease in current over time was observed for control studies; a 36% decrease was observed for switching procedures. Thus, even by allowing time for the diffusion layer to become replenished via the electrode switching, in addition to the presence of convection from the MHD force which should introduce fresh species, it is still not possible to sustain the high current over time due to an inability to ever fully recover from the depletion of redox species that initially occurs, especially in these short periods of time. However, velocities with the switch have still been improved, by an average 63% over control experiments, for the results shown in Figure 5.8.

The gap size and frequency of the switch were varied in attempts to optimize the switch to further increase velocities. A smaller gap size decreases the distance between similarly biased sets of electrodes and is therefore expected to allow for less recovery of the redox species between the sets. Faster switching times should, (1) decrease the length of the diffusion layer and improve redox species recovery due to a smaller volume to ecover, and (2) result in higher average currents because of the shorter time-frame (less time for current to decrease from depletion of redox species). Currents, velocities, and

147
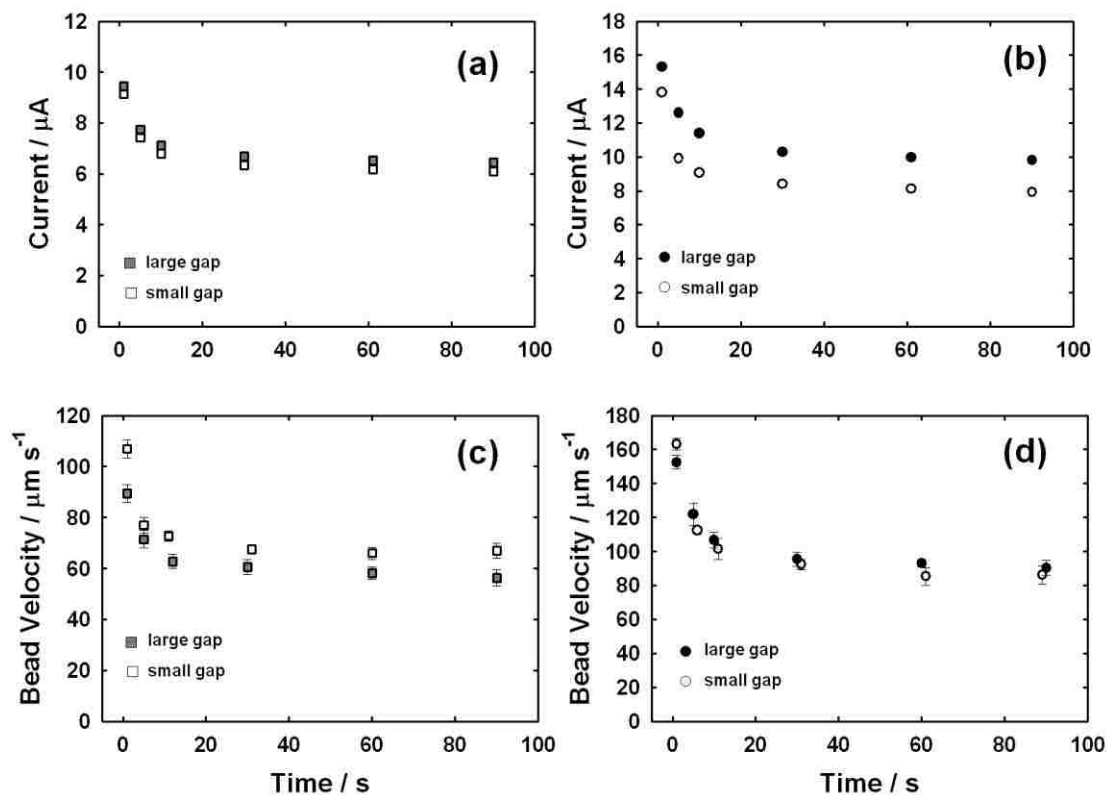
Figure 5.9. Comparisons of current, (a) and (b), and fluid velocity, (c) and (d), over time for control (square markers, a and c) and switching (circle markers, b and d) procedures, both performed with the small gap (open markers) and large gap (closed markers) configurations. The switching time was 220 ms. Current for switching experiments was sampled every 4 ms for 1.67 s, beginning at each time indicated on the plot, and is reported as an average of 417 points. Markers in (c) and (d) correspond to an average of four different velocity measurements. Error bars represent plus/minus one standard deviation over the four measurements.

percent enhancements between switching and control procedures obtained for these studies are presented in Table 5.1 (for the small gap configuration) and Table 5.2 (for the large gap configuration).

There did not appear to be a significant difference of the three different switching times (119, 220, and 440 s) on the resulting currents or velocities for either of the gapsizes. Gap size, however, did have an effect on currents and velocities, as shown in Figure 5.9 for one switching time, with more extensive data in the tables. A comparison of control studies for the small (open squares) and large (closed squares) gap sizes revealed that the current, for each, was approximately the same throughout, as indicated in Figure 5.9a. The velocities, however (shown in Figure 5.9c), are consistently greater for the small gap (open squares) than for the large gap (closed squares) configuration. This can most likely be explained as a result of the greater force density in the small gap configuration. Similarly biased electrodes that are closer together produce MHD forces that are also closer together, producing a greater net force over a smaller volume.

In the presence of switching, there are a couple of phenomena occurring. The first, as shown in Figure 5.9b is the difference in current between the small (open circles) and large (closed circles) gap configurations. The current is consistently greater for the large gap than for the small gap configuration throughout the experiment, which can be explained by a greater recovery of redox species that occurs at increased distances between active electrodes. Depletion is much more significant at the small gap and thus results in lower currents. The velocities, however, for both small and large gap configurations are similar throughout (Figure 5.9d) and can be explained by the greater

Table 5.1. Currents and velocities, at different times throughout each experiment, as a result of switching times and the control experiment (indicated as 0 s switching time) for the small gap configuration (Figure 5.6). Reported values for bead velocities are an average and standard deviation of four replicate bead measurements. Percent enhancements of currents and velocities during switching over control experiments are also indicated.

Switch time / ms		1 s	5 s	10 s	30 s	60 s	90 s
0	Velocity / $\mu m\ s^{-1}$	107 ± 3.6	77.0 ± 3.2	72.7 ± 2.1	67.5 ± 0.9	66.0 ± 2.4	67.0 ± 2.9
	Current / μA	9.14	7.44	6.79	6.34	6.18	6.10
440	Velocity / $\mu m\ s^{-1}$	171 ± 11	121 ± 2.9	104 ± 6.7	93 ± 4.2	92 ± 3.2	89 ± 3.7
	% enhancement	60	57	43	38	39	32
	Current / μA	13.9	10.0	9.13	8.36	8.05	7.64
	% enhancement	52	34	34	32	30	25
220	Velocity / $\mu m\ s^{-1}$	163 ± 3.5	112 ± 2.3	101 ± 6.1	92.4 ± 3.0	85.3 ± 5.2	86.2 ± 5.5
	% enhancement	53	32	39	37	29	29
	Current / μA	13.8	9.90	9.07	8.39	8.12	7.91
	% enhancement	51	33	34	32	31	30
119	Velocity / $\mu m\ s^{-1}$	158 ± 1.5	117 ± 5.8	104 ± 2.7	94.3 ± 3.5	93.7 ± 5.5	86.9 ± 5.4
	% enhancement	48	52	43	40	42	30
	Current / μA	13.9	10.4	9.07	8.35	8.11	7.99
	% enhancement	52	40	34	32	31	31

Table 5.2. Currents and velocities, at different times throughout each experiment, as a result of switching times and the control experiment (indicated as 0 s switching time) for the small gap configuration (Figure 5.7). Reported values for bead velocities are an average and standard deviation of four replicate bead measurements. Percent enhancements of currents and velocities during switching over control experiments are also indicated.

Switch time / ms		1 s	5 s	10 s	30 s	60 s	90 s
0	Velocity / $\mu m\ s^{-1}$	89.4 ± 3.5	71.4 ± 3.5	62.8 ± 2.8	60.5 ± 2.9	58.2 ± 2.4	56.2 ± 3.2
	Current / μA	9.44	7.73	7.11	6.69	6.53	6.45
440	Velocity / $\mu m\ s^{-1}$	144 ± 5.2	111 ± 4.9	99.4 ± 2.9	91.1 ± 3.8	87.7 ± 1.6	90.9 ± 0.43
	% enhancement	62	56	57	50	51	62
	Current / μA	14.6	11.7	10.5	9.74	9.34	9.41
	% enhancement	55	51	48	46	43	46
220	Velocity / $\mu m\ s^{-1}$	152 ± 4.0	122 ± 6.5	107 ± 4.6	95.4 ± 4.3	93.0 ± 2.1	90.3 ± 4.4
	% enhancement	61	71	70	58	60	61
	Current / μA	15.3	12.6	11.4	10.3	9.97	9.81
	% enhancement	62	63	60	54	53	52
119	Velocity / $\mu m\ s^{-1}$	149 ± 5.1	120 ± 2.6	103 ± 1.4	93.5 ± 3.2	91.3 ± 1.1	88.1 ± 1.6
	% enhancement	67	69	64	54	57	57
	Current / μA	15.0	12.2	11.2	10.1	9.71	9.56
	% enhancement	59	58	58	51	49	48

force density in the small gap configuration that offsets the localized lower force from the lower current. Thereby, the velocities are comparable to those obtained for the large gap.

Conclusions

Several methods that take advantage of the high faradaic transient current were investigated to maximize redox-MHD pumping while minimizing redox species concentration. Comparisons between using a sweep-step potential waveform and a simple potential step experiment revealed that there was no advantage to the former. The sweep-step potential waveform studies suffer from redox depletion and recovery problems. However, a novel method using a switch to alternately turn on and off electrodes was implemented that allows for recovery of redox concentrations and therefore enhances velocities over a pumping method using a simple step function by a minimum of 30% and by a maximum of 70%. Thus, redox species concentrations could be further decreased to achieve sufficient pumping speeds, having significant implications for the future of this technique.

References

(1)   Weston, M. C.; Fritsch, I. *Sensors and Actuators B* In Revisions.

(2)   Pamme, N. *Lab on a Chip* 2006, *6*, 24-38.

(3)   Qian, S. Z.; Bau, H. H. *Mechanics Research Communications* 2009, *36*, 10-21.

(4)   Weston, M. C.; Gerner, M. D.; Fritsch, I. *Analytical Chemistry* 2010, *82*, 3411-3418.

(5)   Grant, K. M.; Hemmert, J. W.; White, H. S. *Journal of Electroanalytical Chemistry* 2001, *500*, 95-99.

(6)   Lee, J.; Ragsdale, S. R.; Gao, X.; White, H. S. *Journal of Electroanalytical Chemistry* 1997, *422*, 169-177.

(7)   Leventis, N.; Dass, A. *Journal of the American Chemical Society* 2005, *127*, 4988-4989.

(8)   Leventis, N.; Gao, X. *Journal of the American Chemical Society* 2002, *124*, 1079-1086.

(9)   Pullins, M. D.; Grant, K. M.; White, H. S. *Journal of Physical Chemistry B* 2001, *105*, 8989-8994.

(10)   Aguilar, Z. P.; Arumugam, P. U.; Fritsch, I. *Journal of Electroanalytical Chemistry* 2006, *591*, 201-209.

(11)   Anderson, E. C.; Fritsch, I. *Anal. Chem.* 2006, *78*, 3745-3751.

(12)   Anderson, E. C.; Weston, M. C.; Fritsch, I. *Analytical Chemistry* 2010, *82*, 2643-2651.

(13)   Arumugam, P. U.; Clark, E. A.; Fritsch, I. *Anal. Chem.* 2005, *77*, 1167-1171.

(14)   Clark, E. A.; Fritsch, I. *Anal. Chem.* 2004, *76*, 2415-2418.

(15)   Grant, K. M.; Hemmert, J. W.; White, H. S. *J. Am. Chem. Soc.* 2002, *124*, 462-467.

(16)   Leventis, N.; Gao, X. *Analytical Chemistry* 2001, *73*, 3981-3992.

(17)   Weston, M. C.; Anderson, E. C.; Arumugam, P. U.; Yoga Narasimhan, P.; Fritsch, I. *Analyst* 2006, *131*, 1322-1331.

(18)   Wilkes, J. S.; Williams, M. L.; Musselman, R. L. *Electrochemistry* 2005, *73*, 742-744.

(19)   Weston, M. C.; Nash, C. H.; Fritsch, I. *Analytical Chemistry* 2010, *82*, 7068-7072.

Chapter 6

Conclusions and Future Directions

Conclusions

Fundamentals of redox-MHD microfluidics are explored in this dissertation. Parameters such as electrode size, redox species concentration, applied potential and current, electrode configuration, and cell height were all investigated for their effect on redox-MHD fluid flow. Redox-MHD microfluidics was determined to be well-suited for electrochemical detection in solutions compatible with enzyme-linked immunoassays. Redox-MHD fluidics were optimized by using a "switch" to maximize the current at alternating active electrodes. All of the fundamental studies reported in this dissertation should ultimately lead to integration of redox-MHD microfluidics into analytical chemistry applications.

A method using polystyrene microbeads to visualize fluid flow around microband electrode arrays was used to investigate spatially distributed velocities in a small, redox-MHD system. It was determined that a maximum flow rate of 1.44 mm/s could be achieved with these devices. Flow profiles, vertically and horizontally, through the solution were obtained. A flat flow profile between reinforcing flows was observed which could offer a significant advantage for applications requiring volumes and flow rates that are too large for electrokinetic pumping. These fundamental results will be useful in developing devices for redox-MHD microfluidics.

A highly controlled approach to manipulating fluid flow using applied current to generate the ion flux, as opposed to applied potential was investigated. Applying a current allowed for greater control over fluid velocities and allowed for the determination of quantitative relationships between current, magnetic field, and velocity. The

relationships between velocity and current and velocity and magnetic field are linear indicating that velocity can be finely tuned by adjusting either of these parameters. The log-log plots of these parameters revealed that current and magnetic field contribute equally to the velocity at an approximate 1:1 ratio. Other parameters such as increased electrode size and increased electrochemical cell height were shown to increase flow velocities.

Redox-MHD, for the first time, has been successfully used to deliver a plug containing an electroactive species in solution from an injection site to a detector and electrochemically detected there, all on a single device, without the need for channel walls. A redox pumping species ($Ru(NH_3)_6^{2+}$ and $Ru(NH_3)_6^{3+}$) which did not interfere with enzymatic activity in a solution compatible with enzyme-linked immunoassays was found. A solution plug containing an enzyme substrate, PAPP (no AP), was pumped through the surrounding solution containing the enzyme, AP (no PAPP), and the enzymatically generated PAP_R was easily detected and distinguishable electrochemically from the pumping species with square wave voltammetry down to 0.1 mM concentrations. It was determined that a small detecting electrode between pumping electrodes does not significantly alter flow velocities or trajectories. These initial findings indicate that redox-MHD microfluidcs could certainly be used for analytical chemistry applications.

A method for maximizing redox-MHD flow velocities was established. Using a switch to alternately turn electrodes on and off resulted in a continuous flow between electrodes and a higher current was generated at these electrodes, resulting in faster velocities, when compared to control experiments when the switch was not employed.

The switch allowed for a 70% maximum enhancement in velocities over control studies. By employing the switch, it is expected that much lower concentrations of redox species will generate flow velocities which could be used to move solution to different areas of a chip for use in analytical applications. Lower concentrations of redox species will provide advantages in detection methods and is elaborated upon in the Future Directions.

Future Directions

Many interesting and important discoveries were made with respect to redox-MHD microfluidics and are presented in this dissertation. However, there are some fundamental aspects which remain to be investigated and applications which need to be developed, such as the use of redox-MHD in analytical chemistry.

We have observed density gradients, in the absence of a magnetic field, which result in fluid flow in a different direction than that of MHD-induced flow. Quantitative studies involving flow visualization in and out of the magnet will reveal more about the contribution of these density gradients. They may even prove to be useful for stirring or directing fluid without the need for an external magnet. Also, there is some debate about where in solution the MHD force is applied; whether within the diffusion layer or throughout solution between the working and counter electrodes.[1-3] Thus, flow visualization studies are underway, using small permanent magnets placed very far (~5.5 mm) from the electrodes responsible for generating the ion flux, to investigate the effect on spatially distributed velocities.

We have noted that a flat flow profile is generated between reinforcing flows which could be beneficial for separations. Thus, it might be of interest to attempt to

perform a real separation in which analytes in a mixture could be distinguished, electrochemically from the pumping-redox species. This would likely require a slight design modification with a detecting electrode located at the end of a set of long pumping electrodes.

Now that a switch has been shown to increase velocities by as much as 70%, it is possible that it could be used to direct fluid from an injection port to a detector, as in Chapter 4 of this dissertation, but with much lower concentrations of redox-pumping species. In those studies, it was observed that detection limits for PAP_R increased from 5.7 μM to 25 μM in the presence of the pumping species. This is due to the baseline of the signal from oxidation of the pumping species contributing to the background of PAP_R, thereby interfering with detection of PAP_R, at low concentrations. Thus, it would be ideal to use a lower concentration of redox-pumping species. Assuming the switch can enhance velocities by as much as 70%, a pumping species at half the concentration could be easily used to achieve the same pumping speeds, but result in improved (lower) detection limits in its presence.

It is also of interest to fully integrate redox-MHD microfluidics into a device which would offer unique opportunities for and compatibility with lab-on-a-chip applications. Future work would likely involve performing a full, multistep assay which will require a modified microfluidic design to perform multisolution introduction and removal as well as regions for mixing on-chip to decrease incubation times. This concept is already underway in the Fritsch lab, in which chips have been made with pumping electrodes leading to separate regions which can be used for trapping or mixing fluids. In addition, with the use of the switch, it may be possible to alternately turn pumping and

159

mixing electrodes on and off at varying times in an automated fashion so that the

pumping does not interfere with the mixing process.

References

(1)   Kabbani, H.; Wang, A. H.; Luo, X. B.; Qian, S. Z. *Physics of Fluids* **2007**, *19*.

(2)   Qian, S.; Bau, H. H. *Physics of Fluids* **2005**, *17*.

(3)   Gerner, M. D. Master's Thesis, University of Arkansas, Fayetteville, AR, 2009.